UTS UNIVERSITY OF TECHNOLOGY SYDNEY

# In-pipe Robot Perception for Challenging Altered Environments

by

Delpachchitra Arachchige Amal Gunatilake

A thesis submitted in partial fulfillment of the requirements for the degree of Doctor of Philosophy

at the
UTS Robotics Institute
Faculty of Engineering and Information Technology
**University of Technology Sydney**

5th October 2021

# Certificate of Original Authorship

I, Delpachchitra Arachchige Amal Gunatilake declare that this thesis, is submitted in fulfilment of the requirements for the award of Doctor of Philosophy, in the School of Mechanical and Mechatronic Engineering, Faculty of Engineering and Information Technology at the University of Technology Sydney.

This thesis is wholly my own work unless otherwise referenced or acknowledged. In addition, I certify that all information sources and literature used are indicated in the thesis.

This document has not been submitted for qualifications at any other academic institution.

This research is supported by the Australian Government Research Training Program.

Signed: Production Note:
Signature removed prior to publication.

Date: 05/10/2021

UNIVERSITY OF TECHNOLOGY SYDNEY

# *Abstract*

Faculty of Engineering and Information Technology
UTS Robotics Institute

Doctor of Philosophy

by Delpachchitra Arachchige Amal Gunatilake

Robotics can play a crucial role in the condition assessment of critical infrastructure assets such as underground drinking water pipes. Currently, water utilities worldwide spend billions of dollars every year to reliably inspect and rehabilitate corroding and deteriorating pipes. Internal pipe linings are widely used as a renewal method to increase structural strength. Post pipe-lining quality assurance and long-term performance monitoring of the applied liners are essential for maintaining pipe assets. In this regard, this thesis focuses on the development of a multi-sensor approach to liner defect mapping in underground human-altered environments.

A mobile robotic sensing system that can scan, detect, locate, and measure internal pipeline defects is proposed. This is achieved by generating three-dimensional RGB-D maps using stereo camera vision in combination with an infrared laser profiling unit. The system does not involve complex calibration procedures and utilises orientation correction to provide accurate real-time RGB-D maps. Defects are identified and colour mapped for easier visualisation. The robotic sensing system was extensively tested under laboratory conditions, followed by field deployment in buried water pipes in Sydney, Australia. The experimental results showed that the RGB-D maps were generated with millimetre-level accuracy and with demonstrated liner defect quantification.

The accuracy of the map is dependent on the robot localisation. Therefore, a cost-effective UHF-RFID tags were used for robot localisation inside pipelines. The

results showed that unlike outdoor RFID localisation, inside the pipeline, the signal behaves uniquely, which makes the localisation task challenging and unique. Signal processing using a Gaussian process combined particle filter was applied to accurately localise the robot. Experiments carried out on field-extracted pipe samples from the Sydney Water pipe network showed that using the RSSI and Phase data together in the measurement model with the particle filter algorithm improves the localisation accuracy up to millimetre-level, through utilisation of a two-antenna sensor model.

Robot localisation assumes an accurate map. In pipes, this is tedious and therefore SLAM is desirable. A novel solution for SLAM using UHF-RFID signal processing for underground pipe environments is proposed. The problem was formulated as a Graph-SLAM combining signal cross-correlation and mapping with respect to the RFID sensor measurements. Experiments in the laboratory showed that the solution can localise the robot with 2.5-centimetres accuracy while building the RFID map. The results showed that the solution allows accurate identification of defect locations in a 50-meter long pipe, and performs vastly better than standard encoder-based localisation methods.

# *Acknowledgements*

I would like to specially thank my supervisor Prof. Sarath Kodagoda for providing all necessary support and guidance throughout my degree, and for the valuable time he contributed to assist me with my research.

I also thank my co-supervisor Prof. Gamini Dissnayake for providing constant feedback related to my research work.

I thank the University of Technology Sydney (UTS), Robotics Institute and Faculty of Engineering and IT for granting me this valuable scholarship to pursue my higher studies. I further extend my gratitude to UTS Tech Lab for providing laboratory facilities.

I specially thank Australian Federal Government for funding this project through the Cooperative Research Centres Projects (CRC-P) grant and Sydney Water for providing resources and facilitating to carry out field trials.

I thank my research team colleagues who supported me in numerous ways. I like to specially thank Dr. Karthick Thiyagarajan, Dr. Lasitha Piyathilaka, Mr. Vinoth Viswanathan, Dr. Antony Tran and Mr. Sathira Wickramanayake who gave me consistent support.

I thank my family and friends who motivated, encouraged, and supported me throughout my education.

Last but not least, I thank all those who helped me in one way or other to make this research a success.

This thesis was edited by Elite Editing, and editorial intervention was restricted to Standards D and E of the Australian Standards for Editing Practice.

# Contents

# List of Figures

# List of Tables

# Acronyms & Abbreviations

| | |
|---|---|
| **1D** | One-dimensional |
| **2D** | Two-dimensional |
| **3D** | Three-dimensional |
| **ANN** | Artificial Neural Network |
| **CAC** | Calcium Aluminate Cement |
| **CAS** | Centre for Autonomous Systems |
| **CCTV** | Closed Circuit Television |
| **CIPP** | Cured-In-Place-Pipe |
| **COTS** | Commercial Off the Shelf |
| **CPU** | Central Processing Unit |
| **CRC-P** | Cooperative Research Centres Project |
| **EKF** | Extended Kalman Filter |
| **ELF-EP** | Extreme Low Frequency Electromagnetic Pulse |
| **EPC** | Electronic Product Code |
| **GP** | Gaussian Process |
| **GPR** | Ground Penetrating Radar |
| **GPS** | Global Positioning System |

**GUI** Graphical User Interface

**IMU** Inertial Measurement Units

**IR** Infrared

**LiDAR** Light Detection and Ranging

**LPDDR** Low-Power Double Data Rate

**LTPM** Long Term Performance Monitoring

**PAQA** Post Application Quality Assurance

**PEC** Pulsed Eddy Current

**PF** Particle Filter

**PIRO** Pipe Inspection Robot

**PVC** Polyvinyl Chloride

**RAM** Random Access Memory

**RAM** Random-Access Memory

**RF** Radio Frequency

**RFID** Radio Frequency Identification

**RGB** Red-Green-Blue

**RGB-D** Red-Green-Blue Depth

**RMSE** Root Mean Square Error

**ROS** Robotic Operating System

**RSSI** Received Signal Strength Indicator

**RVIZ** ROS Visualisation

**SLAM** Simultaneous Localisation and Mapping

**SSD** Solid State Drive

**ToF** Time of Flight

**UHF** Ultra High Frequency

**UTS** University of Technology Sydney

**WSAA** Water Services Association of Australia

# Nomenclature

| | **General Notations** |
|---|---|
| $m$ | Metre (unit). |
| $cm$ | Centimetre (unit). |
| $mm$ | Millimetre (unit). |
| $m/s$ | Metres per second (unit). |
| $t$ | Time (continuous). |
| $GB$ | Gigabytes (unit). |
| $dB$ | Decibel (unit). |
| $dBi$ | Decibels per isotropic (unit). |
| $Hz$ | Hertz (unit). |
| $ppr$ | Pulses per revolution (unit). |
| $fps$ | Frames per second (unit). |

# Glossary of Terms

| | |
|---|---|
| Ambient | Pertains to the immediate surroundings. |
| Anomalies | Data that deviates from the standard, normal, or expected. |
| Autonomous | Without human intervention. |
| Field Deployment | The transportation of equipment to a place or position for desired operations. |
| Forecasting | Predict or estimate the future trends or unknown events. |
| Liner defects | Anomalies that occur on the protective coating of the pipe internal surface. |
| Measurements | The action of measuring the physical quantities. |
| Modelling | A description of a system using mathematical concepts and language. The process of developing a mathematical model is termed mathematical modelling. |
| Predictive Analytics | A variety of statistical techniques from predictive modelling, machine learning and data mining to predict future trends or unknown events by using historical and transactional data. |
| Real-time | Relating to a system in which input data is processed within milliseconds so that it is available virtually immediately as feedback to the process from which it is coming. |
| Resistance | The measure of the degree to which a conductor opposes an electric current through that conductor. |
| Robust | Able to withstand or overcome adverse conditions. |
| Sensing Suite | A set of sensors enclosed in a housing to perform measurements of interest. |

| | |
|---|---|
| Sensor | A device that detects or measures a physical property, indicates or otherwise responds to it. |
| Sensor Failure | The state of improper functioning of a sensor. |
| Sewers | An underground conduit for carrying off drainage water and waste matter. |
| Smart | Device programmed so as to be capable of some independent action. |
| Study | A detailed investigation and analysis of a subject or situation. |
| Technology | Device or equipment developed from the application of scientific knowledge. |
| Quantification | The measurement of the variable of interest. |
| Odometry | The measurement of robot movement from the aid of robot sensors. |

# Chapter 1

# Introduction

Robotics and artificial intelligence never cease to amaze with their advancements. This is an era in which robots are becoming human's best friend. Tasks formerly deemed highly complicated and dangerous have become simplified and safe, allowing people to perform their activities more efficiently and securely. Robotics has made its mark in almost every possible domain including space exploration, manufacturing, military defence, security, health care, household services, transportation, agriculture, emergency response, construction, and maintenance, to name a few. When it comes to the field of maintenance, robotics plays a major role in managing underground infrastructure assets.

Globally there are millions of kilometres of underground pipelines that transport necessities for humankind such as drinking water, household gas, and waste water. Over time, those pipe assets can degrade due to a combination of environmental factors and characteristics such as pipe material, age, size, the nature of the transported material, soil condition, and internal and external pressure [6, 7]. Therefore, it is of paramount importance to identify such degradation to minimise the potential for catastrophic pipe failures and leakages [8]. However, as pipes may be very narrow and are mostly underground, monitoring or inspection is a difficult task due to complexities associated with bends, accessibility, and residue. Even in larger pipes, human entry to such confined spaces to enable visual and physical inspection is associated with high health and safety risks.

Therefore service utilities use a variety of robotic technologies [9–14] to monitor and identify degrading regions of pipelines. Following discovery of such issues, water utilities may opt to employ interventions including replacement. The estimated expenses of pipe replacement range from AU$400/m (for small pipes) to AU$4,000/m (for large pipes) [15]. This means that it costs water utilities millions or billions of dollars every year to maintain their underground pipeline infrastructure. For example, in Australia, AU$100 billion is estimated as the cost of replacing the entire pipe network [16]. Around AU$5 billion is estimated as the urgent pipe replacement cost and around AU$2.5 billion as the maintenance cost over a period of five years [16].

## 1.1 Research Background

In Australia, to address this problem, water utilities use pipe lining technologies such as Cured-In-Place-Pipe (CIPP) [17–19] and spray liners [20–22] to prevent corrosion of the metallic pipes and extend the service life of those assets at a lower cost, providing a cost-effective alternative to pipe replacement. Pipe linings are protective coatings applied to the pipe surface. They are made of a resin-based epoxy formulation that mainly consists of polyurea and polyurethane; or a flexible tube made of felt and fibreglass-like materials to prevent pipe surface corrosion [15, 23]. Fig. 1.1 shows examples of corroded and liner applied pipe samples. However, the integrity of pipe linings may diminish over time for a number of reasons, including improper application or curing of linings in the short term, which can lead to physical flaws such as folds, wrinkles, dimples, and bulges in the long term [3, 15, 24, 25]. Hence, these pipelines need to be monitored using a non-invasive sensing technology before and after application of liners to identify any signs of corrosion and assess the quality of applied liners. Since pipe environments are confined and hostile, robots have emerged as effective means of monitoring the evolution of liner defects.

Currently, the most commonly used robots for monitoring pipes are traditional Closed Circuit Television (CCTV) camera-based crawler robots with wheel or tether line encoder odometry tracking systems [26]. However, they only offer visual cues, which provides limited information for decision making and does not provide the quantitative measurements required to critically assess the condition of a pipe to avoid catastrophic

FIGURE 1.1: Corroded and liner applied pipe samples [1].

failure. Solutions such as embedded sensors in pipes to monitor their condition are still futuristic [27]. There have been attempts to utilise 3D reconstruction technologies such as Light Detection and Ranging (LiDAR) [28, 29], and Time of Flight (ToF) cameras [30] to assess the internal surface of large-diameter pipes and tunnels, that require only centimetre-level accuracy. However, such technologies do not provide the millimetre-level accuracy required to properly assess smaller scale defects in smaller-diameter pipes [31–33].

Pipes can be very slippery for robots because of the presence of water puddles and mould, rendering the traditional technique of utilising wheel odometers for in-pipe robot localisation inaccurate in terms of position estimating [8]. Most of the popular outdoor localisation technologies, such as Global Positioning System (GPS), cannot be used in pipelines because of GPS signal limitations in pipe environments [34]. Dead reckoning techniques based on Inertial Measurement Units (IMU) which employ magnetometers and accelerometres to provide absolute measurements of heading and downward directions are not suitable for in-pipe robot localisation, primarily because the magnetometer component will not provide an accurate measurement of heading angles, and can cause drift [35]. Popular outdoor localisation methods such as visual Simultaneous Localisation and Mapping (SLAM) prevent challenges in underground pipeline infrastructure because of human alterations and long-term visual feature variation in changing environmental conditions.

## 1.2 Research Motivation

Pipe lining technology has the potential to extend the life of pipes by up to 50 years, providing a cost-effective alternative to more expensive pipe replacement and thus saving millions of dollars for water utilities annually . Therefore, the Australian Government has funded a multi-million-dollar industry research project entitled "Smart Linings for Pipes and Infrastructure" Cooperative Research Centres Project (CRC-P), involving more than 30 partners including water utilities to research in improved lining and monitoring technologies. In collaboration with the Water Services Association of Australia (WSAA), water utilities, liner/coating manufacturers, liner/coating applicators, and researchers, the project aims to develop standards and specifications for fit-for-purpose liners/coatings with smart sensing/robotic capabilities to improve the utilisation of linings. The research team from the University of Technology Sydney (UTS) is developing robotic sensing systems for Long Term Performance Monitoring (LTPM) and Post Application Quality Assurance (PAQA) of liners/coatings as part of the CRC-P. PAQA is critical in pipeline rehabilitation because it establishes benchmarks for liner applicators in regard to the required quality assurance for liners, giving utilities confidence in the product delivery and application [15]. Further, non-invasive LTPM would enable utilities to predict when their assets need to be repaired. There are currently no tools or procedures for successful use of this form of assessment.

The outcome of this research will eventually set standards and guidance for performing analytical tests for liner validation. It will further improve the design and application of smart lining products. Most importantly, it will save billions of dollars for the government by extending the service life of its underground pipe assets and prevent catastrophic pipe failures that cause disruptions to public and environmental health.

Additionally, the outcome of this research will contribute to the advancement of field robotics with improved sensing technologies for infrastructure condition assessment, and introduce robot localisation technologies outside the norm.

## 1.3 Research Problem

The main problems that need to be addressed in this research are:

- Research Problem 1: Improper application of liners to pipelines may lead to liner defects in the pipe. Therefore, sensing these defects is important for PAQA. While current robotic technologies are capable of detecting defects, they cannot quantify them to critically assess the quality of liner application. Thus, the research problem is, how to develop a robotic technology that can detect, process, and quantify defects in pipes through non invasive sensing and data appropriate processing? The solution must be capable of identifying defects, and measuring and categorising them based on the severity of the damage to the liners.
- Research Problem 2: To monitor the evolution of liner defects by comparing profiles acquired at different times, an accurate robot localisation is required. Therefore, the research questions is, how to achieve an accurate and reliable in-pipe robot localisation where the pipe internal structure is subjected to change? The solution must be capable of accurately localising identified defects monitored at different times using a multi-sensor robotic platform, without being affected by the human-altered environment inside pipelines in the long term.

## 1.4 Principal Contributions

The principle contributions of this research are:

1. First, a stereo vision-based laser profiling system integrated with a mobile robotic platform is proposed for real-time Red-Green-Blue Depth (RGB-D) mapping with true colour information extracted from the pipelines using colour and Infrared (IR) cameras. The proposed approach requires only a one-time calibration and generates RGB-D mapping with millimetre level accuracy for pipe diameters ranging from 400 to 700 mm. The system generates heat-maps that highlight and measure defective areas in scanned pipelines, which enables easy monitoring of damaged areas and

damage evolution in the long term. Stereo vision is utilised to detect the orientation of the robot by determining yaw and pitch parameters, which assists in accurate RGB-D map building.

2. Second, a novel Ultra High Frequency (UHF)-Radio Frequency Identification (RFID) signal-based in-pipe localisation system is proposed for the mobile robotic platform to accurately localise the robot in known RFID terrains. The system is proposed to employ a Gaussian process (GP) combined particle filter localisation approach that utilises both Received Signal Strength Indicator (RSSI) and phase signals in the measurement model to improve the localisation with a two-antenna hardware model. The system performs significantly better than commonly used localisation systems, and localises the robot with millimetre-level accuracy.

3. Third, an innovative UHF-RFID signal-based simultaneous localisation and mapping system is proposed for the mobile robotic platform to localise accurately in long-rage unknown RFID-mounted terrains inside the pipelines. The study of the unique RFID signal patterns inside the pipeline leads to a new measurement model with signal correlation techniques integrated into the SLAM algorithm to accurately localise the robot. The proposed solution was tested in long pipe ranges. It performs significantly better than commonly used localisation systems, producing approximately 2.5 cm accuracy.

## 1.5 Publications

The following is a list of the publication outcomes from this thesis:

### 1.5.1 Journal articles

1. **A. Gunatilake**, L. Piyathilaka, A. Tran, V. K. Vishwanathan, K. Thiyagarajan, and S. Kodagoda, "Stereo Vision Combined With Laser Profiling for Mapping of Pipeline Internal Defects," IEEE Sensors Journal, vol. 21, no. 10, pp. 11 926–11 934, 2021.

2. **A. Gunatilake**, K.Thiyagarajan, S. Kodagoda, "A Novel UHF-RFID Dual Antenna Signals Combined with Gaussian Process and Particle Filter for In-pipe Robot Localization," IEEE Robotics and Automation Letters. *(Accepted for publication.)*

3. **A. Gunatilake**, K.Thiyagarajan, S. Kodagoda, "Robot Simultaneous Localization and Mapping Inside Pipelines Using UHF-RFID Signals," IEEE Robotics and Automation Letters. *(Under Review.)*

### 1.5.2 Conference Proceedings (Peer-reviewed)

1. **A. Gunatilake**, L. Piyathilaka, S. Kodagoda, S. Barclay, and D. Vitanage, "Real-Time 3D Profiling with RGB-D Mapping in Pipelines Using Stereo Camera Vision and Structured IR Laser Ring," in 2019 14$^{\text{th}}$ IEEE Conference on Industrial Electronics and Applications (ICIEA), 2019, pp. 916–921, doi: 10.1109/ICIEA.2019.8834089.

2. **A. Gunatilake**, M. Galea, K. Thiyagarajan, S. Kodagoda, L. Piyathilaka and P. Darji, "Using UHF-RFID Signals for Robot Localization Inside Pipelines," in 2021 IEEE 16$^{\text{th}}$ Conference on Industrial Electronics and Applications (ICIEA), 2021, pp. 1109-1114, doi: 10.1109/ICIEA51954.2021.9516284.

3. **A. Gunatilake**, K.Thiyagarajan, S. Kodagoda, "Evaluation of Battery-free UHF-RFID Sensor Wireless Signals for In-pipe Robotic Applications," IEEE Sensors Conference, 2021, pp. 1-4, doi: 10.1109/SENSORS47087.2021.9639827.

## 1.6 Thesis Layout

The remainder of this thesis is structured as follows:

**Chapter 2** presents an improved laser profiling system that can scan, detect, locate, and measure internal pipeline defects by generating 3D RGB-D maps using stereo camera vision combined with an IR laser profiling unit. This work was published as [2, 3].

**Chapter 3** proposes a cost-effective localisation method using UHF-RFID signals for robot localisation inside pipelines, based on a Gaussian Process (GP) combined particle filter. This work was published as [4, 5].

**Chapter 4** proposes a localisation and mapping system inside pipelines when RFID tag locations are unknown, by using a novel measurement model with UHF-RFID signal mapping technique with the SLAM algorithm. The system localises the robot with higher accuracy than encoder-based localisation methods, while building a RFID tag location map. This work is under review with IEEE Robotics and Automation Letters.

**Chapter 5** summarises the research work presented in this thesis, presents conclusions, and discusses the limitations of the presented work. It then outlines potential future research in this area.

# Chapter 2

# Pipeline Internal Defects Mapping Through Stereo Vision Combined Laser Profiling

## 2.1 Introduction

Water and waste water pipes undergo severe metallic corrosion with age [12, 36, 37]. To reduce the cost of pipe replacement, water utilities adopt a range of lining technologies including spray liners and CIPP liners that can add a protective layer to mitigate the effects of corrosion. However, these lining technologies can fail as a result of poor application, internal pipe pressure, and environmental conditions over time. As part of the CRC-P collaborative project, a survey was carried out with liner manufacturers, liner applicators, researchers, and water utilities to identify the most important liner defect that can occur after application. The survey outcomes showed that liner imperfections were considered the most important defect that requires monitoring for quality assurance purposes [15]. Liner imperfections or defects include folds, wrinkles, dimples, and bulges in pipelines [15, 23, 24]. Since the pipes are mostly underground, timely monitoring for fit-for-purpose renewal to avoid failures is a significant challenge for water utilities around the world. Human entry to such confined spaces for visual and physical inspections is impossible

because of size constraints and in some cases is associated with high health and safety risks.

Some pipe inspection robots [38–40] are more application oriented, being designed for specific requirements, and some generic methods are not able to identify and quantify defects accurately [41, 41–56] as they rely on traditional CCTV inspection. Currently, the most commonly used inspection method for liner assessment is crawler robots based CCTV cameras. However, these robots fail to provide critical structural information for making accurate decisions regarding maintenance of underground infrastructure, because they only provide visual information with not quantitative measurements. Several studies have used CCTV camera vision with image processing algorithms or Artificial Neural Network (ANN) based laser data fusion to inspect images captured from the inner surfaces of pipelines [57–59]. These methods can identify major defects such as holes or cracks on the pipe wall, but are not sufficiently accurate to sense delicate features that may indicate smaller scale defects in liners. Several research groups are quantitatively assessing the quality of liner applications, including via Pulsed Eddy Current (PEC), Ground Penetrating Radar (GPR), and ultrasound sensing [13, 36, 37, 60–63]. Although they provide reasonable subsurface level measurements, these sensors work in close contact with the pipe surface to take spot measurements, which is highly time consuming and impractical in terms of monitoring the entire pipe surface. To cover a large surface area in a short time, an array of sensors can be utilized but this will increase the cost of the hardware significantly, as the sensors are very expensive.

In the past, LiDAR sensing technology has been used to create 3D maps inside tunnels and large diameter pipes [28]. LiDAR sensors are primarily designed to detect obstacles and objects around the scanned area and are most suitable for long-range measurements. Therefore, their accuracy is limited to a few centimetres [29]. Most pipe defects are smaller up to sub-centimetre level and cannot be detected by LiDAR sensors. Further, these sensors only provide distance measurements and do not provide true colour information about the scanned surface in the 3D point cloud.

Cameras such as Realsense and Kinect, which project structured IR light patterns to generate 3D point clouds [30], are commonly used in mobile robotic platforms. With

structured IR light, patterns are projected in very close proximity; thus, when the distance from the measured surface increases, the resolution of the project pattern decreases, resulting in lower accuracy of measurement. Hence, it may not be possible to detect or measure small defects in pipelines using such cameras [31–33].

Most recent studies have used monocular camera vision-based laser profiling with mobile robots. This technology provides more accurate structural information. Measurement accuracy depends on the camera resolution. Using this approach, several studies have been undertaken to identify and quantify structural defects and calculate ovality changes in pipelines [64–69]. The problem with monocular vision is that it needs extensive field calibration under different environmental conditions. Further, because of the inability to detect the lateral movements of the robot navigation, when these occur, the generated 3D maps become defective and the measurements become inaccurate. As these systems have extensive field calibration requirements, the data gathered from such systems cannot be processed and visualised in real time, and must be processed offline. This limits opportunistic decision-making during robot deployment, requiring multiple deployments to fill gaps in missed scan areas or collect high-resolution data in areas of interest.

The most commonly used non-destructive method in water industries for scanning and identifying defects in water pipelines is 3D laser profiling with mono camera vision [66, 70, 71]. This method uses a continuous red laser ring projection on the pipe wall that is captured by a calibrated camera [71–73]. The system is mounted on top of a mobile robotic platform and deployed inside the pipeline. When the laser line projects onto a pipeline defect, small deviations are produced in the laser line projection and are captured by the camera. Camera calibration parameters are used with simple trigonometry to identify and measure the defects. The system requires traversal of the pipeline without any lateral movements to achieve high accuracy. Slight deviations can create large errors in the generated 3D point cloud. Further, this monocular system cannot capture colour information from the pipe surface because the red laser projection overlays the true colour information about the surface [74].

Therefore, current technologies available for 3D reconstruction of underground and

internal surfaces are highly abstract and some of the most highly accurate technologies are immobile, and time consuming in terms of data collection. To overcome the limitations discussed above, this research proposes an improved laser profiling system that utilises stereo camera vision with IR laser pattern projection (Fig. 2.1). The proposed stereo system can calculate the depth of the laser projection, which helps identify lateral movements of the robot using implemented algorithms, leading to increased accuracy of 3D map reconstruction. The system is highly efficient and does not require extensive field calibration at each deployment, unlike mono camera vision-based laser profiling systems. Therefore, it can be effectively deployed in different environments with a wide range of pipe diameters. As it does not require field calibration, while the robot is traversing the pipeline, the system is capable of generating real-time 3D point clouds. The use of an IR laser beam with IR and Red-Green-Blue (RGB) cameras, instead of the traditional red laser, allows for extraction of the true colour information from the pipe surface; thus generating accurate RGB-D maps. The data can be further processed in real time to generate a heat map that highlights ovality changes in the pipe surface, enabling easy visualisation and identification of defects.

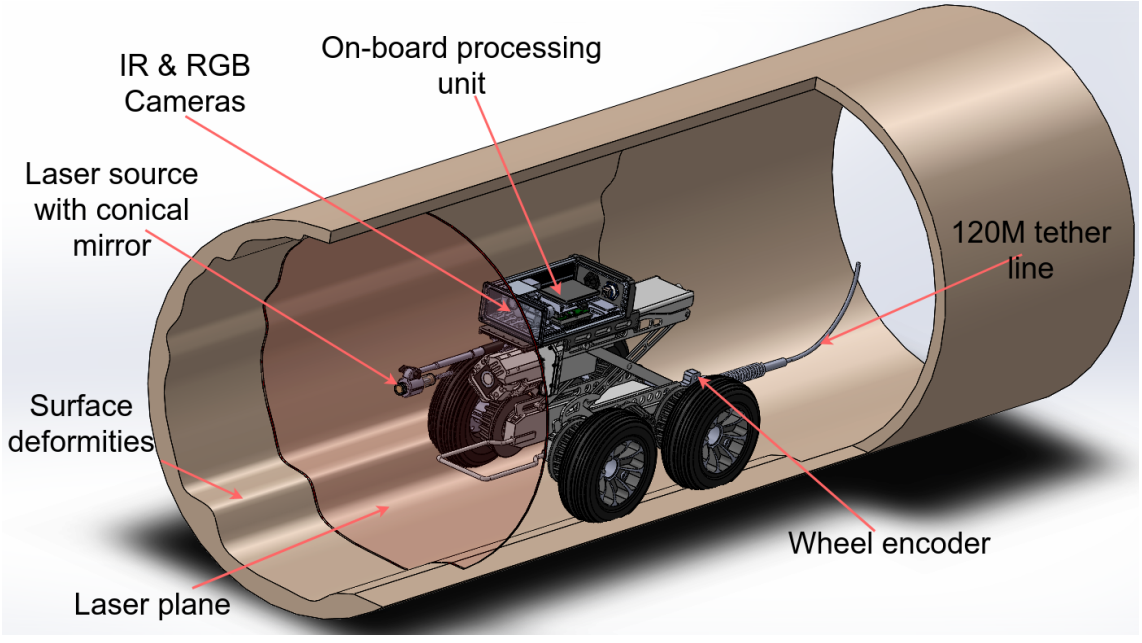


FIGURE 2.1: The robot design with the laser profiling sensors [2].

The key contributions of this chapter are:

- First, a stereo vision-based laser profiling system is proposed with an integrated mobile robotic platform for real-time RGB-D mapping with true colour information extracted from pipelines using colour and IR cameras. The proposed approach requires only one-time calibration and generates RGB-D maps with 1-mm accuracy for pipe diameters ranging from 400 to 700 mm.
- Second, the system generates heat maps that highlight and measure defective areas in scanned pipelines, which enables easy monitoring of damaged areas and damage evolution over the long term.
- Third, the stereo vision is utilised to detect the orientation of the robot by determining yaw and pitch parameters, which assists in accurate RGB-D map building.

## 2.2 3D Data Generation and Processing

This section describes algorithms used for camera calibration, stereo mapping, RGB mapping, defect detection, and robot orientation estimation. The overall 3D data generation and processing execution pipeline is shown in Fig. 2.2. Images from a camera system are fed into image processing algorithms along with camera calibration parameters. The laser projection is filtered and a 3D point cloud is generated using stereo processing algorithms and the odometry received from the robot tracking system. The odometry is further calibrated using orientation detection algorithms. The 3D point cloud receives the colours extracted from the RGB image. Using circle detection and ray casting algorithms, a heat map is generated by detecting ovality changes, which highlight defects.

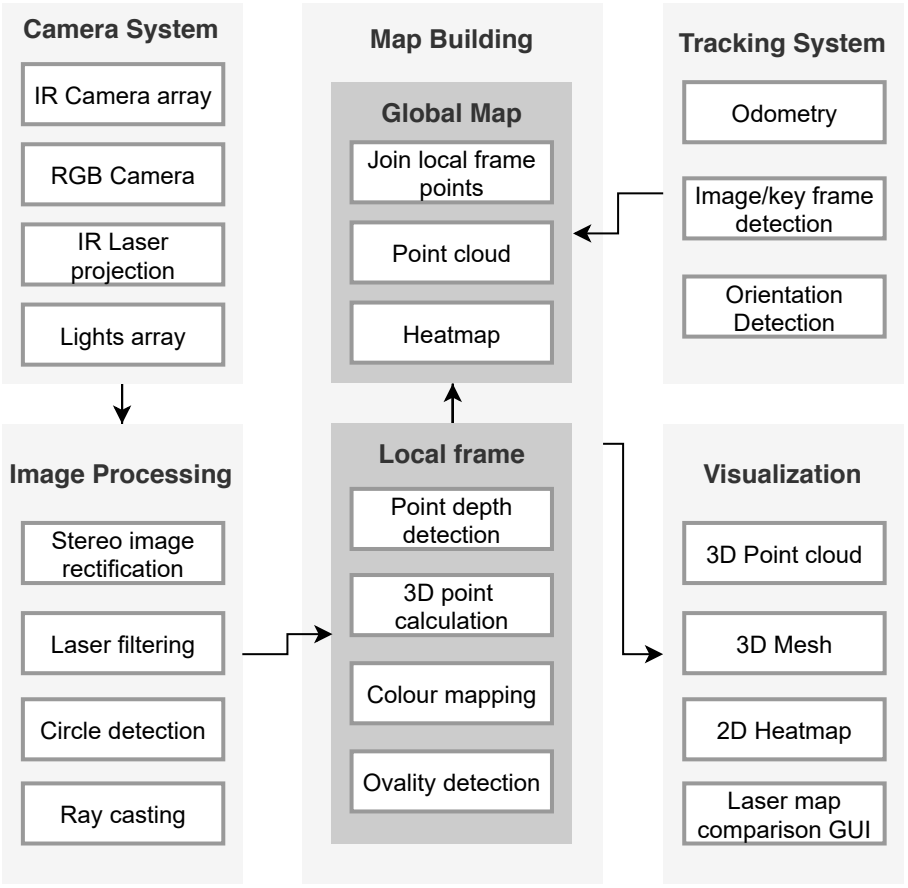


FIGURE 2.2: Execution pipeline [3].

### 2.2.1 Camera Calibration

Camera calibration plays a major role in measurement accuracy because of various factors in camera optics such as lens distortion, different camera focal lengths, and camera misalignment [75–77]. Raw camera images are calibrated using Equation (2.1), where $x$ and $y$ are the pixel coordinates for the original image; $r$ is the radial distance from the image centre to the pixel; $k_1, k_2, k_3, ..., k_n$ are the radial distortion coefficients; and $n$ is the number of iterations:

$$\begin{bmatrix} x' \\ y' \end{bmatrix} = \begin{bmatrix} x \\ y \end{bmatrix} [1 + k_1 r^2 + k_2 r^4 + k_3 r^6 ... + k_n r^{2n}] \tag{2.1}$$

The distortion coefficients are estimated by utilising a checkerboard-like pattern.

Stereo camera calibration is carried out using intrinsic and extrinsic camera parameters. The 3D coordinates of the object are projected onto a Two-dimensional (2D) image plane using Equation (2.2) with intrinsic and extrinsic camera parameters. $(x, y)$ represents the 2D image coordinates for the object; and $(X, Y, Z)$ represents the 3D coordinates for the object in the real world. The intrinsic camera parameters are $(f_x, f_y)$ for focal length, $(c_x, c_y)$ for the optical centre, and $(s)$ for the skew coefficient. The extrinsic camera parameters consist of rotation coefficients $(r_{11}, ..r_{33})$ and translation coefficients $(t_1, t_2, t_3)$:

$$\begin{bmatrix} x \\ y \\ 1 \end{bmatrix} = \begin{bmatrix} f_x & s & c_x \\ 0 & f_y & c_y \\ 0 & 0 & 1 \end{bmatrix} \begin{bmatrix} r_{11} & r_{12} & r_{13} & t_1 \\ r_{21} & r_{22} & r_{23} & t_2 \\ r_{31} & r_{32} & r_{33} & t_3 \end{bmatrix} \begin{bmatrix} X \\ Y \\ Z \\ 1 \end{bmatrix} \tag{2.2}$$

Similar to the distortion parameter estimation, a checkerboard pattern is used for stereo camera calibration. These calibration parameters are later used in the 3D reconstruction process.

### 2.2.2 Stereo Image Processing

Stereo image processing is used to generate an accurate point cloud with true colours mapped from the scanned pipe. The highest-intensity point is detected in one image to identify the laser beam points, while the other image is searched along the epipolar lines to find the corresponding points. Since the laser beam is circular, two intersection points are detected during the epipolar line search. This is resolved by carrying out a directional search starting from the centre of the image.

The disparity $d$ between the two image features (Fig. 2.3) are calculated by Equation (2.3), comparing the corresponding points from left and right image pairs. The relationship between the real-world object coordinates and the image coordinates is denoted by Equation (2.4), where $f$ is the focal length, $T$ is the distance between the two focal points, $P = (X_p, Y_p, Z_p)$ are the object position coordinates, $p_l = (x_l, y_l)$ is the left camera image coordinate, and $p_r = (x_r, y_r)$ is the right camera image coordinate [78]:

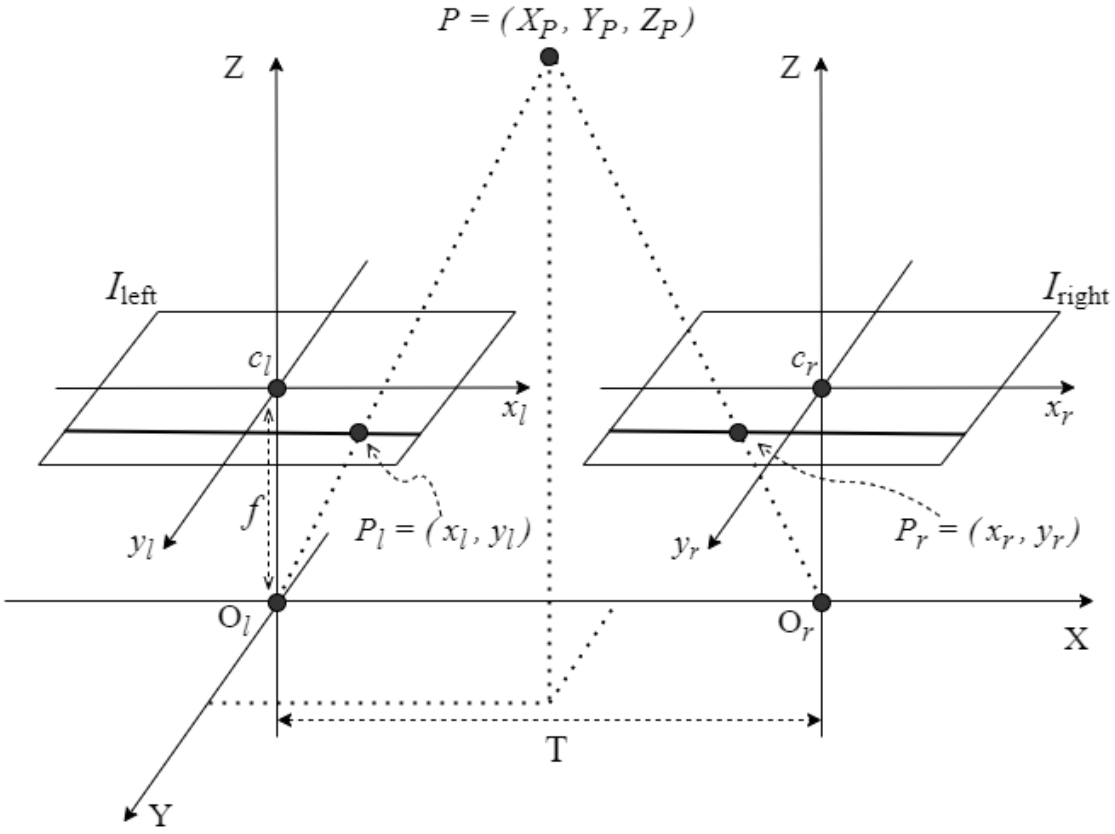


FIGURE 2.3: Stereo vision reference frames of the co-ordinate system.

$$d = (x_l - x_r) \tag{2.3}$$

$$x_l = \frac{X_p f}{Zp};\ x_r = \frac{(X_p - T)f}{Zp};\ y_l = y_r = \frac{Y_p f}{Z_p}; \tag{2.4}$$

From (2.3) and (2.4):

$$Z_p = f\frac{T}{x_l - x_r} = f\frac{T}{d};\ X_p = x_l\frac{T}{d};\ Y_p = y_l\frac{T}{d} \tag{2.5}$$

The stereo-based depth estimation can be used to generate the 3D structure of the internal pipe surface, and to calculate the orientation of the robot with respect to the pipe axis. Further, it can be used to carry out RGB colour mapping of the 3D pipe.

### 2.2.3 RGB Mapping

The calculated depth information is used for RGB mapping by stereo calibrating one IR camera with one RGB camera and projecting the 3D points onto the colour image using Equation 2.6:

$$\begin{bmatrix} p_x \\ p_y \end{bmatrix} = \begin{bmatrix} s_x & 0 & 0 \\ 0 & 0 & s_z \end{bmatrix} \begin{bmatrix} P_x \\ P_y \\ P_z \end{bmatrix} + \begin{bmatrix} c_x \\ c_z \end{bmatrix} \tag{2.6}$$

where, $(P_x, P_y, P_z)$ are the 3D real-world coordinates, $(p_x, p_y)$ defines the colour camera image coordinates, $s$ is an arbitrary scale factor, and $c$ is an arbitrary offset.

Once the 3D point is projected onto the colour image, the RGB values of the mapping location are taken and embedded into the generated point cloud. A high-level implementation of the algorithm is given in Algorithm 1:

### 2.2.4 Defect Detection and Mapping

Defects are estimated from the colour heat map and ovality measurements through detection of the centre of the pipe followed by casting. Through experimentation, it was discovered that image processing functions available in OpenCV such as Hough Circle did not offer a sufficiently accurate way to detect the centre of the pipe from captured laser profile images. The main causes of the circle detection error are lighting changes due to defects and various other surface irregularities. Therefore, a novel approach was developed and implemented to detect the circle on the image, along with its centre.

First, the image is converted into a distance transform map using grayscale values. Then, using matrix operations, a rough circle diameter is estimated to generate a dummy circle at the centre of the image. Next, distance transform values are added along the generated circle circumference by extracting the grayscale image. Then, by iteratively changing the position of the circle and its radius, the algorithm searches for the minimum summation of distance transform values along the circle circumference using an optimisation algorithm.

**Algorithm 1** Generate point cloud

/* $I$ →image, $L$ →left, $R$ →right, $C$ →circle, $W$ →width $P$ →points */
/* FUNCTION PARAMETERS */
$I_L, I_R, I_C, Odometry, CamParams, Threshold$
/* INITIALIZATION OF VARIABLES */
$C_L : W_{I_L}/2$
$C_R : W_{I_R}/2$
$PointCloud : []$

---

$I_L : Undistort\_Image(I_L, CamParams)$
$I_R : Undistort\_Image(I_R, CamParams)$
$I'_L, I'_R : Rectify\_Images(I_L, I_R, CamParams)$
$P_L : Extract\_Coordinates(I'_L, Threshold)$
**for all** $p_l \in P_L$ **do**
  /* Search points along epipolar lines */
  $P_R : Find\_Corresponding\_Points(I'_R, p_l)$
  /* The search returns two, left and right points along epipolar lines */
  **for all** $p_r \in P_R$ **do**
    **if** $(x_{p_r} < C_R \;\&\&\; x_{p_l} < C_L) \;||\; (x_{p_r} > C_R \;\&\&\; x_{p_l} > C_L)$ **then**
      $[x, y, z] : Triangulate(p_l, p_r, CamParams)$
      $[r, g, b] : Project([x, y, z], I_C, CamParams)$
      $z = z + Odometry$
      $Point3D : [x, y, z, r, g, b]$
      $PointCloud : Append(Point3D)$
    **end if**
  **end for**
**end for**
**return** $PointCloud$

---

Let the camera image matrix be $I_{h,w}$, where height is $h$ and width is $w$. Using the Chebyshev distance transform function $Dt$, the image distance transform matrix $D_{h,w}$ can be defined as in Equation 2.7:

$$D_{h,w} \;=\; Dt(I_{h,w}) \tag{2.7}$$

For any given two points, the difference of the $x$ coordinate is $\Delta x$ and the difference of the $y$ coordinate is $\Delta y$; then, the Chebyshev distance $D_{h,w}$ matrix calculated using Equation 2.8:

$$\sum_{i,j} D_{h,w}(x, y) = \sum_{i=1}^{h} \sum_{j=1}^{w} \left[ max_{i,j} \left( |\Delta x_i| \;,\; |\Delta y_j| \right) \right] \tag{2.8}$$

As in Fig. 2.4, the circle centre is denoted by $x_c$, $y_c$ and the radius is denoted by $r_c$. Search initialisation values are as in Equations 2.9, 2.10, and 2.11:

$$x_c = w/2 \tag{2.9}$$

$$y_c = h/2 \tag{2.10}$$

$$r_c = [max(I_w) - min(I_w)]/2 \tag{2.11}$$

Using Equation 2.12, the coordinates $(P)$ of the circle circumference are generated where $x_i,\ y_i$ is taken as a single coordinate:

$$(x_i - x_c)^2 + (y_i - y_c)^2 = r_c^2 \tag{2.12}$$

Now the distance transform values $(V_1, V_2, ..., V_n)$ in the distance transform map $D$ that belongs to the circle circumference coordinates $P$ are used to calculate the total sum $T$:

$$V = D(P) \tag{2.13}$$

$$T = \sum_{i=1}^{n} V_i \tag{2.14}$$

The perfectly fitting circle $C_{optimum}$ is found with minimising $T$ by changing the values of $x_c, y_c, r_c$ variables.

$$C_{optimum} = \underset{x_c, y_c, r_c}{argmin}(T \mid x_c, y_c, r_c) \tag{2.15}$$

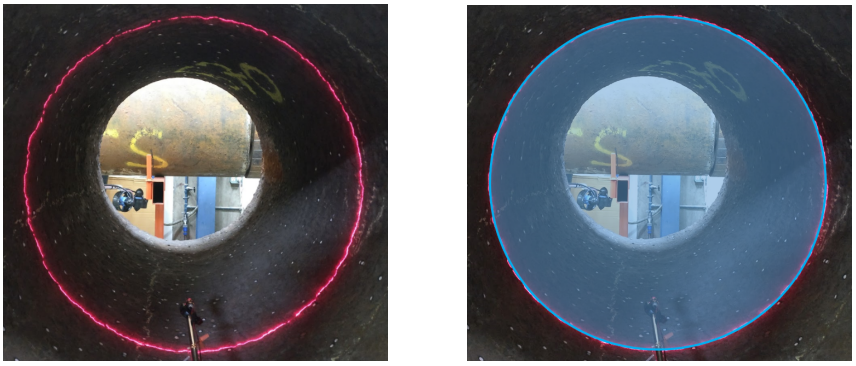

(a) The laser projection view before circle fitting.

(b) Projection of the optimum circle found by the algorithm.

FIGURE 2.4: Circle fitting [3].

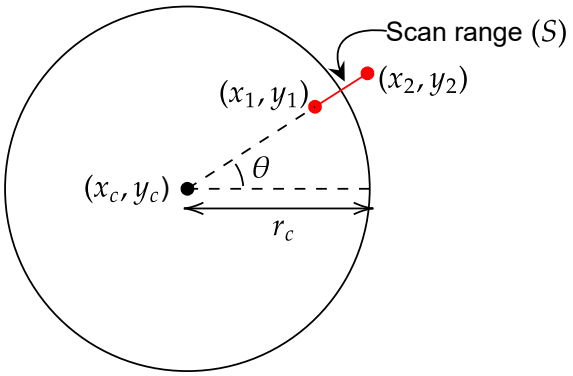


FIGURE 2.5: Ray casting [3].

Fig. 2.4 shows an example result from application of the optimal circle detection algorithm. The optimum circle parameters are now used for ray casting. Existing ray casting algorithms can be computationally demanding as they tend to start the scan from the centre. Therefore, a dynamic scan range parameter is used to define a scan region around the pipe surface. This minimises the unnecessary computational cost of the algorithm.

Let $x_1, y_1$ be the starting point of the scan range $(S)$ and $x_2, y_2$ be the end point of the scan range. By defining the equation of a line with $x, y$ and changing the angle $(\theta)$, rays can be cast around the circle:

$$x_1 = x_c + [(r_c - S/2)\ cos\ \theta] \tag{2.16}$$

$$y_1 = y_c + [(r_c - S/2)\ sin\ \theta] \tag{2.17}$$

$$x_2 = x_c + [(r_c + S/2)\ cos\ \theta] \tag{2.18}$$

$$y_2 = y_c + [(r_c + S/2)\ sin\ \theta] \tag{2.19}$$

$$x - x_1 = \left[\frac{y_2 - y_1}{x_2 - x_1}\right](y - y_1) \tag{2.20}$$

The optimised ray casting algorithm can be used to cast rays around the laser projection to scan and identify surface anomalies when generating the point cloud. Fig. 2.6 provides an example of ray casting in a zoomed IR image, showing how the white pixels created

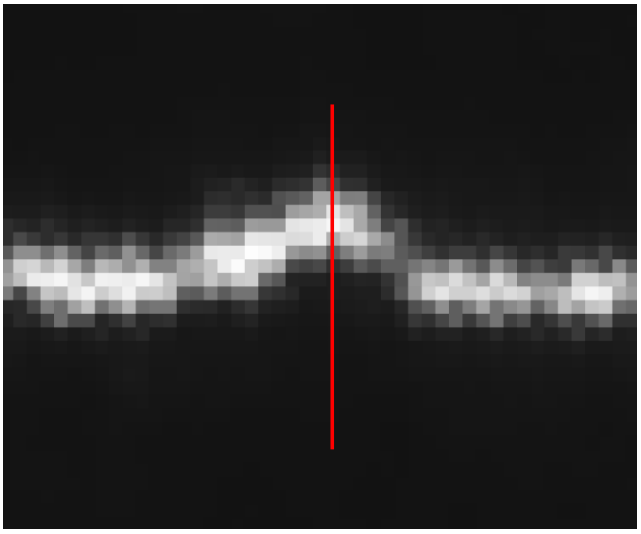

FIGURE 2.6: Laser projection intensity [3].

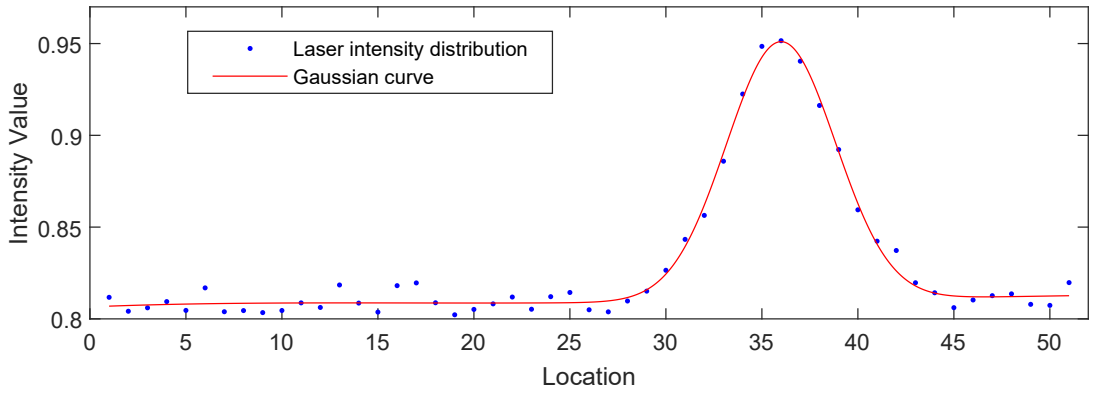


FIGURE 2.7: Gaussian curve fitting [3].

from the laser projection are not consistent, and thus that the ray scan along the red line needs to determine the centre of the laser projection.

Most lasers tend to create a thick laser line on the projected surface because of the reflection properties of the surface and defects (Fig. 2.6). The extracted distance transform values are fitted with a Gaussian kernel to identify the midpoint of the thick laser line projection. Fig. 2.7 shows an example Gaussian kernel used for laser intensity distribution of a ray cast line.

Let $\mu$ be the mean and $\sigma$, the standard deviation of the calibrated coefficients; $x$ is the intensity variation; and $i$ is the number of terms to be determined (which is four in the

proposed system) for the Gaussian distribution $G(x)$ as follows:

$$G(x) = \sum_{i=1}^{n} \frac{1}{\sigma\sqrt{2\pi}} \exp\left[\left(-\frac{1}{2}\left(\frac{(x-\mu)}{\sigma}\right)\right)^2\right] \tag{2.21}$$

The location of the highest-intensity point is used to calculate the distance to the centre. Similarly, all ray lines are examined to identify the highest-intensity location, to calculate distances from the centre. The average radius is estimated and compared with all the calculated distances from the radius to identify defects, and hence to generate a defect heat map. A high-level implementation of the algorithm is demonstrated as in Algorithm 2:

**Algorithm 2** Defect mapping

/* $I$ →image, $r$ →radius, $c$ →circle*/
/* FUNCTION PARAMETERS */
$I, Odometry$
/* INITIALIZATION OF VARIABLES */
$Range$ : 100 /* Dynamic param */
$Resolution$ : 1000 /* Launch param */
$Heatmap, Ovality$

---

$[x_c, y_c, r_c] : Circle\_Fitting(I)$
$step : 2\pi/Resolution$
**for all** $\theta \in 0 : step : 2\pi$ **do**
  $[X_n\ Y_n] : Ray\_Cast(Img, [x_c, y_c, r_c], \theta, Range)$
  $gp : Gaussian\_Process([X_n\ Y_n])$
  $[x, y] : Get\_Highest\_Intensity\_Point(gp)$
  $distance : |\sqrt{(x-x_c)^2 + (y-y_c)^2}|$
  $error : distance - r_c$
  $Heatmap : Append(Odometry, \theta, error)$
**end for**
$Ovality : [\max(error) - \min(error)]/r_c$
**return** $Heatmap, Ovality$

### 2.2.5 Orientation Detection

It is important to detect the orientation of the robot as it traverses inside the pipeline, because in situations where the robot slightly rotates as a result of control noise, or when it traverses over a hump or a ledge, its orientation will change, causing deformations in

the point cloud. Having a mechanism to detect the orientation will help in aligning the point cloud for better measurement accuracy.

An iterative closest point (ICP) algorithm [79] is implemented in the system to detect the orientation of the robot by comparing the point clouds generated in laser profile scans. First, a base point cloud ($P$) that is in the estimated orientation when the robot correctly aligns with the pipe orientation is chosen. Next, the point cloud ($Q$) with unknown orientations is compared with the base point cloud to find the corresponding pairs of points $(p_i, q_j)$ by searching for the nearest points that align between the two point clouds:

$$P = \{p_1.....p_n\} \quad ; \quad Q = \{q_1.....q_m\} \tag{2.22}$$

$$(p_i, q_j) = \underset{i,j}{argmin} \left((x_{p_i} - x_{q_j})^2 + (y_{p_i} - y_{q_j})^2 + (z_{p_i} - z_{q_j})^2\right) \tag{2.23}$$

Then, minimising the summation of the squared error of rotation ($R$) and translation ($T$) of those corresponding points will allow us to estimate the optimal transformation parameters:

$$E(R,T) = \sum_{i=1,\ j=1}^{n,m} (p_i \ - Rq_j \ - T)^2 \tag{2.24}$$

To further optimise the calculation, translation parameters are chosen by taking the centre of mass of the corresponding points of both sets $(M_Q, M_P)$. The centre of the circle is translated from one data set to the other to generate a new point data set:

$$M = M_p - M_Q \tag{2.25}$$

$$p_i^{'} = \{p_i - M\} \tag{2.26}$$

$$E^{'}(R) = \sum_{i=1,\ j=1}^{n,m} (p_i^{'} \ - Rq_j)^2 \tag{2.27}$$

$$R_{optimum} = \underset{R}{argmin}(E'|R) \tag{2.28}$$

A high-level implementation of the algorithm is demonstrated as in Algorithm 3:

**Algorithm 3** Orientation detection

/* FUNCTION PARAMETERS */
$P - base, Q - current$ /* Point clouds*/
$M_P, M_Q$ /* centre of mass */
/* INITIALIZATION OF VARIABLES */
$e_{pre}, R_{optimum}$ /* $e \rightarrow$error, $R \rightarrow$rotation */
$i = 0, i_{max}$ /* $i \rightarrow$iteration */

---

$M : M_P - M_Q$
/* Translate current scan to base scan */
**for all** $p \in P$ **do**
  $p' = p - M$
**end for**
/* Search for optimum rotation */
**while** $(i < i_{max})$ **do**
  $R : Rotate$
  **for all** $j \in 1 : n$ **do**
    $e = e + |p_j^{'} - Rq_j|^2$
  **end for**
  **if** $(e < e_{pre})$ **then**
    $e_{pre} = e$
    $R_{optimum} = R$
  **end if**
  $i++$
**end while**
**return** $R_{optimum}$

## 2.3 Hardware Setup and Software Architecture

The mini-Pipe Inspection Robot (PIRO) system was developed as part of the Sydney Water funded project, "Development of Sensor Suites and Robotic Deployment Strategies for Condition Assessment of Concrete Sewer Walls." It has two main components: a robotic platform and a sensor suite. The robotic platform is equipped with basic pipeline inspection functionalities such as tethered remote control, navigation inside pipes with small water puddles, and CCTV inspection with a flashlight system. The robot is powered and controlled via a 120-m-long tether connected to a control station. The sensor suite consists of an IR laser, cameras, and on-board computer. The mini-PIRO is shown in Fig. 2.8.

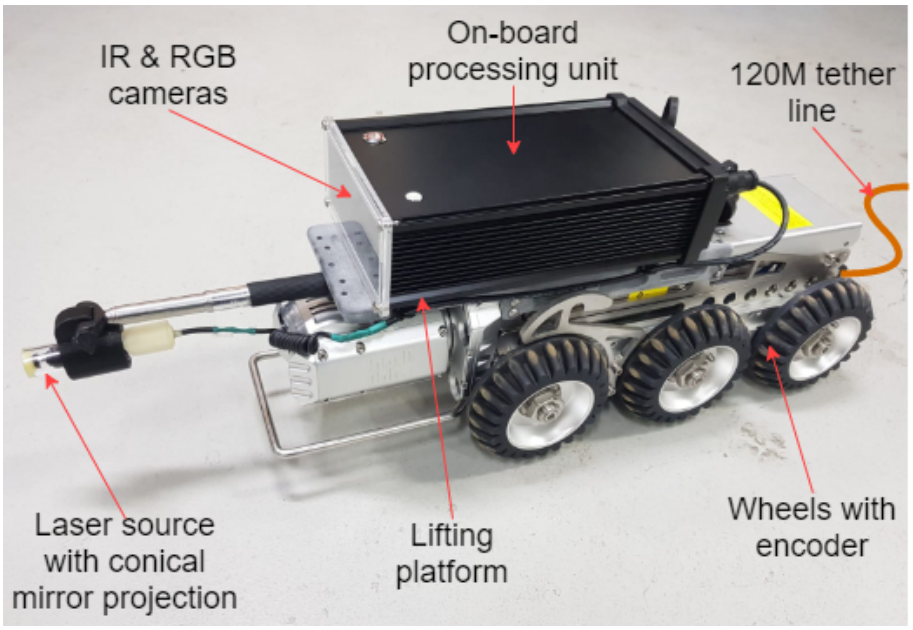


FIGURE 2.8: The mini-PIRO with sensors [3].

### 2.3.1 Sensor Suite

An IR laser and a conical mirror are used to project the circular laser line perpendicular to the pipe wall. The laser probe is mounted at the front end of the robot using a length-adjustable rod. The length of the rod is adjusted to achieve the best laser line visibility for the camera image frames. The laser projection draws a continuous 360 degrees circle over the pipe surface, enabling detection of structural differences throughout the scanning surface area.

The IR laser beam was chosen to lie in the range of the IR camera wavelength so that it is visible in the images. An RGB camera with an IR block filter is used so that the laser ring does not appear in the RGB camera image. All three cameras are configured to $1280 \times 720$ pixel resolution to extract high-definition images at a rate of 30 frames per second. The two IR cameras are used to detect the laser ring projection in the captured images and to generate a stereo-processed point cloud. Since the IR laser is not visible in the RGB spectrum because of the IR filter, the RGB camera image data include colour information for the scanning surface area, which can then be associated with the points generated from the stereo cameras.

As the mini-PIRO is operating in dark underground pipes, the quality of the RGB-D mapping depends on camera exposure settings, laser intensity, and the robot lighting system. IR cameras with IR laser projection work best in dark environments such as pipes. RGB cameras require well-lit environments to capture the true colour. The brightness of the light source may result in over exposure of both IR and RGB camera images. Therefore, the camera exposure values and brightness of the light source need to be carefully chosen for different environments and applications.

An encoder with 1,000 pulses per revolution is embedded into the wheels of the mini-PIRO to track the location of the robot along the pipeline. Although encoders introduce long-term bias into location estimates, at this stage of the application, they work well as the initial intention is to build short-length pipe maps. Tether length can provide another source of information about the location of the robot, which is reasonable at this stage. The algorithms are implemented on a high-performance motherboard with an Intel 2.5-GHz quad-core processor, 8 GB Random-Access Memory (RAM), and a 500 GB Solid State Drive (SSD) internal storage memory. The system was tested extensively and found to operate smoothly over a long period. The whole unit is secured against possible splashes of water to protect the hardware.

### 2.3.2 Software Architecture

The software architecture (Fig. 2.9) is implemented using the Robotic Operating System (ROS) framework based on C++ language and OpenCV libraries for image processing. The computationally heavy functions in the code are modularised and distributed among ROS nodes to work in parallel as separate threads, to improve real-time performance. Since the robot is moving slow (0.2 m/s) to increase the pipe cross section resolution frame rate, the optical flow cause by the movement is very low and negligible. Therefore, the software architecture implementation does not take it into account for simplicity. The raw image frames taken from the cameras are processed using pre-calibrated camera parameters and algorithms implemented using the OpenCV framework, which generates a 2D point cloud of the laser ring that contains the RGB-D vectors. Using the odometry information taken from the robot wheel encoder, 2D point clouds generated from each camera image frames

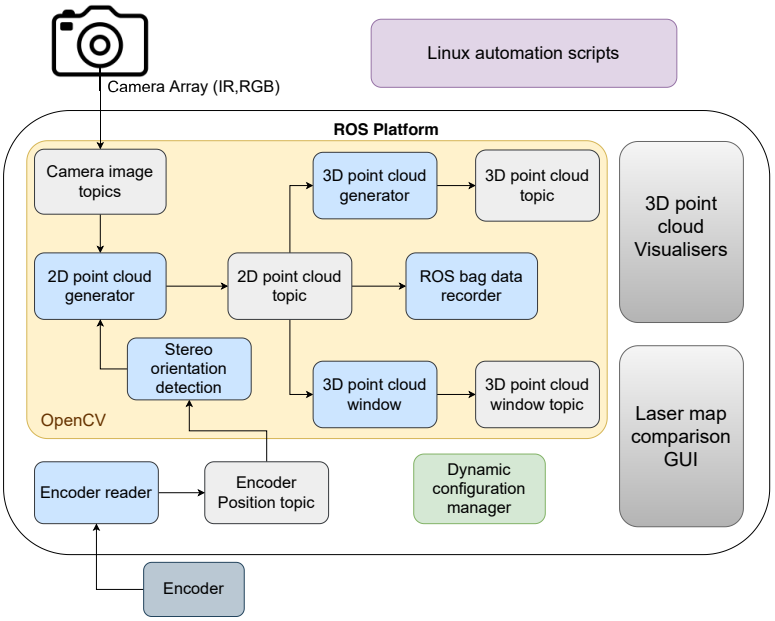


FIGURE 2.9: Software architecture [3].

are iteratively combined to generate a 3D map of the pipe surface. The final results are visualised in real time using ROS Visualisation (RVIZ)-like tools. The system is automated using Linux automation scripts to launch the full system with the single push of a button.

## 2.4 Experiments and Results

The sensor suites and algorithms were tested and validated through a set of experiments conducted in different laboratory setups and in a utility-owned pipe section. The purpose of these experiments was to validate the accuracy of 3D map measurements, RGB-D mapping, defect mapping, orientation detection, and real-time performance of laser profiling, and to evaluate the robustness of the system. The initial experiments were conducted in the laboratory environment using different pipe samples acquired from the field. To test the accuracy of measurements, some pipe samples were planted with artificial defects with known dimensions as the ground truth. Once the system was proven in the laboratory, several field trials were carried out to evaluate the robustness of the system and to collect valuable data.

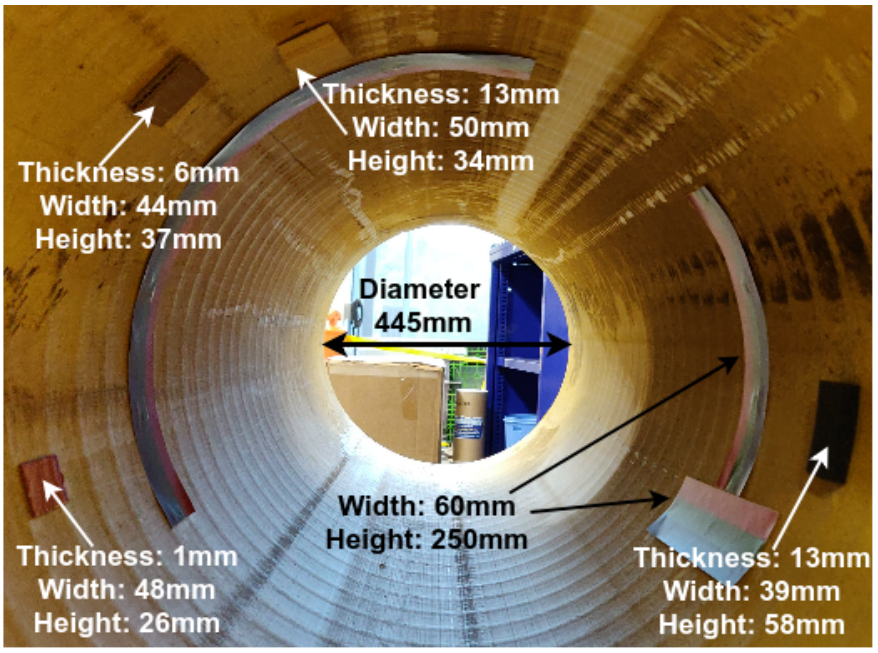


FIGURE 2.10: Storm water pipe with artificial defects with benchmarks used in the laboratory setup to validate sensing performance [3].

### 2.4.1 Sensor Suite Validation

To validate the sensors, a storm water pipe was arranged with artificial defects with known dimensions placed around the pipe surface, to test the accuracy of measurements taken from the 3D map. Fig. 2.10, 2.11g, and 2.11h show the laboratory test environment. Artifacts with different thicknesses were attached to the internal pipe surface to validate the measurements by comparing them with the ground truth (Fig. 2.10). Colour stripes of red, green, and blue were placed on the pipe surface as shown in Fig. 2.10, to enable validation of the colour alignment mapping. The second setup is shown in Fig. 2.11h, and was focused more on validating the 3D measurements by scanning a triangular profile made from styrofoam, as shown in Fig. 2.11g. This setup was carefully designed to provide more detailed measurements for all required metrics.

An example of metric-scaled point clouds generated from the proposed sensor module is provided in Fig. 2.11. Fig. 2.11a shows an RGB-D point cloud generated from the proposed system and Fig. 2.11b shows the unwrapped version of the point cloud generated using an unroll algorithm. The measurements are validated by comparing the point cloud

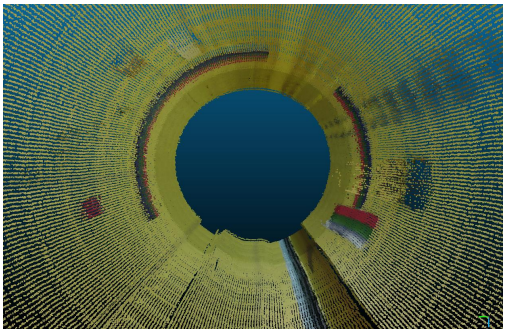

(a) RGB-D point cloud generated from the validation test pipe scan.

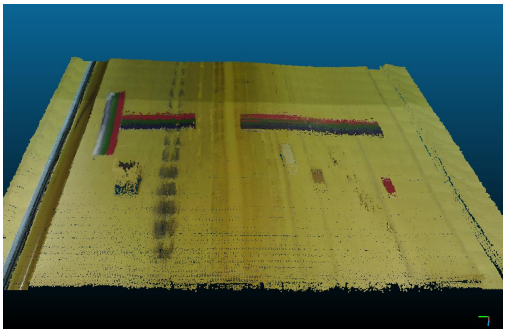

(b) The unwrapped RGB-D point cloud generated from the laser profile.

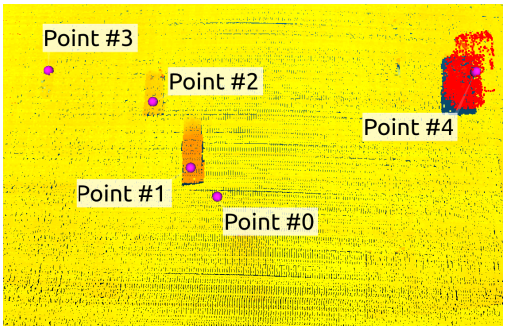


(c) The unwrapped 3D point cloud with the defects heat map.

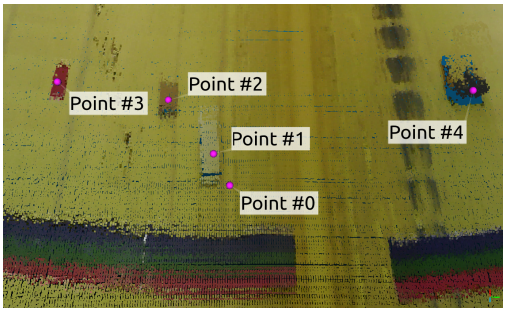


(d) Point cloud defects thickness measurements.

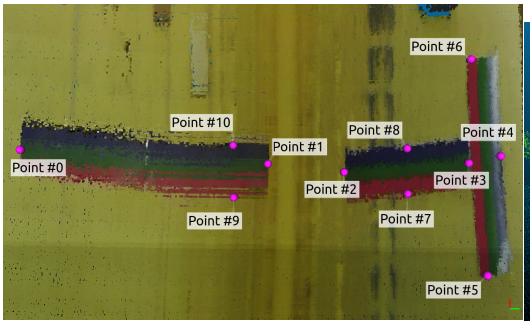


(e) Point cloud defects size measurements.

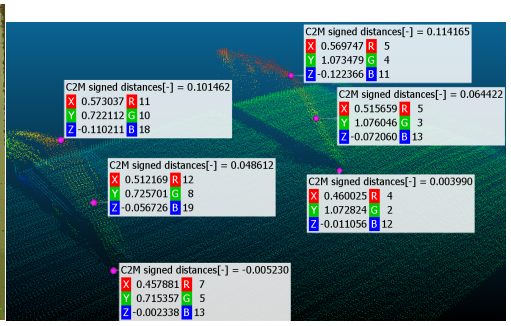


(f) 3D point cloud measurements of the styrofoam artificial defects.

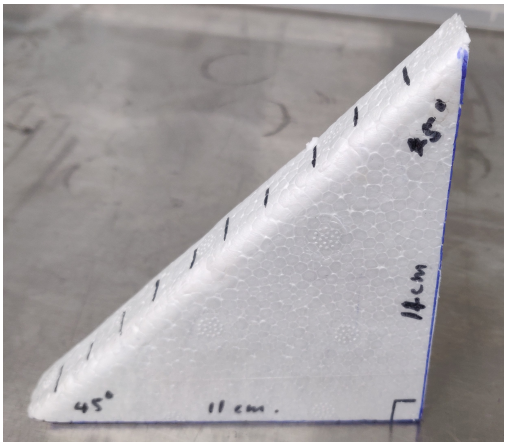


(g) Triangle-shaped artificial defect profile constructed from styrofoam.

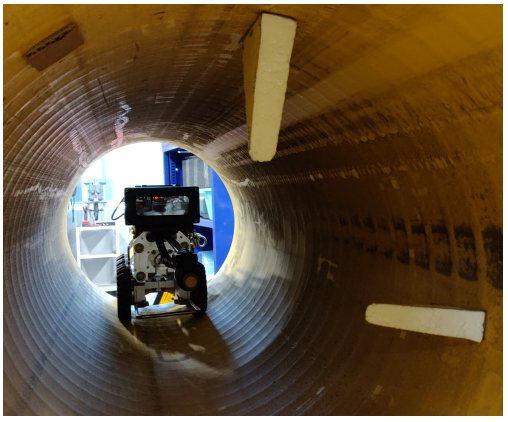

(h) Laboratory pipe scan with the styrofoam artificial defects.

FIGURE 2.11: 3D point cloud measurement accuracy validation [3].

measurements with the actual measurements taken from the physical pipe. Fig. 2.11d and 2.11e show the measurements taken at different locations to validate their accuracy.

### 2.4.2 Measurement Validation

| Location | Physical measurement (mm) | Point cloud measurement (mm) | Error (mm) |
|---|---|---|---|
| Pipe diameter | 445 | 445.36 | 0.36 |
| Fig. 9d Point 1 | 13 | 13.56 | 0.56 |
| Fig. 9d Point 2 | 6 | 6.05 | 0.05 |
| Fig. 9d Point 3 | 1 | 1.68 | 0.68 |
| Fig. 9d Point 4 | 14 | 31.15 | 17.15 |
| Fig. 9e Point 0-1 | 500 | 501.38 | 1.38 |
| Fig. 9e Point 2-3 | 250 | 251.86 | 1.86 |
| Fig. 9e Point 3-4 | 60 | 61.4 | 1.4 |
| Fig. 9e Point 5-6 | 250 | 254.25 | 4.25 |
| Fig. 9e Point 7-8 | 60 | 63.56 | 3.56 |
| Fig. 9e Point 9-10 | 60 | 64.02 | 4.02 |
| Fig. 9h right defect | | | |
| • Height | 110 | 111.31 | 1.31 |
| • Length | 110 | 109.72 | 2.78 |
| Fig. 9h left defect | | | |
| • Height | 110 | 107.87 | 2.13 |
| • Length | 110 | 115.16 | 5.16 |

TABLE 2.1: Evaluating measurements of artificial defects placed on the pipe surface [3].

Table 2.1 presents the most significant validations achieved for the generated point cloud by comparing the point cloud measurements with the known dimensions of defects placed on the pipe. Physical measurements were taken using a laser distance meter and vernier caliper. Several points were randomly selected from the region of interest in the generated 3D point clouds using a point cloud analytical tool, and the average measurement compared with physical measurements. In general, the thickness measurements were accurate to the millimetre level, with some exceptions. For example, point 4 in Fig. 2.11d is erroneous because of the dark colour surface. The black surface absorbs most of the projected IR laser light and thus cameras cannot capture the relevant visual features in that area to generate the 3D points for the cloud. Fig. 2.11e and Table 2.1 show that measurements for points 0–4, taken along the circumference of the surface (on the x-axis of the image), are accurate

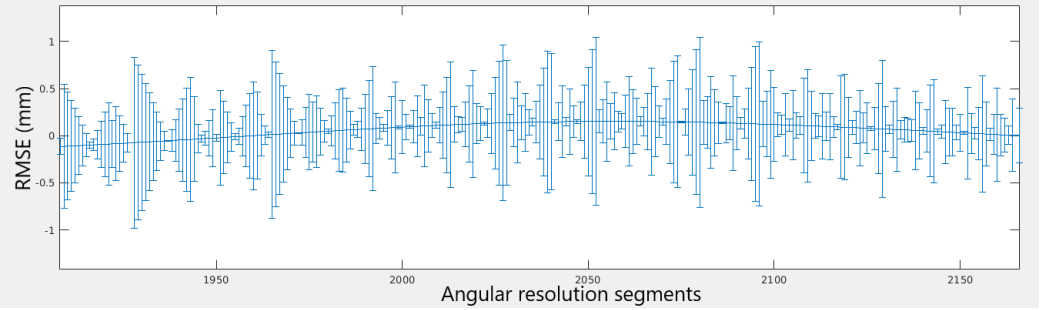


FIGURE 2.12: Root mean square deviation from ground truth [2].

to the millimetre level. However, measurements for points 5–10 (taken on the y-axis of the image) have higher errors caused by the basic odometry received from the lateral movement of the robot. The next stage of the research involves improving robot localisation to address these errors. The last two rows in Table 2.1 (right defect and left defect locations) compare the results taken from the Fig. 2.11f point cloud measurements with the ground truth, which reflects the accuracy of the readings. Fig. 2.11a shows that the colours of the point cloud are perfectly aligned with the locations of the defects, and therefore the RGB-D mapping is accurate to the millimetre level. To further analyse the error deviation across the circumference of the pipe, laser profiling was performed on a brand new 300-mm-diameter polyvinyl chloride Polyvinyl Chloride (PVC) pipe for which precise ground truth measurements are available. Fig. 2.12 shows the test result comparison of the laser profile with the ground truth, with the Root Mean Square Error (RMSE) shown across the circumference of the pipe for each sample period. To minimise costs, the purchased laser ring projector was not the best available on the market. This resulted in some aspects of the error patterns being created by noise from the projector itself.

Fig. 2.11c shows a point cloud that was run through the heat map algorithm to highlight defects on the pipe surface based on their severity. A colour gradient was applied throughout the point cloud to easily identify defects at millimetre-level accuracy. This is the most crucial information for a water utility engineer for identifying and repairing defects in the scanned pipeline. Further, as seen in Fig. 2.13, the proposed solution can highlight wave-like patterns that cannot be seen by the naked eye. These results are discussed in [2].

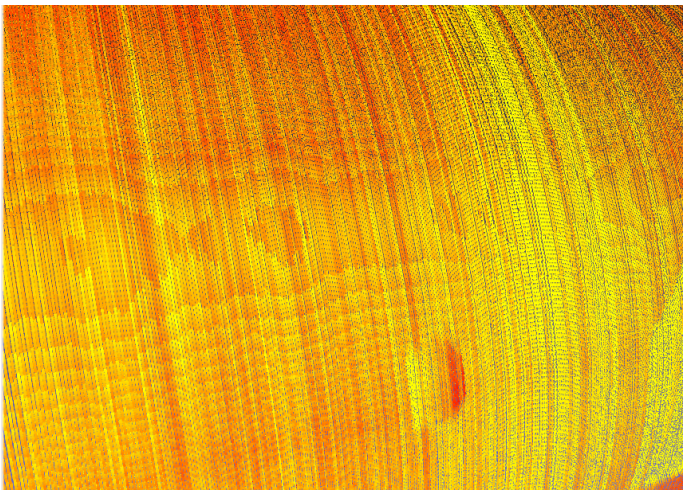

FIGURE 2.13: Features of a PVC pipe that cannot be seen by the naked eye, highlighted by a high-density heat map [3].

### 2.4.3 Performance Evaluation With Existing Technologies

The following outlines a comparative study undertaken with existing methods. A corroded metal drinking water pipe extracted from a Sydney Water network was used to perform these tests (Fig. 2.14a). First the pipe was scanned using a commercially available 3D scanner (Creaform EXAscan 3D scanner model SYS-H3D-EXAD). This scanner generated a 0.1-mm-accurate 3D mesh model, as shown in Fig. 2.14b. However, it was only able to scan a small portion of the pipe because of limited manoeuvrability in a confined space. Next, based on the literature [71–73], another mono camera system scan was performed that generated a 3D point cloud with an accuracy of 7 mm in the best-case scenario. These errors are susceptible to sudden changes in orientation of the robot because of defects in the pipe that a mono camera system cannot detect or correct. Next, the scan was repeated using the proposed stereo vision system, which generated a 3D point cloud with accuracy of 1 mm, as shown in Fig. 2.14c. Then, all the 3D scan models were aligned for comparative purposes (Fig. 2.14d). The accuracy of the methods was validated using a 3D model evaluation software by comparing the measurements with those from a hand-held Creaform scanner 3D model (Fig. 2.14e). The 3D mesh model was generated from the point cloud for the proposed system using third-party software algorithms. Visualising a heat map overlaying the mesh provides a clear indication of the defects (Fig. 2.14f).

| Method / Feature | Mono Camera Laser Profiler System | Creaform handheld 3D scanner | Proposed Laser Profiler System |
|---|---|---|---|
| Measurement Accuracy | 7 mm | 0.1 mm | 1 mm |
| Mobility | Deployable in a robotic platform | Need a human to operate, limited maneuverability | Deployable in a robotic platform |
| Trackers | Doesn't need trackers | Need point markers | Doesn't need trackers |
| Orientation Detection | No orientation detection, slight rotations in robot introduce errors | Detects orientation from marker references | Detects orientation with stereo vision and correct errors |
| Calibration | Need field calibration for each deployment | One time calibration | One time calibration |

TABLE 2.2: Summary of performance comparisons of the proposed system with existing 3D scanning technologies.

Thus, the proposed system overcomes the limitations of other evaluated methods. Table 2.2 summarises the performance comparison results.

### 2.4.4 Orientation Validation

The following tests were carried out to validate the algorithms discussed in Section 2.2.5. As shown in Fig. 2.15 various point clouds were generated by projecting a laser beam at known angles inside the pipe. The first instance (Base) is taken as the reference point cloud for comparison with the rest of the data using the algorithm. The second and third instances are individual rotations of 10 degrees for the Y- and Z-axes, respectively. The fourth instance is rotated by 10 degrees in each of the Y- and Z-axes. The final instance is rotated by 10 degrees along the X-axis.

The generated data were loaded into the algorithm and the results compared with known measurements to estimate accuracy, as shown in Table 2.3.

According to the comparisons, individual axis (pitch, yaw) rotations are accurate with just 0.2 degrees error. When there is a rotation in both the pitch (Y) and yaw (Z) axes at the same time the error increases to 3 degrees. Rotation in the roll (X) axis is ignored as it cannot be detected accurately because of the symmetrical shape of the circular point cloud.

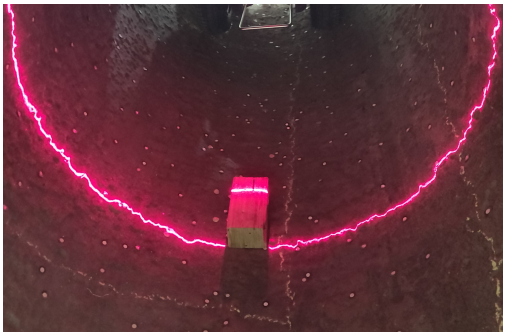

(a) Corroded metal pipe extracted from a Sydney Water network. A red laser was used instead of IR for image demonstration purposes.

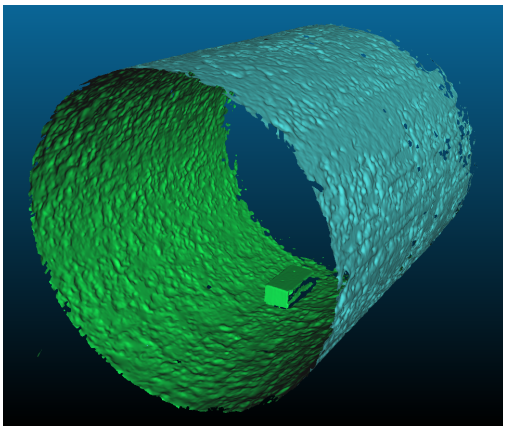

(b) 3D scan generated from a Creaform handheld 3D scanner.

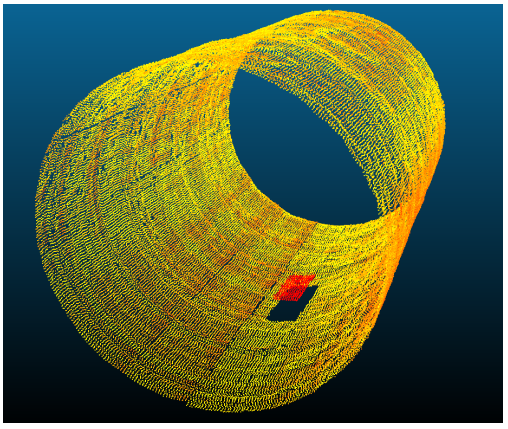

(c) Laser scan generated from the proposed system.

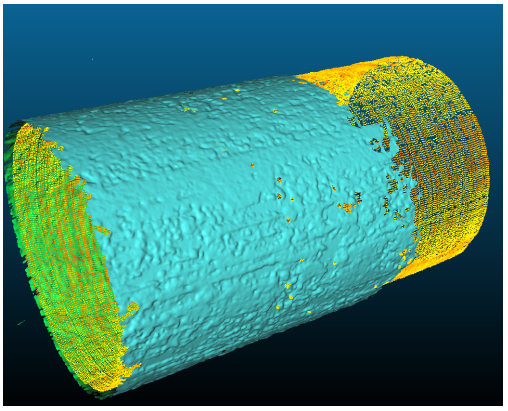

(d) 3D scan and laser scan result comparisons.

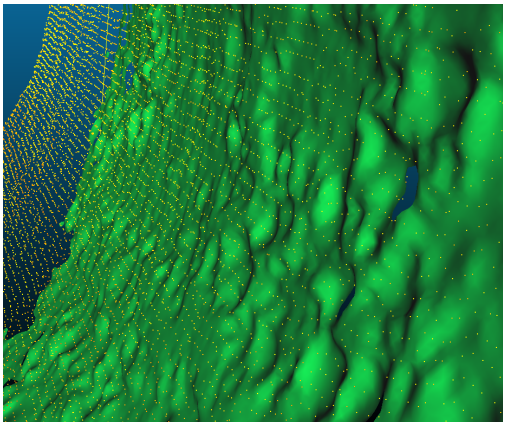

(e) Measurement comparisons.

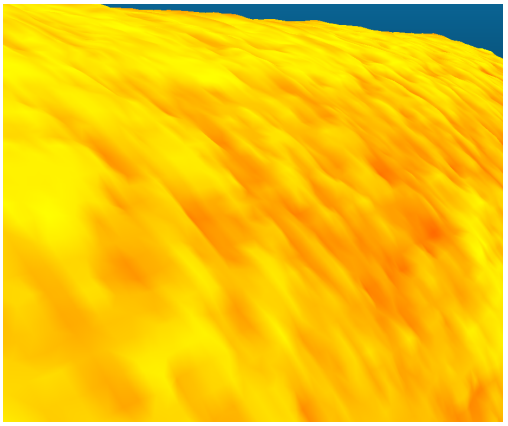

(f) Point cloud for mesh feature validation.

FIGURE 2.14: Ground truth validation using an industrial 3D laser scanner [3].

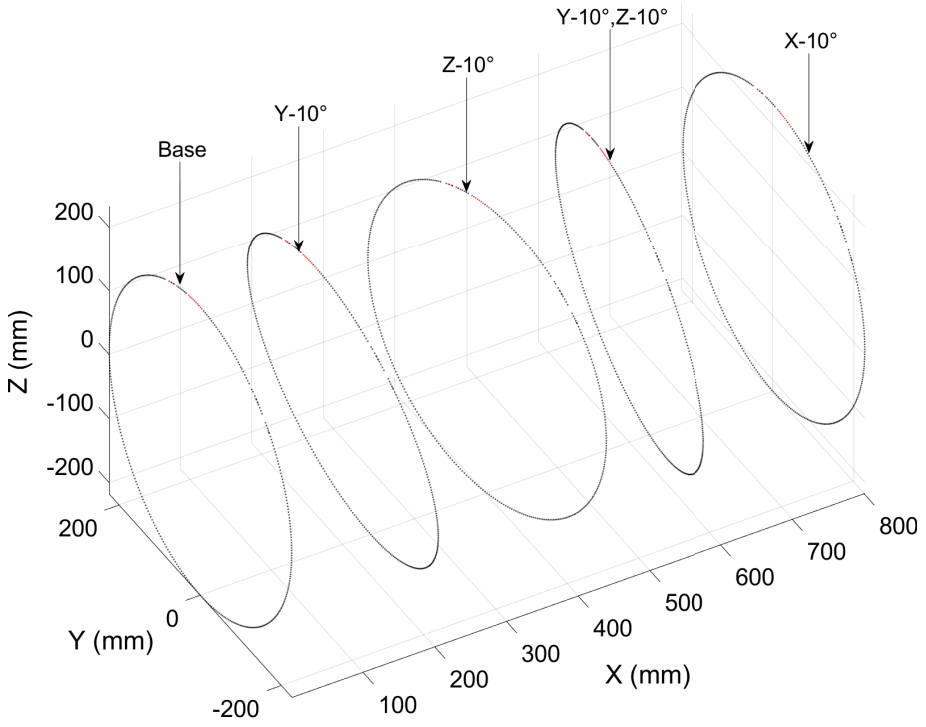


FIGURE 2.15: Test data generated from laser profile scans with fixed known angles to validate the orientation detection [3].

| Physical Orientation (Degrees) | Z Rotation Detection (Degrees) | Y Rotation Detection (Degrees) | X Rotation Detection (Degrees) |
|---|---|---|---|
| Y – 10 | -0.0025866 | 9.851 | -0.015133 |
| Z – 10 | -9.8511 | 0.0025376 | 0.014715 |
| Y & Z – 10 | 7.0537 | 7.0008 | 0.43202 |
| X – 10 | -0.000003 | -0.000003 | 0.021256 |

TABLE 2.3: Evaluating measurements from the orientation algorithm [3].

### 2.4.5 Field Trials and Data

The robot was first tested in a 5 metres long field-extracted pipe sample, as shown in Fig 2.16, to assess its robustness before deploying it in an actual underground pipeline. Fig. 2.16a shows the robot deployment inside the 5 metres long CIPP-lined pipe sample. Fig. 2.16b shows the 3D mesh generated from the point cloud data and Fig. 2.16c shows the unwrapped version of the pipe sample. The results were validated by comparing the point cloud data measurements with physical measurements taken from the pipe sample.

Next, the robot was deployed in real underground Sydney Water pipe networks as shown

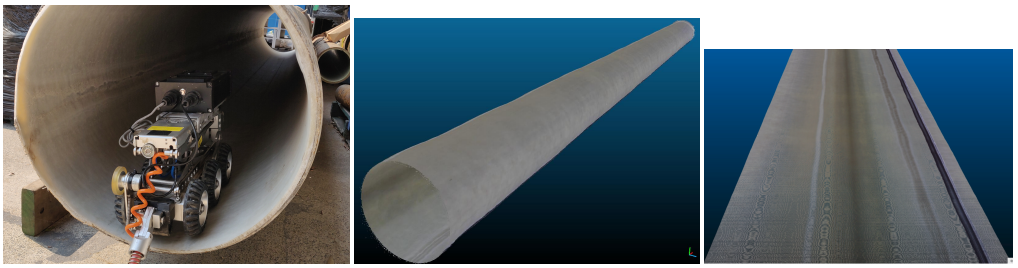

(a) Scanning a sample extracted from an underground water pipeline.

(b) Side view of the generated 3D mesh for the underground water pipe sample.

(c) Unwrapped 3D mesh of the underground CIPP liner water pipe sample.

FIGURE 2.16: Laboratory tests on a field-extracted pipe sample [3].

(a) Preparation for robot deployment.

(b) Deploying the robot into the pipeline.

FIGURE 2.17: Robot deployment in real Sydney Water underground pipeline.

in Fig. 2.17. Lowering of the robot using a crane into the underground pit pipeline opening is shown in Fig. 2.17a. Deployment of the robot into the pipeline is illustrated in Fig. 2.17b. The robot was tested in different underground pipe environments such as spray-liner-coated pipelines, which had shiny surface, and a CIPP-lined pipeline with a relatively rough surface. The robot was deployed in 60 metres long pipelines, in both cases collecting around 120 m of data. Fig. 2.18b shows the robot being deployed in a 60 metres long spray-lined pipeline. The RGB camera feed from the robot is shown in Fig. 2.18b. It further illustrates the corrosion signs at a pipe joint due to liner application

(a) Laser profiling in an actual underground water pipeline.

(b) Camera image of the underground water pipeline with spray liner coating.

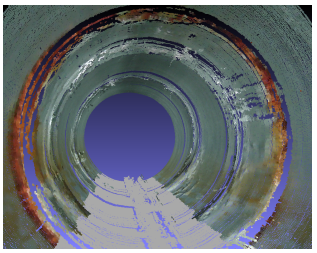

(c) 3D point cloud generated for the underground water pipeline spray liner coating.

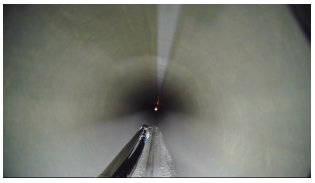

(d) Camera image of an actual underground water pipeline with CIPP liner coating.

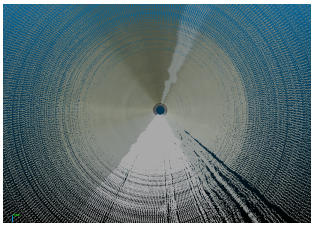

(e) 3D point cloud for the CIPP pipe liner coating.

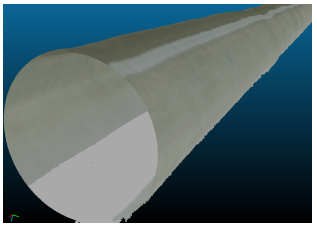

(f) 3D mesh for the CIPP pipe liner coating.

FIGURE 2.18: Field trial with 3D scan results [3].

errors. Fig. 2.18c shows the RGB-D point cloud generated from the system mapping the real colours seen on the pipe surface. It further illustrates the liner application errors seen in Fig. 2.18b accurately captured using the generated point cloud with true colours and dimensions. Fig. 2.18d shows robot deployment in the 60-m CIPP-lined pipeline. The RGB-D point cloud generated from the system can be seen in Fig. 2.18e. Fig. 2.18f shows the 3D mesh for the scanned pipe generated offline using the point cloud data collected during the real-time scan. This mesh is used later for visualisation in a virtual reality system to enable further inspection, which provides a user experience similar to traversing the pipeline.

#### 2.4.5.1 Graphical User Interface

As a post-data processing procedure, a Graphical User Interface (GUI) was developed, as shown in Fig. 2.19, to inspect and compare the data maps created in various trials. The main role of this GUI is to measure the quality of pipe maintenance by comparing the laser profile data gathered before and after application of pipe liners. It can compare post-lining with pre-lining laser profile data. This enables inspection and comparison of data

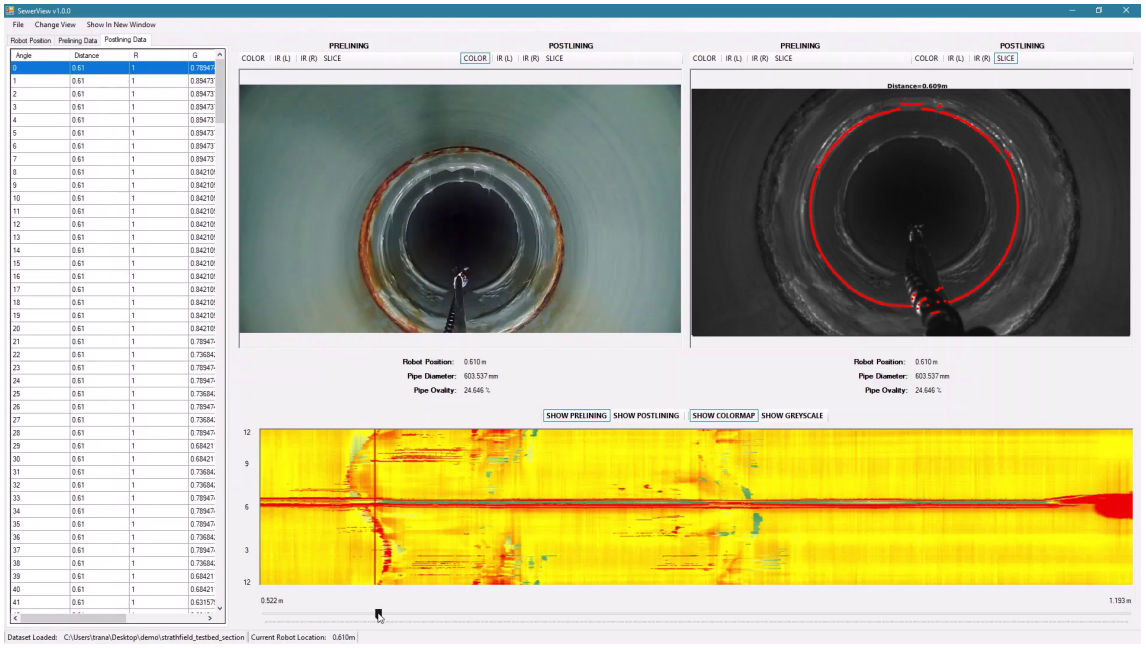


FIGURE 2.19: GUI developed to inspect laser profile data and compare pre-lining and post-lining data sets

gathered at different times to monitor the evolution of damage to underground pipeline infrastructure. Further, it can identify ovality changes in the pipeline, and produce CCTV data, IR camera data, pipe defect heat map, and pipe measurements for every frame. The interface was developed for easy use by third-party users. It was verified that millimetre-level accuracy can be achieved from the system. The ability to measure pipe surface changes accurately is important in pipe defect identification and quantification.

### 2.4.6 Real-time Performance

The system is implemented in ROS using its modularising capabilities to capture images at 30 frames per second (fps) from all three cameras in parallel while running the robot inside pipelines. While the robot is in motion, the 30 frames per second frame rate provides a higher resolution along the pipe axis cross sections when generating the point cloud. The higher the frame rate, the higher the resolution in the longitudinal direction. The hardware used in the prototype provides a maximum of 30 fps frame rate with high-definition image resolution. In normal inspections, the robot runs inside the pipeline at a speed of 0.2 m/s while generating a real-time point cloud Fig. 2.20. When in-depth inspection becomes

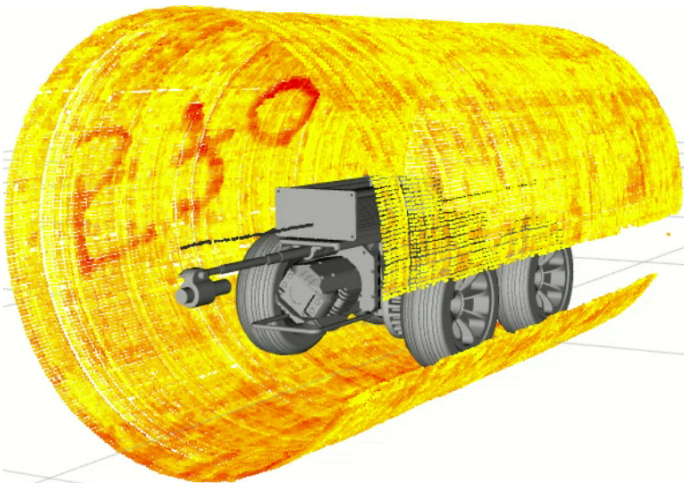

FIGURE 2.20: Real-time 3D scan view from the software interface with heat map mode enabled [3].

necessary, the robot runs at a slower speed to create a 1 mm accuracy point cloud. This slow travel speed is required to increase accuracy. However, running at higher speed will only reduce point cloud resolution; it will not affect real-time system performance. Further information can be found in [2, 3]. Having real-time inspection capability is advantageous during robot deployment as it provides the chance to further scan and gather more data around regions of interest. This reduces the number of cycles of robot redeployment significantly. Further, having the RGB-D information to gather colour values on the pipe surface provides more information about defective areas, such as the degree of pipe surface corrosion, as seen in Fig. 2.18b and Fig. 2.18c.

## 2.5 Summary

This chapter has presented the design and development of a robotic sensing system for RGB-D mapping inside drinking water pipes. The proposed system utilises an IR stereo camera vision system and an IR laser pattern projection-based sensing system along with encoders for robot localisation. The data gathered are used to build true colour 3D maps identifying defects and achieving millimetre-level accuracy. The system was first comprehensively tested in laboratory settings, followed by field trials in a drinking water pipeline in Sydney, Australia for performance evaluation. The experimental results indicated that a 3D map generated for the internal pipe surface had millimetre-level

accuracy and could efficiently detect changes in pipe ovality, and indicate surface corrosion.

The current version of the robotic sensing system was developed for pipes ranging from 400 to 700 mm in diameter. In the future, the system could be extended to develop a robotic system for pipes less than 400 mm in diameter. When the pipe wall has obstructions to the laser projection from the camera, a shadowing effect occurs in the laser profile. Future research could address this issue by means of adding/changing cameras from different angles. Further research might be done to address the limitation discussed in this chapter, whereby black surfaces present low measurement accuracy. This could be overcome by utilising a high-intensity laser.

The proposed solution works well for short-range monitoring with millimetre-level accuracy but, as stated in the 2.3.1 section, when it comes to long-range pipe scans in the field, accuracy in the longitudinal direction decreases with travel distance because of limitations in accurate robot localisation due to the commonly used standard wheel or tether line encoder-based localisation methods for crawler robots. Encoders are effective for localisation tasks over a short distance (several meters) because they are associated with negligible errors, but when it comes to long-distance travel, errors accumulate, which increases uncertainty and invalidates the localisation of defects. This will result in difficulty in defect localisation and alignment of defects required to analyse their evolution by comparison between scans taken at different times. Further, the scanning direction or the entry point to the pipe layout may change over time to accommodate maintenance requirements; therefore errors will be inconsistent, resulting in defect alignment impossible in practice. Hence, in the next chapter a better localisation system for long-range, in-pipe robots is discussed.

The following publications are the outcome of work presented in this chapter:

1. **A. Gunatilake**, L. Piyathilaka, A. Tran, V. K. Vishwanathan, K. Thiyagarajan, and S. Kodagoda, "Stereo Vision Combined With Laser Profiling for Mapping of Pipeline Internal Defects," IEEE Sensors Journal, vol. 21, no. 10, pp. 11 926–11 934, 2021.

2. **A. Gunatilake**, L. Piyathilaka, S. Kodagoda, S. Barclay, and D. Vitanage, "Real-Time 3D Profiling with RGB-D Mapping in Pipelines Using Stereo Camera Vision and Structured IR Laser Ring," in 2019 14$^{th}$ IEEE Conference on Industrial Electronics and Applications(ICIEA), 2019, pp. 916–921, doi: 10.1109/ICIEA.2019.8834089.

# Chapter 3

# UHF-RFID Sensor Based In-pipe Robot Localisation

## 3.1 Introduction

This chapter presents a solution to the limitations related to robot localisation inside pipelines, as outlined in the Chapter 2.1 summary. One of the major requirements in the CRC-P project is to monitor the evolution of pipe defects identified by the robot. This requires the robot to be deployed at different times inside the pipeline to collect laser profile data and compare them to identify and quantify the evolution of defects. To compare defects, the laser profile scan regions for those defect locations must be properly aligned using robot localisation parameters. The current robotic platform, which utilises the laser profile solution proposed in Chapter 2.1, uses standard, commonly used encoder-based odometry data to localise the robot because most crawler robots used to monitor and repair underground infrastructure use standard wheel or tether line encoder-based localisation methods. This solution works well for short-range pipe scans where defects can be properly aligned to enable comparison of measurements, because encoders are effective for localisation tasks over short distances (several metres) because they produce negligible errors. However, for long-distance travel in a pipeline, the errors produced by the encoder

accumulate, which increases uncertainty and invalidates robot localisation information. This means that alignment of defects for measurement comparison is impossible.

Pipes may be very slippery for crawler robots because of the presence of water puddles and mould, rendering the traditional technique of utilising wheel odometers for in-pipe robot localisation inaccurate in terms of positioning estimates [8]. Dead reckoning techniques based on IMU, employing magnetometers and accelerometers to provide absolute measurements of the heading and downward direction are not suitable for in-pipe robot localisation, primarily because the magnetometer component cannot provide an accurate measurement of heading angles and can lead to drift [35]. In [80], the location of the robot along the pipe was determined by the length of the cable from the entrance of the pipeline to the current location of the robot. Similarly, method proposed in [81] combined IMU data with tethered cable encoder data to calculate the distance travelled by the in-pipe robot. Although reliable for short-distance inspections, such methods are unreliable for long-distance inspections owing to the cables' proclivity to bend or coil during the inspection process. Several studies have evaluated the use of Extreme Low Frequency Electromagnetic Pulse (ELF-EP) in-pipe localisation [47, 82, 83], but some required sensors stationed outside the pipe, which is not very practical. Further, sensor accuracy may be affected by the metallic pipe environment. GPS, which can determine robot positions outdoors and in most indoor environments, is disturbed by pipeline environments [34], where the robot has little to no connectivity with GPS [84, 85]. To overcome limitations associated with the aforementioned techniques, researchers have proposed visual odometry techniques such as visual SLAM utilising stereo cameras [86], monocular cameras [87–89], RGB-D sensors combined with machine learning algorithms [90], and a monocular fisheye camera [91] for in-pipe robot localisation. These visual odometry methods work well when there is a sufficient number of identifiable surface features or imperfections inside the pipeline; however, in the context of the current work, pipes can appear symmetrical and have a limited number of discernible surface features after the application of linings. To overcome the constraints of visual odometry within pipes, researchers [35, 92, 93] have proposed using ultrasonic sensors to measure the soil profile through the pipe wall for localisation. Although this technique works well for plastic pipes, metallic pipes may present a significant challenge

depending on their size, and not all drinking water pipes are underground; there are also above ground pipelines. Other studies have elaborated on SLAM methods utilising acoustic sensors [94–98]. They may not work in metallic pipes and in situations where pipes are in the operational state, in which case water may absorb the sound waves, further decreasing accuracy. Therefore, a different and more efficient contactless localisation method is needed.

Currently, many wireless technologies and algorithms are under study for localisation in outdoor and indoor environments [99–105]. In recent research RFID, localisation technology has produced good localisation results for indoor environments [106, 107]. This is a cost-effective solution that is being researched for its ability to monitor environmental conditions such as temperature, moisture, and acidity levels inside pipelines, by embedding them as liner-embedded sensing technologies [108–110]. An additional use of this technology might be as an effective contactless and wireless localisation method that will not become dependent on environmental changes in the pipe over time. In this way, RFID becomes more suitable for localisation using UHF-RFID wireless signal processing. However, little research has focused on accurate underground pipeline localisation using RFID signals and such studies have produced information that is insufficiently accurate [93, 111, 112]. Unlike outdoor/indoor RFID localisation, where the highest peak of the signal strength is the most likely location of the RFID tag [105, 113], inside the pipeline, according to the simulations presented in Section 3.3.2.1, the signal behaves uniquely, in that it bounces off the pipe surface producing a ripple effect on the signal strength and creating multiple peak points [4, 5]. Further, Commercial Off the Shelf (COTS) RFID readers provide vague and uncertain measurements, making them capable only of localising the RFID tag with square-metre accuracy [114]; hence rendering the localisation task challenging and unique.

In this chapter, an improved localisation method is proposed for underground water pipelines using COTS RFID components with a GP combined Particle Filter (PF) algorithm [115, 116] that employs both RSSI and phase data in the measurement model to achieve higher accuracy. Experiments were conducted in field-extracted water pipelines from the Sydney Water network to identify the best RFID tags for the task and best locations to deploy the RFID tags inside the pipe. The results showed that the

proposed system achieved a precision of approximately 15 cm with a single antenna model. To further improve accuracy, the signal behaviour of a two-antenna sensor model was studied, and by improving the measurement model, localisation accuracy was enhanced to millimetre level.

The key contributions of this chapter are:

- First, a UHF-RFID signal-based robotic localisation system is presented that uses a particle filter combined with a GP algorithm. The accuracy of the localisation is further enhanced by utilising Phase data in addition to RSSI data in the particle filter measurement model.
- Second, the system can be used for robot localisation without the aid of any other odometry systems after creating an initial measurement model, and can accurately localise the robot to the millimetre level.
- Third, the system is capable of aligning the laser profile scans taken at different times with millimetre-level accuracy to map the corresponding defects in each 3D profile and monitor their evolution. The solution was tested in sample laboratory pipes extracted from the Sydney Water network, simulating a 50 metres length.

The remainder of this chapter is organised as follows: Section 3.2 presents the problem formulation. A single-RFID-antenna sensor model for robot localisation is then evaluated in Section 3.3. To improve the localisation results, Section 3.4 presents a twin-antenna sensor model. Finally, Section 3.5 summarises the main contributions of the chapter and the research outcomes.

## 3.2 Problem Formulation

The initial simulations and experiments showed that in the open environment, RFID localisation is somewhat straightforward because the signal strength curve contains only one peak point, which relates to the most likely location of the robot [113]. However, inside a pipe environment the signal strength curve has multiple peak points, making the

robot location uncertain and the localisation task unique and difficult. Results in Fig. 3.6 comparing data on the location of Tag A inside and outside the pipe show how the signal behaves differently in these two environmental conditions.

The RFID RSSI data and Phase data are first collected from the robot. The fading effects of RSSI are significant in outside (outdoor, indoor) environment applications due to the presence of obstacles. However, inside metallic pipe environments, the signals behave somewhat different and therefore the fading effect is not so strong. Hence, the unique signal pattern seen on the collected RSSI data, can be modelled using a GP. GPs are ideal for complex likelihood models for a number of reasons: for example, they do not require a representation of the environment; they are non-parametric models; they provide uncertainty estimates, unlike other regression models; and the parameters can be learned using training data [117–123]. Therefore, to filter out outliers, normalise the data, and create a measurement model, GP regression modelling is used [117, 124].

Particle filter has many advantages for RFID based localisation including the feasibility of handling complex motion and observation models and it can be scaled well using parallelism. It further works for any dimensional systems as it is independent of the system size. Particle filter has been used with RFID for robot localisation in the literature [107, 125–135]. There are instances reported where the RFID RSSI measurement model of the particle filter is improved by applying GP data [115, 116, 136].

### 3.2.1 Particle Filter Based In-Pipe Localisation Method

Let $x_t \in R^{d_x}$ be the robot's location (hidden variable) at time $t$ and $z_t \in R^{d_z}$ conditioned to both RSSI and phase signal measurements received at time $t$. The observation model can be defined as in Equation 3.1 and Equation 3.2:

$$x_t = g(x_{t-1}, \omega_t) \tag{3.1}$$

$$z_t = h(x_t, v_t) \tag{3.2}$$

where $g : R^{d_x} \times R^{d_\omega} \rightarrow R^{d_x}$ and $h : R^{d_x} \times R^{d_v} \rightarrow R^{d_z}$ are known functions; $p(x_t|x_{t-1})$ and $p(z_t|x_t)$ are probability distributions obtained from $\omega_t \in R^{d_\omega}$ and $v_t \in R^{d_v}$ that are white-noise independent of each other. The recursive form of filtering the sequential estimates of distribution states at time $t-1$ can be defined as in Equation 3.3:

$$p(x_t|z_{1:t}) \propto p(z_t|x_t) \int p(x_t|x_{t-1}) p(x_{t-1}|z_{1:t-1}) dx_{t-1} \tag{3.3}$$

To filter the sequential estimates of distribution at time $t-1$, a number of $N$ particles are generated and distributed inside the pipe section in the form of $X_{t-1} = \left\{ x_{t-1}^{(n)} | w_{t-1}^{(n)} \right\}_{n=1}^{N}$, where $w_{t-1}^{(n)}$ are the weights generated for the particles. The distribution is approximated using Equation 3.4:

$$p(x_{t-1}|z_{1:t-1}) \approx \sum_{n=1}^{N} w_{t-1}^{(n)} \delta \left( x_{t-1} - x_{t-1}^{(n)} \right) \tag{3.4}$$

where $\delta()$ is the Dirac delta function. Following this, an approximation of $p(x_t|z_{1:t})$ can be defined as in Equation 3.5:

$$p(x_t|z_{1:t}) \propto p(z_t|x_t) \sum_{n=1}^{N} w_{t-1}^{(n)} \; p \left( x_t | x_{t-1}^{(n)} \right) \tag{3.5}$$

Unlike the RSSI data, which show a unique signal pattern that can be mapped to a GP function, the phase data are somewhat noisy (Fig. 3.7). Therefore, different weight sets are generated to give high priority to the RSSI data and low priority to the phase data. Finally, they are combined to create an improved measurement model. Therefore, for a given particle defined above, assuming there is no correlation between RSSI and phase values, the weight ($w$) is generated as in Equation 3.6:

$$w = mean \left( \left[ \left| \begin{bmatrix} z_g^* \\ z_h^* \end{bmatrix} - \begin{bmatrix} z_g \\ z_h \end{bmatrix} \right| + \begin{bmatrix} \xi \\ 0 \end{bmatrix} \right] \times \begin{bmatrix} c & 0 \\ 0 & (1-c) \end{bmatrix} \right) \tag{3.6}$$

where $z_g$ is the predicted RSSI measurement from the GP model formulation in Section 3.2.2 that maps to the particle; $z_h$ is the raw phase signal measurement from the model that maps to the particle; $z_g^*$ and $z_h^*$ are the RSSI and phase measurements received from the robot at a particular instant; $\xi$ is the uncertainty that comes from the GP measurement;

and $c$ is a normalisation parameter capturing the different noise levels of RSSI and phase values.

As the GP models are learned independently for each RFID tag from each antenna, the resulting predictions can lean towards over-confident estimates. To prevent such a phenomenon, the likelihood model is smoothed using Equation 3.7:

$$p(z_{t[1:n]}|x_t) = \left(\prod_{i=1}^{n} p(z_{t[i]}|x_t)\right)^{\gamma} \tag{3.7}$$

where $\gamma$ *is* the smoothing coefficient, which lies between 0 and 1.

#### 3.2.1.1 Particle Resampling

Let $S_{t-1} = \left\{\left\{x_{t-1}^{(n)}, w_{t-1}^{(n)}\right\}, z_t\right\}$ be the state at $(t-1)$ that contains a set of particles and weights. $z_t$ are the measurements sensed from the robot at time $t$. The following procedure is iteratively executed for $i = 1, 2, ...n$, where $S_t = \emptyset$ is the new set and $\gamma$ is the normalisation factor for weights:

- Sample index $\hat{i}$ from discrete distribution given by $w_{t-1}$.
- Sample $x_t^i$ from $p(x_t|x_{t-1})$ using $x_{t-1}^{\hat{i}}$
- Reweight $w_t^i = p\left(z_t|x_t^i\right)$
- Update factor $\gamma = \gamma + w_t^i$
- Update new states $S_t = S_t \cup \left\{x_t^i, w_t^i\right\}$
- Normalise weights $w_t^i = \dfrac{w_t^i}{\gamma}$ for $i = 1, 2, ...n$

### 3.2.2 Gaussian Process-based Measurement Model

Function–space view modelling was used to derive the GP, as described in [137]. Let $S = \{(x_1, y_1), (x_2, y_2), ..., (x_i, y_i), ..., (x_n, y_n)\}$ be the set of noisy RSSI training data samples, where $x_i$ is the robot position and $y_i$ is the corresponding RSSI value received by the

robot. The prediction model relating to the robot's location and the RSSI measurement can be learned in the form of function $f$ as in Equation 3.8:

$$y_i = f(x_i) + \epsilon \tag{3.8}$$

where $\epsilon$ is the zero mean Gaussian noise with a known $\sigma_n^2$ variance. Since the robot's movements are considered to occur only along the axis of the pipeline, all input values $x_i$ can be aggregated into vector $\mathbf{x}$ and all target $y_i$ values can be aggregated into vector $\mathbf{y}$.

GP enables correlation of the RSSI signal strength function values at different data points where the covariance of $f(x_p)$ and $f(x_q)$ values depends on the robot location input values of $x_p$ and $x_q$. This relationship can be learned in the form of a kernel $k(x_p, x_q)$ to generate the training data model. The squared exponential kernel is selected to learn the non-linear regression problem, which is defined as in Equation 3.9:

$$k(x_p, x_q) = \sigma_f^2 \; exp\left\{-\frac{1}{2\beta^2}|x_p - x_q|^2\right\} \tag{3.9}$$

where $\beta$ and $\sigma_f^2$ are hyper-parameters. $\beta$ is the scale parameter that estimates how well the kernel fits between data points and $\sigma_f^2$ is the parameter that determines function smoothness.

Once the data are trained, the kernel returns noisy signal observations based on robot location input parameters. Therefore Equation 3.10 defines the covariance of the noisy signal observations for the corresponding function:

$$cov(y_p, y_q) = k(x_p, x_q) + \sigma_n^2 \delta_{pq} \tag{3.10}$$

where $\delta_{pq}$ is either one or zero depending on $p = q$, and $\sigma_n^2$ is the observation noise. For all robot locations $\mathbf{x}$ the corresponding covariance function observations $\mathbf{y}$ can be defined as in Equation 3.11:

$$cov(\mathbf{y}) = \mathbf{K} + \sigma_n^2 I \tag{3.11}$$

$$\mathbf{K}[p, q] = k(x_p, x_q) \tag{3.12}$$

where $\mathbf{K}$ is the covariance matrix for all data inputs $\mathbf{x}$.

Let $x_*$ be an arbitrary robot location, where the RSSI signal strength needs to be estimated based on the function value $f(x_*)$ from training data $\mathbf{x}$ and $\mathbf{y}$. The posterior distribution $\mu_{x_*}$ and the associated uncertainty $\sigma^2_{x_*}$ can be calculated as in Equation 3.13 and Equation 3.14:

$$\mu_{x_*} = \mathbf{k}_*^T \left(K + \sigma_n^2 I\right)^{-1} \mathbf{y} \tag{3.13}$$

$$\sigma^2_{x_*} = k(x_*, x_*) - \mathbf{k}_*^T \left(K + \sigma_n^2 I\right)^{-1} \mathbf{k}_* \tag{3.14}$$

where $\mathbf{k}_*$ is a covariance vector from the matrix $\mathbf{K}$ for corresponding input values.

Further, in GP when estimating hyper-parameters, to minimise the negative log marginal likelihood, Equation 3.15 is used:

$$\log\ p(\mathbf{y}|\mathbf{x}, \theta) = -\frac{1}{2}\mathbf{y}^T \left(K + \sigma_n^2 I\right)^{-1} \mathbf{y} - \frac{1}{2}\ \log\ |K + \sigma_n^2 I| - \frac{1}{2}\ \log\ 2\pi \tag{3.15}$$

where $\theta = \left\{\sigma_n^2, \beta, \sigma_f^2\right\}$.

## 3.3 Single-UHF-RFID Antenna In-pipe Robot Localisation

Understanding of the signal behaviour is important in developing localisation systems. Therefore, a simulation study was performed to study the behaviour of the UHF-RFID signal inside metallic pipelines. A single UHF-RFID antenna prototype model was then designed and developed for deployment via a crawler robot in a field-extracted pipeline from the Sydney Water pipe network. Experiments were performed to study the feasibility of the model and suitable hardware configurations, RFID sensor arrangements inside the pipeline, and function parameters.

### 3.3.1 Development of an In-pipe Robot System

#### 3.3.1.1 Hardware Development

The sensor suite was built with COTS RFID components. A Thingmagic M6e Micro-LTE UHF 2 port RFID reader module with the embedded developer kit was used to implement the proposed system as it was easy to customise and actively supported by the open source Python MercuryAPI software community. A single 915 MHz General Purpose Panel RF antenna in the 902–928 MHz range with 5.5 dBi gain was used to support the module. Three of the most commonly available chip-based RFID tag types (Fig. 3.5) were used to conduct experiments to evaluate and identify the most suitable tag type for the proposed system to achieve the best results. A Jetson Nano Developer kit board with Quad-core ARM 1.43 GHz Central Processing Unit (CPU), 4 GB 64-bit Low-Power Double Data Rate (LPDDR)-4 RAM was used as the central processing unit to run the implemented system. The whole hardware system was assembled inside an enclosure and mounted on top of a robotic platform for deployment, as shown in Fig. 3.1. A rotary encoder with 1,024 pulses per revolution was fixed to the robot wheels to collect odometry data from the robot for validations.

#### 3.3.1.2 Software Development

The components of the software architecture (Fig. 3.2) are implemented using the ROS framework to gain the flexibility to modularise each component, as well as cross-language software support. Each individual component is implemented as a ROS node to make them communicate with each other effectively. As the RFID hardware module is supported with a Python Mercury API library, the RFID reader module is implemented with Python. To gain more flexibility and structure for the implementation, the core integration and algorithms are implemented as C++ components. The robot wheel encoder electronics that receives the initial odometry data to create measurement maps for the particle filter is implemented using Arduino components. Finally, the estimated particle filter localisation predictions based on the previously trained measurement maps are displayed on RVIZ-like visualisation systems. At initial deployment, the robot collects RFID and odometry data

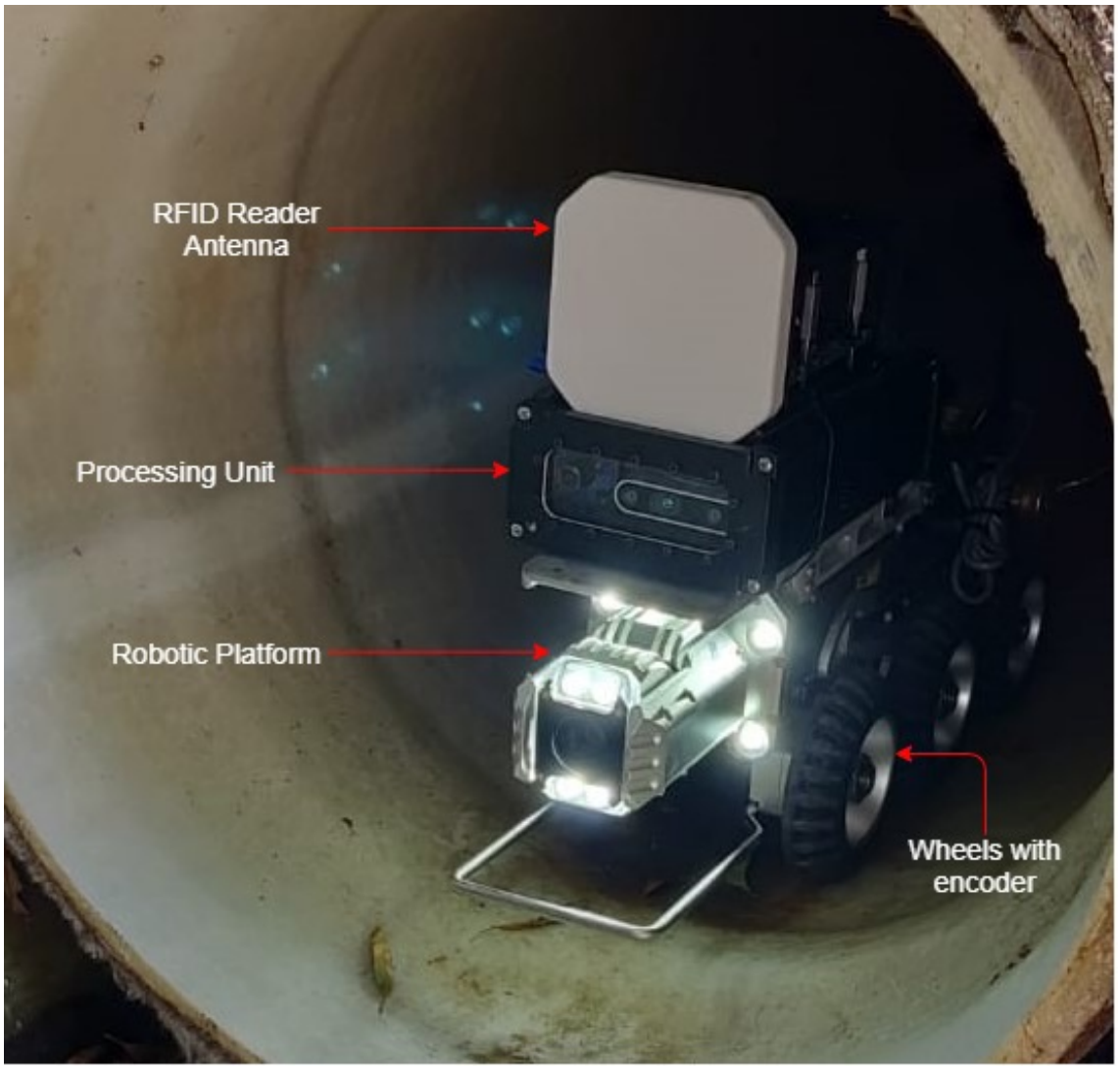


FIGURE 3.1: Robot with a single UHF-RFID antenna sensor model mounted on top [4].

to publish as ROS topics, which are used to generate the measurement models. In following deployments, when the system does not have the wheel odometry data, the particle filter is able to localise the robot using the RFID data and the measurement model.

### 3.3.2 Experiments and Results

#### 3.3.2.1 Electromagnetic Field Simulation

Fig. 3.3 shows the simulation results from the use of CST Studio simulation software. The first simulation was carried out in the open environment using a designed UHF-RFID

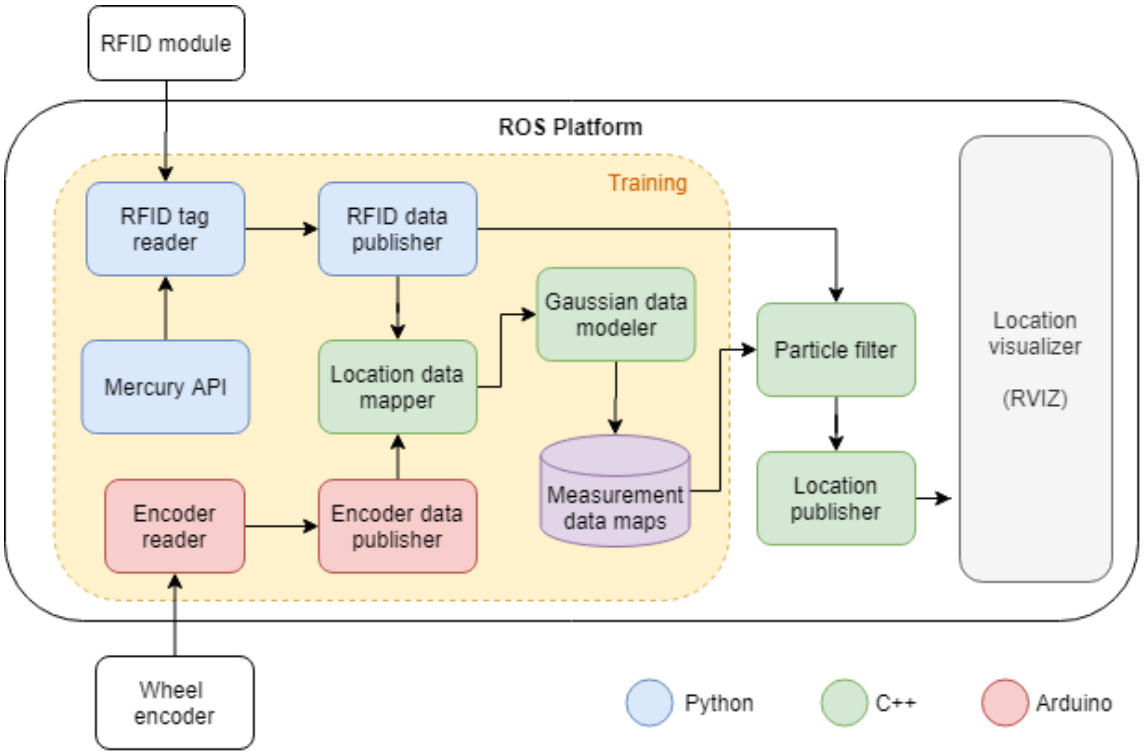


FIGURE 3.2: Software architecture [4].

antenna with hardware configurations that match those of the actual antenna used in practical experiments. The signal strength of the antenna was distributed evenly across the space as an expanding radial field that decays along the distance, as shown in the results (Fig. 3.3a). The same antenna was then moved inside a metallic pipe setting for the next simulation. The signal is reflected from the pipe surface and travels further, as seen in the results (Fig. 3.3b), giving the signal strength a ripple effect. This implies that signals move farther and behave differently within a pipe environment, making the RFID localisation task unique and challenging. Following the observation of these patterns, functional experiments were conducted to explain the findings.

#### 3.3.2.2 RFID Tag and Location Selection

Chip-based, battery-free RFID tags were chosen for the experiments because they can be uniquely identified using the Electronic Product Code (EPC) value and they can be further used to store extra information. Three different chip-based UHF-RFID tags (Fig. 3.5) were tested to identify the tag that led to the best RFID localisation results: oil-impregnated

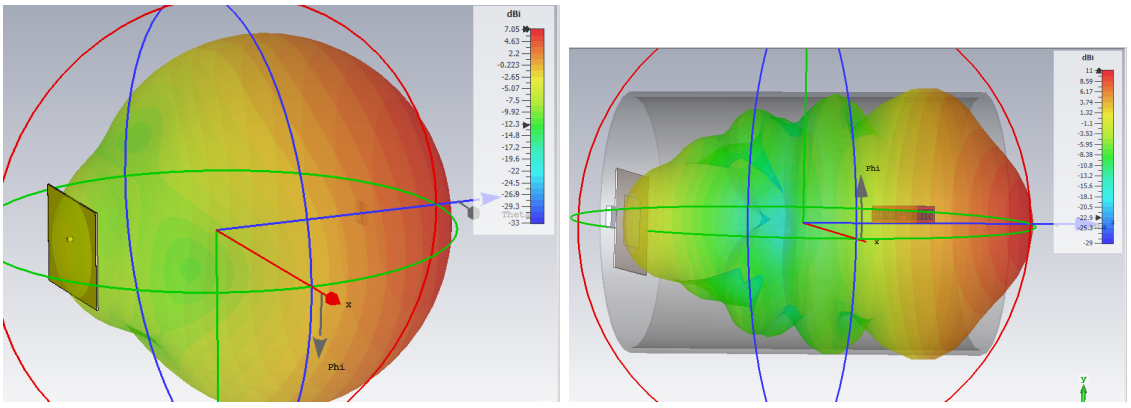

(a) RFID reader antenna far-field simulation in the open environment.

(b) RFID antenna far-field simulation inside the pipeline environment.

FIGURE 3.3: CST Studio RFID simulation results [4].

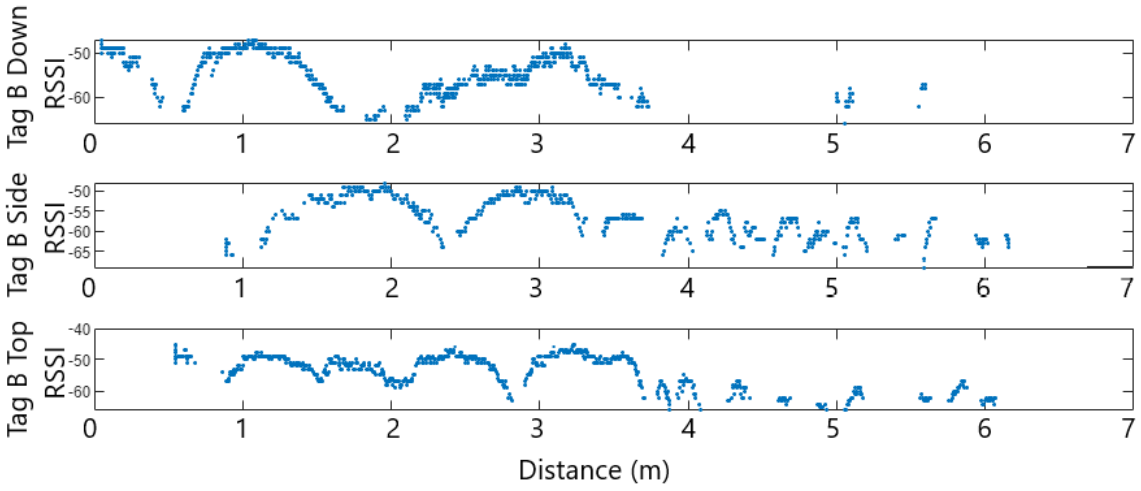


FIGURE 3.4: RFID tag location comparison [4].

paper-based substrate with a non-coiled antenna (Fig. 3.5a); oil-impregnated paper-based substrate with a coiled antenna (Fig. 3.5b); and strong metal-based substrate with a non-coiled antenna (Fig. 3.5c). Fig. 3.6 compares the results for the different tags (Fig. 3.5) tested to identify the most suitable tag for localisation. These tags were placed in the middle of the scanned length and the robot travelled from one end to the other. The results clearly show that inside the pipe, signals travel far and create a reflected ripple effect. Inside the pipe, the data are denser than those from the open space scan. Further, when the antenna passes the tags, the signal strength and data density diminishes. Tag A performed the best as its signal has low noise and produces a clear reflection pattern that will assist the localisation algorithms. Fig. 3.7 compares the RSSI and phase data for a

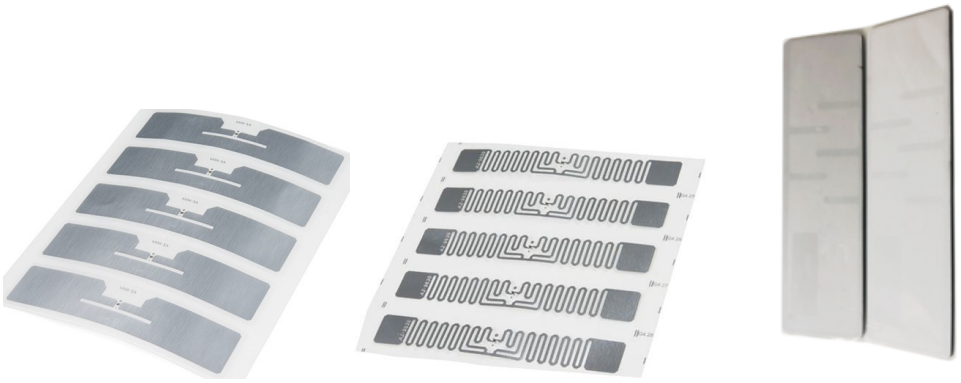

(a) Tag A. (b) Tag B. (c) Tag C.

FIGURE 3.5: RFID tags [4].

single tag. The RSSI data seem to have a more unique signal pattern than the phase data. Next, the same experiment was conducted in two different environments: inside the pipe and outside in the open, to compare the behaviour of the sensors. The tags were arranged inside a 6m long, 600 mm diameter, field-extracted water pipe sample as shown in Fig. 3.8 and data were collected using the robot. This experiment was repeated by changing the RFID tag location inside the pipe surface, at top, side, and bottom (Fig. 3.8d, 3.8c, 3.8b). The tests were then repeated by changing the distances ($d$) between RFID tags. Fig. 3.4 shows the data collected by placing RFID tags in different locations in the pipe. The three scans were done by placing a Tag A type in the middle of the pipe. The first scan shows the tag placed in the bottom section of the pipe; the next, at the side of the pipe; and the last, at the top crown of the pipe. The observations show that the top or side are the best locations to place RFID tags because the tag doesn't get covered from the robot when receiving data while traversing [138].

#### 3.3.2.3 UHF-RFID Sensor Signal Evaluation with Repeated Scans

An experiment was performed to determine the amount of signal deviation that would occur if the scans were repeated on the same configuration with minor changes in UHF-RFID sensor placement. Data were collected from five UHF-RFID sensors by spacing them 1 m apart inside the pipe sample on the side wall and operating the robot at a speed of 0.1 m/s, as shown in Fig. 3.9. Then, the UHF-RFID sensors were randomly positioned (within a 10-cm area from the initial position) and the robot was deployed a

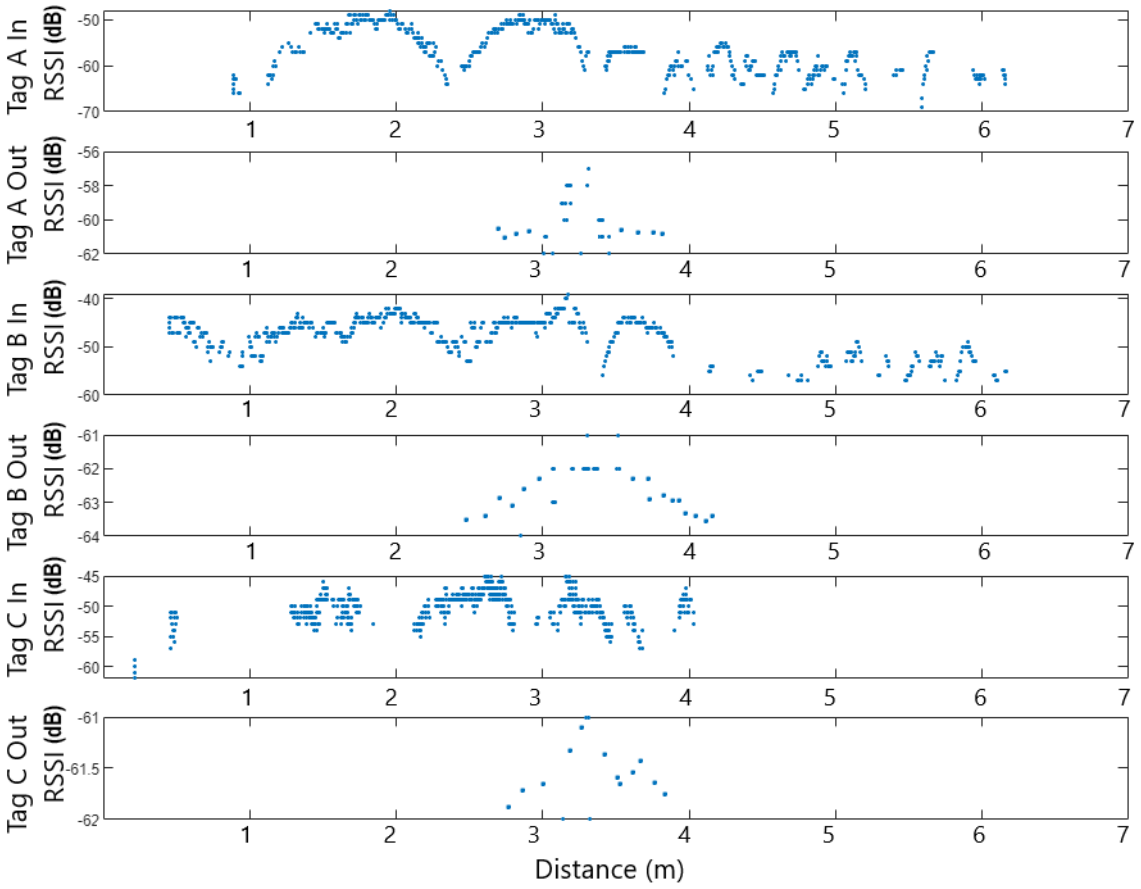


FIGURE 3.6: Comparison of RFID tags [4].

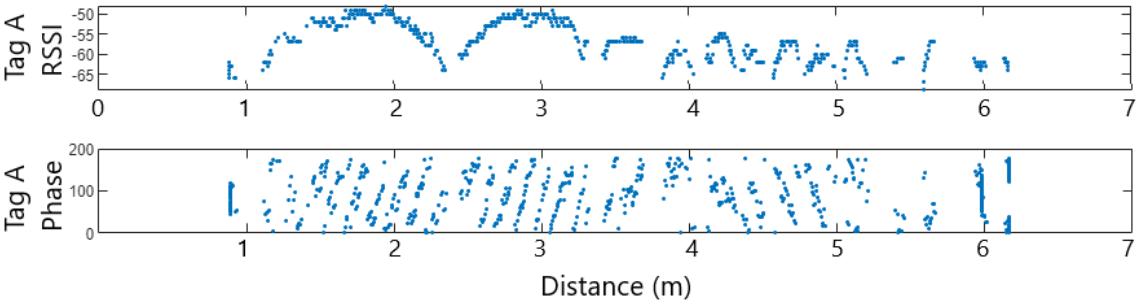


FIGURE 3.7: RFID tag RSSI and phase data [4].

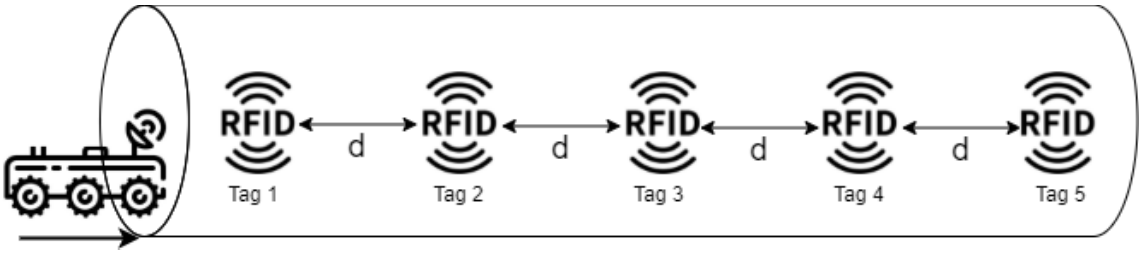


(a) RFID experimental setup inside the pipeline.

(b) RFID tags placed on the bottom of the pipe.

(c) RFID tags placed at the side of the pipe.

(d) RFID tags placed at the top of the pipe.

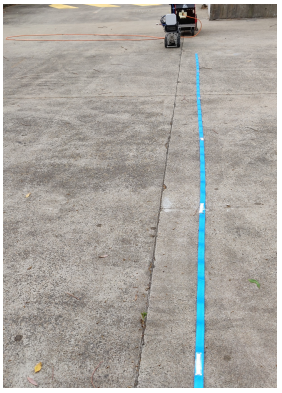

(e) RFID tags placed in an open area.

FIGURE 3.8: RFID test setups [4].

second time to collect data, as illustrated in Fig. 3.9, showing the round 2 data pattern. The data are interpolated up to a millimeter level to perform a detailed comparison. The results indicate that the two data patterns align very well. The degree of divergence in the results from two rounds of robotic scans was plotted on a histogram. As shown in Fig. 3.10, the majority of the data fit within the ± 2 dB mean signal variation with a correlation coefficient of 0.89. These experimental results provide confidence in the signal's repeatability, which will enhance localisation tasks. Further, these signal noises has been used as the White Gaussian Noise characteristics for proposed algorithms.

#### 3.3.2.4 Evaluating the Effects of UHF-RFID Signals with Different Hardware Configurations

The effect of the UHF-RFID sensor signal pattern was examined by changing the directional placement of the UHF-RFID reader antenna. The first scan was completed with the antenna facing forwards, and the second scan was completed with the same antenna facing backwards. Fig. 3.11 shows that the signal pattern changes as the

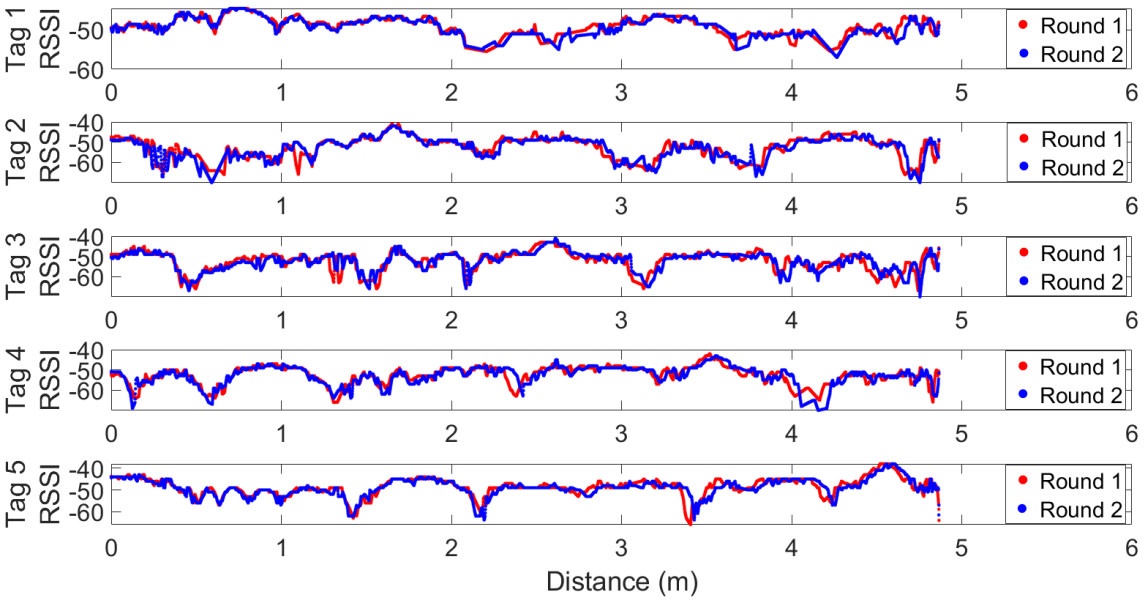


FIGURE 3.9: UHF-RFID sensor wireless signal comparison for two robotic scans [5].

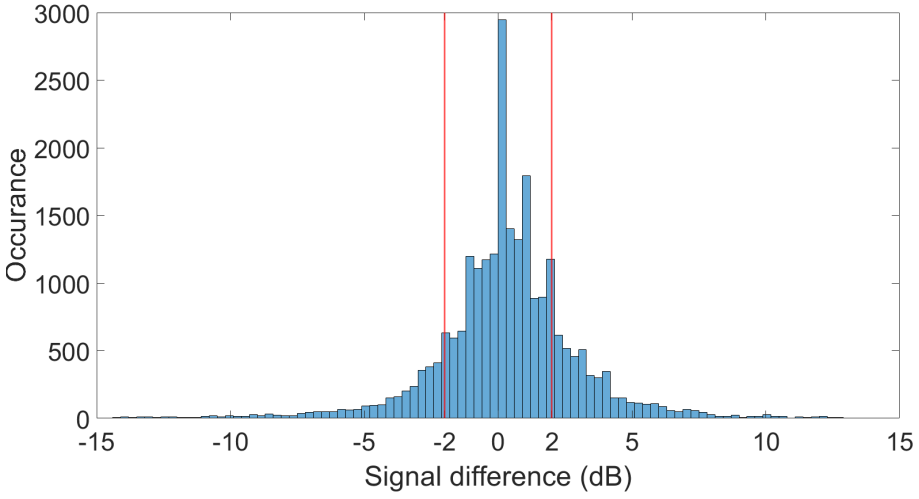


FIGURE 3.10: Histogram showing UHF-RFID sensor signal differences for each data point [5].

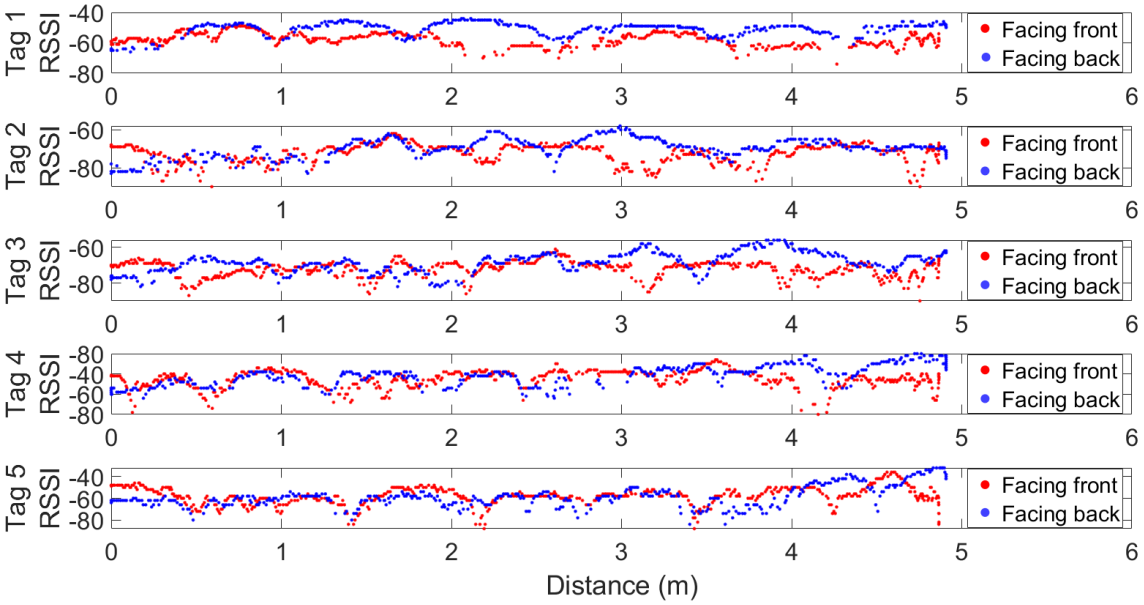


FIGURE 3.11: UHF-RFID sensor signal difference when the antenna faces the opposite direction [5].

antenna direction changes, with a correlation coefficient of 0.0468. Thus, once the training (initial) data set for robot localisation has been collected, the sensor model cannot be altered as this would render the collected data obsolete. A second experiment was conducted to determine the effect of the robot's movement on the signal. One scan was performed with the robot moving forwards and another with the robot moving backwards. The direction in which the UHF-RFID reader's antenna faced was not changed at any stage. The two scans were then aligned to enable visualisation of the signal difference, which is shown as the graph in Fig. 3.13, with a correlation coefficient of 0.91. It is clear that the direction of travel of the robot has no effect on the UHF-RFID sensor signal pattern. A third experiment was conducted to determine how the signal pattern behaved when the robot's speed was varied (0.1, 0.3, and 0.5 m/s). The results indicated that driving speed had no effect on the signal pattern, although it did influence the data frequency in that slower speed resulted in higher-resolution data (Fig. 3.12).

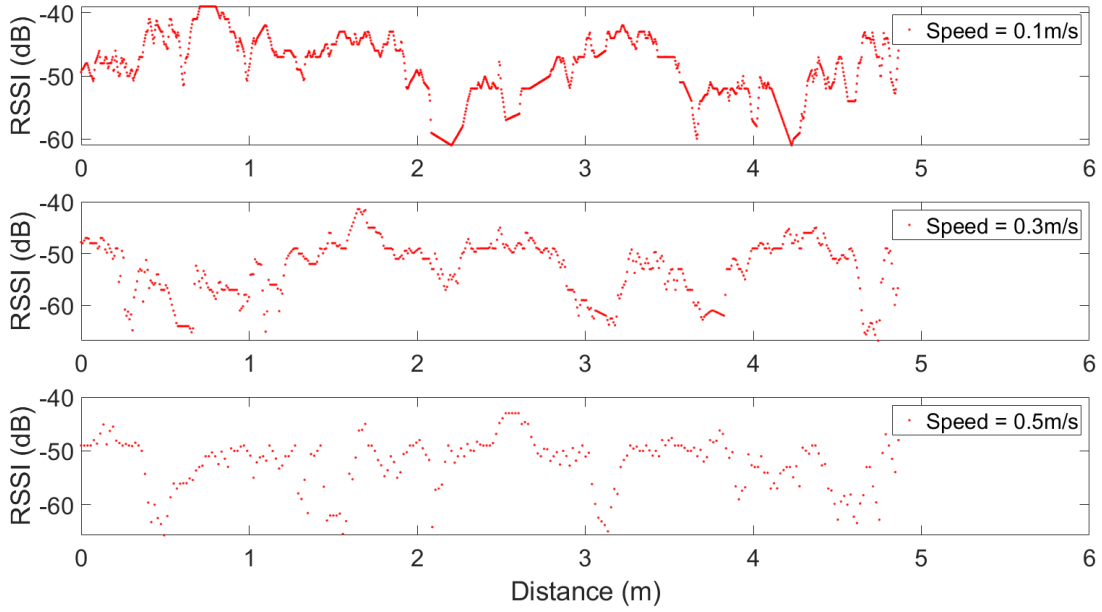


FIGURE 3.12: UHF-RFID sensor signal behaviour at different speeds of the robot.

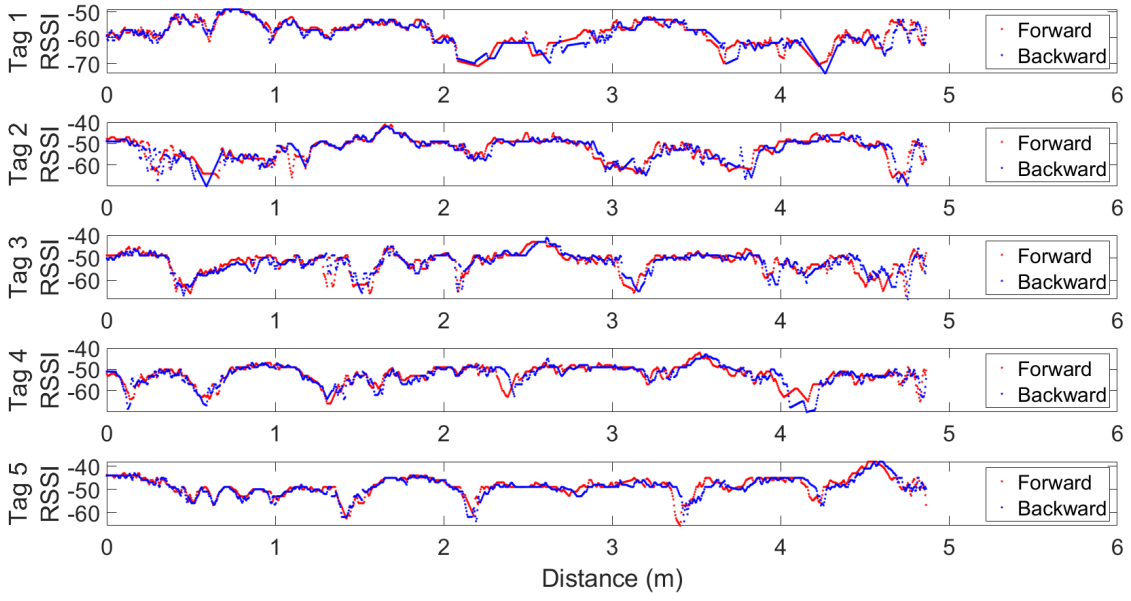


FIGURE 3.13: UHF-RFID sensor signal behaviour when robot moving in different directions.

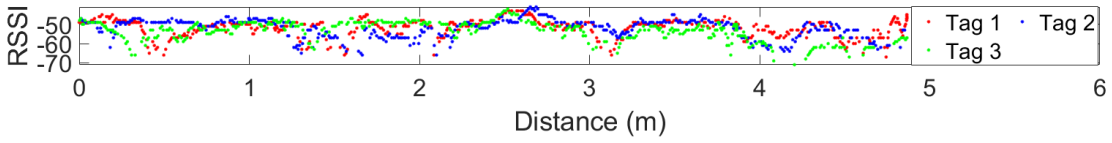


FIGURE 3.14: Wireless signal differences within the same family of UHF-RFID sensors [5].

#### 3.3.2.5 Evaluating the Signals of Same Type UHF-RFID Sensors

The purpose of this experiment was to determine the signal strength of various UHF-RFID sensors of the same model. Independent scans were performed for each sensor by placing them in the middle of the pipe and moving the robot from end to end. The signal difference between the three sensors of the same type is shown in Fig. 3.14, with a correlation coefficient of 0.64. Even though the sensors were of the same type, each sensor's signal appears to have a slightly different signal pattern when the antenna is not close (highest peak) to the sensor. The localisation task will be aided by having relatively distinctive signal signatures from each UHF-RFID sensor, as this will help to minimise the search area.

#### 3.3.2.6 Data Modelling

In-order to generate a more accurate measurement model the data capture during the training phase need to match with the pipe system (environment). This will increase the accuracy of the localisation and help in reducing the measurement noise. The collected data were mapped with the robot's odometry data to model the GP, which filters outliers and provides a stable data input for training the particle filter algorithm. Fig. 3.15 depicts the scan results for the 1 m apart tag distribution inside the water pipeline sample as shown in Fig. 3.8a, 3.8c. The red fitted curve represents the GP model, which normalises the raw data before they are used as the measurement model for the particle filter.

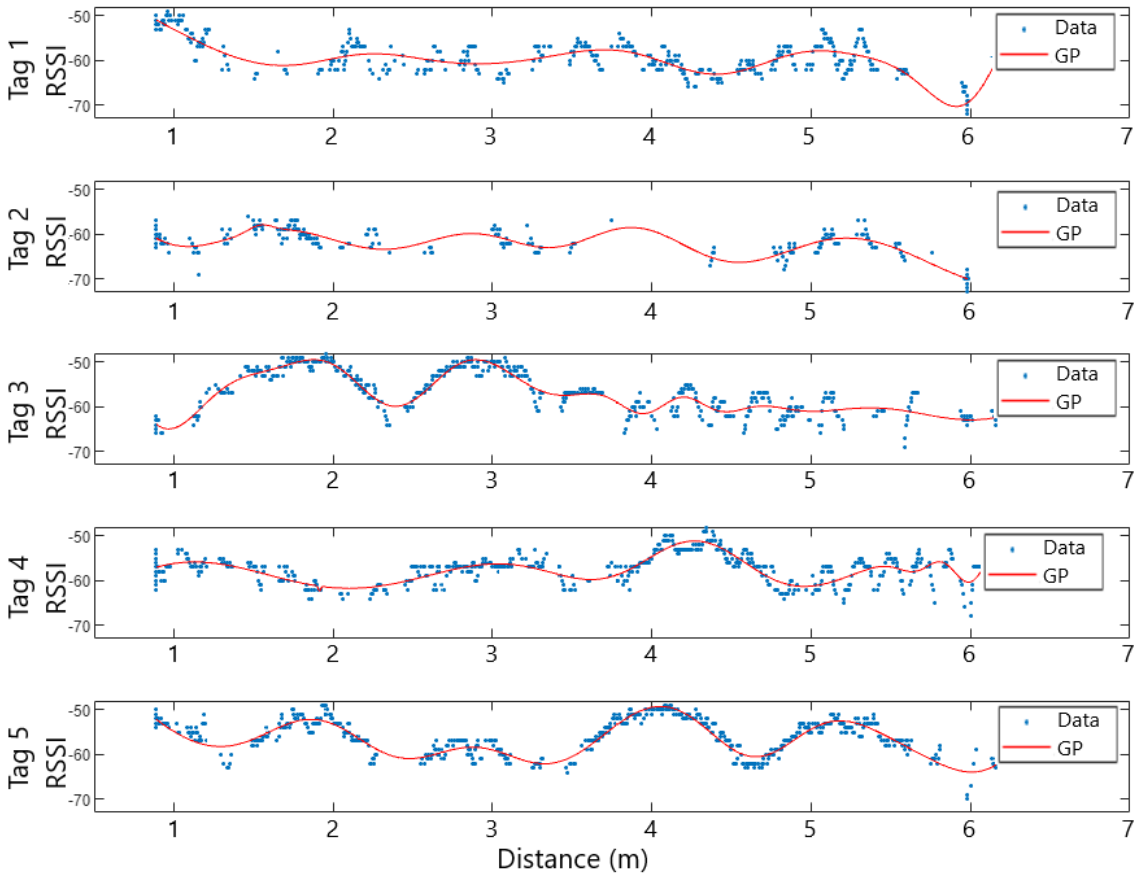


FIGURE 3.15: RFID GP data modelling [4].

#### 3.3.2.7 System Performance

Using these data models, the particle filter based localisation algorithm was tested in a ROS simulated environment to evaluate different data collections and particle filter configurations. The best results were achieved when the robot travelled at a maximum speed of 0.1 m/s, where the RFID reader detects tags at a maximum rate of 50 tag readings per second. The particle filter performance was evaluated with both a measurement model employing RSSI data alone, and a combined data model with RSSI and phase data. Fig. 3.16, 3.17 shows the performance evaluation of the particle filter for localisation prediction values. It is clear that there is a significant improvement in the localisation results when both RSSI and phase data are used in the particle filter measurement model. The proposed system achieved a precision of 15 cm accuracy in localisation results. A system performance video [139] has been published in [4]. Finally, particle filter performance was evaluated with different numbers of particle configurations, as shown in Fig. 3.18. The legend

indicates the number of particles for each performance data curve. The results show that maximum accuracy is captured with 300 particles. Increasing the number further (Fig. 3.18 p=400) reduces the performance of the system and increases the error rate, because the prediction algorithms takes too long to process and respond.

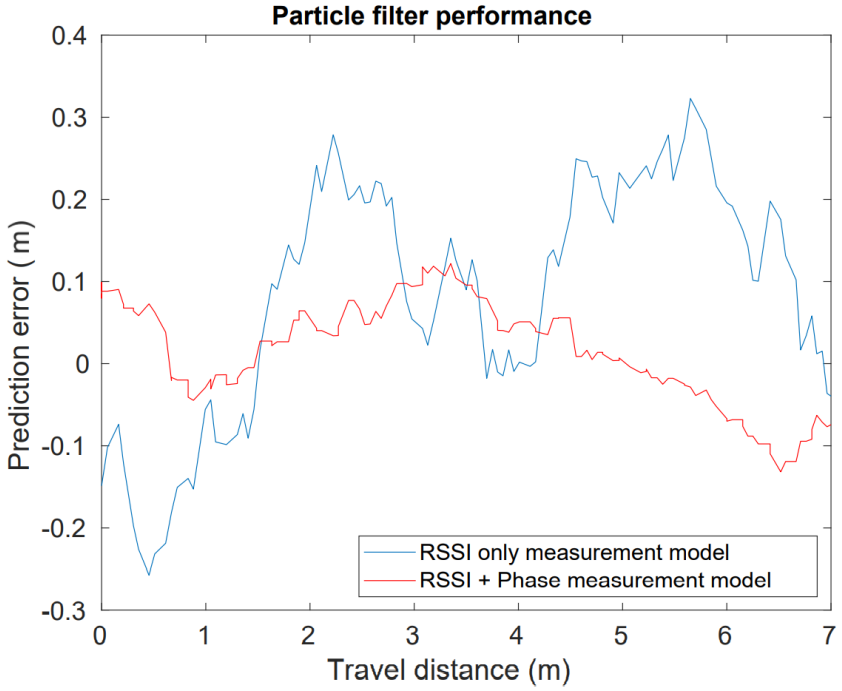


FIGURE 3.16: Particle filter performance evaluation with different measurement models [4].

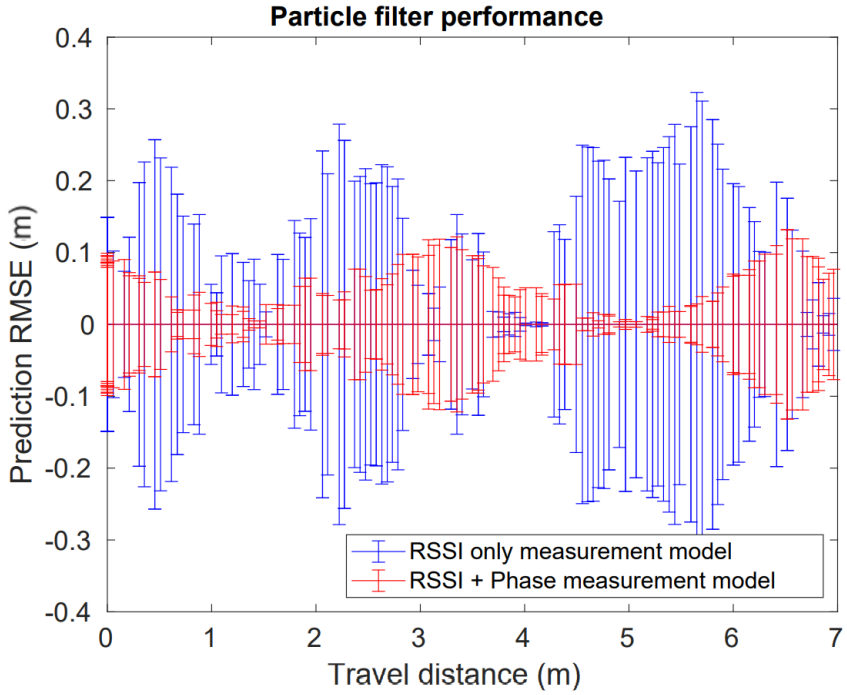


FIGURE 3.17: Error boundary representation of the particle filter performance evaluation with different measurement models [4].

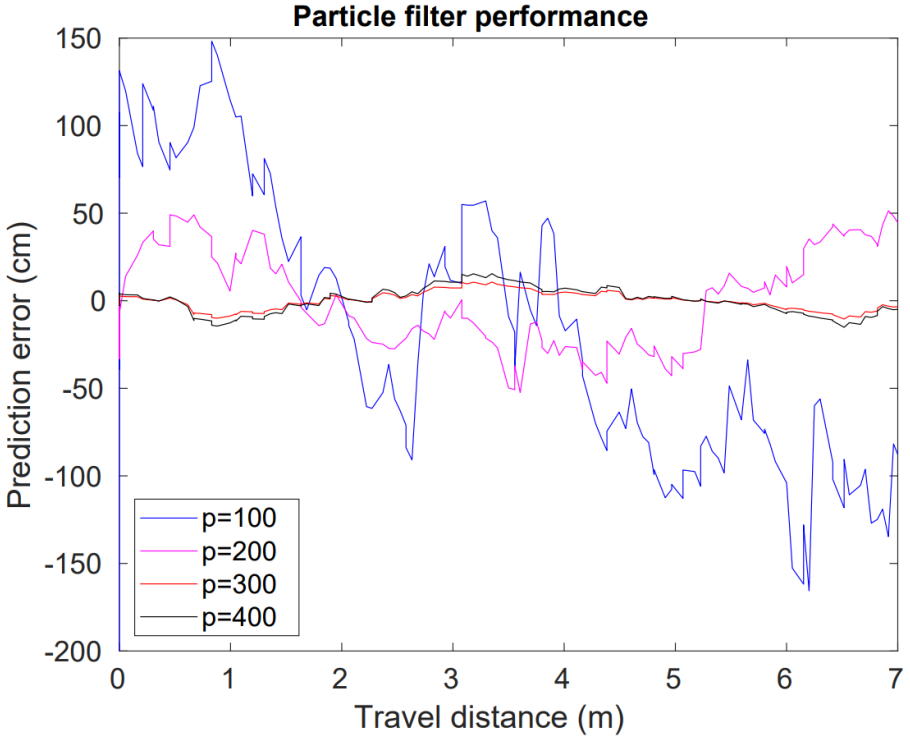


FIGURE 3.18: Particle filter performance evaluation against the number of particles [4].

### 3.3.3 Discussion

A single-antenna UHF-RFID signal-based robotic system for in-pipe localisation was presented in this section. The robotic localisation uses a particle filter combined with a GP algorithm. By incorporating both RSSI and phase shift values into the particle filter model, the localisation results are further enhanced. This scheme can be used for localisation without the aid of odometry after creating the initial measurement model. The system was validated in laboratory experiments by using a pipe sample extracted from the Sydney Water pipe network. The best type of RFID tag, location to deploy RFID tags, and their distribution inside the pipeline was identified, and the results showed that the proposed system has 15 cm accuracy. However, to achieve better results in laser profile measurements, 15 cm accuracy is not sufficient: millimetre-level accuracy is required to measure smaller scale defects accurately. Although the number of RFID tags deployed inside the pipeline can be increased to improve accuracy, a significant number of RFID tags is already deployed with 1 m separation, so deploying more is not practically feasible. Therefore, the following section explores different means of increasing the UHF-RFID's localisation accuracy.

## 3.4 Twin-UHF-RFID Antenna In-pipe Robot Localisation

In the search for improved localisation accuracy, the literature on outdoor and indoor environment localisation [140–144] motivated exploration of a twin-antenna UHF-RFID sensor model because particle filter accuracy improves with an increase in the number of measurements. The experiments conducted in this section indicated that unique signals measurements are generated from different antennas of the same model for a given RFID tag. Therefore, the existing methodology was modified to accommodate the twin-antenna UHF-RFID sensor model in terms of hardware, software, and measurement models for the particle filter algorithm discussed in Section 3.2 to explore the possibilities of improving the localisation accuracy.

### 3.4.1 Development of an In-pipe Robot System

#### 3.4.1.1 Hardware Development

The following modifications were made to the hardware model discussed in Section 3.3.1.1 to accommodate the twin-antenna UHF-RFID sensor module, as shown in Fig.3.19. Two 915 MHz General Purpose same model Panel RF antennas in the 902–928 MHz range with 5.5 dBi gain were used as the receiver antennas. An industry-standard IR laser distance sensor with 80 m range and 1 mm accuracy was used to collect the robot's ground truth odometry and prepare more accurate measurement model. To enable comparison of the performance with the standard wheel encoder-based odometry, a 2400 pulse-per-revolution rotary encoder was used to record the odometry.

#### 3.4.1.2 Software Development

The following modifications were made to the software architecture discussed in Section 3.3.1.2 to process the data efficiently and increase the accuracy of localisation, as shown in Fig. 3.20. A new laser distance sensor that tracks the ground truth odometry of the robot for preparing the measurement model was implemented as Arduino components. The odometry data from the wheel encoders were also recorded for later performance comparisons. The whole system implementation was improved with parallel thread handling for parallel data collection from the two antennas and processing in real time. The firmware of the RFID module was upgraded to receive 70 tag readings per second, to increase the data resolution and improve accuracy. In the training phase, the location mapper will combine the data with the robot's odometry data that it receives from the laser data publisher node. The Gaussian data modeler node will then filter and normalise the data and store them as measurement data maps for later use in the particle filter. In the localisation phase, the data received from the robot will be analysed in the RSSI & phase data balancer node that will distribute the weights according to the uncertainty values received from the pre-trained RSSI Gaussian process signal matching and the raw phase data signal matching. Finally, using these data, the particle filter algorithm will calculate the highest-probability robot location and publish

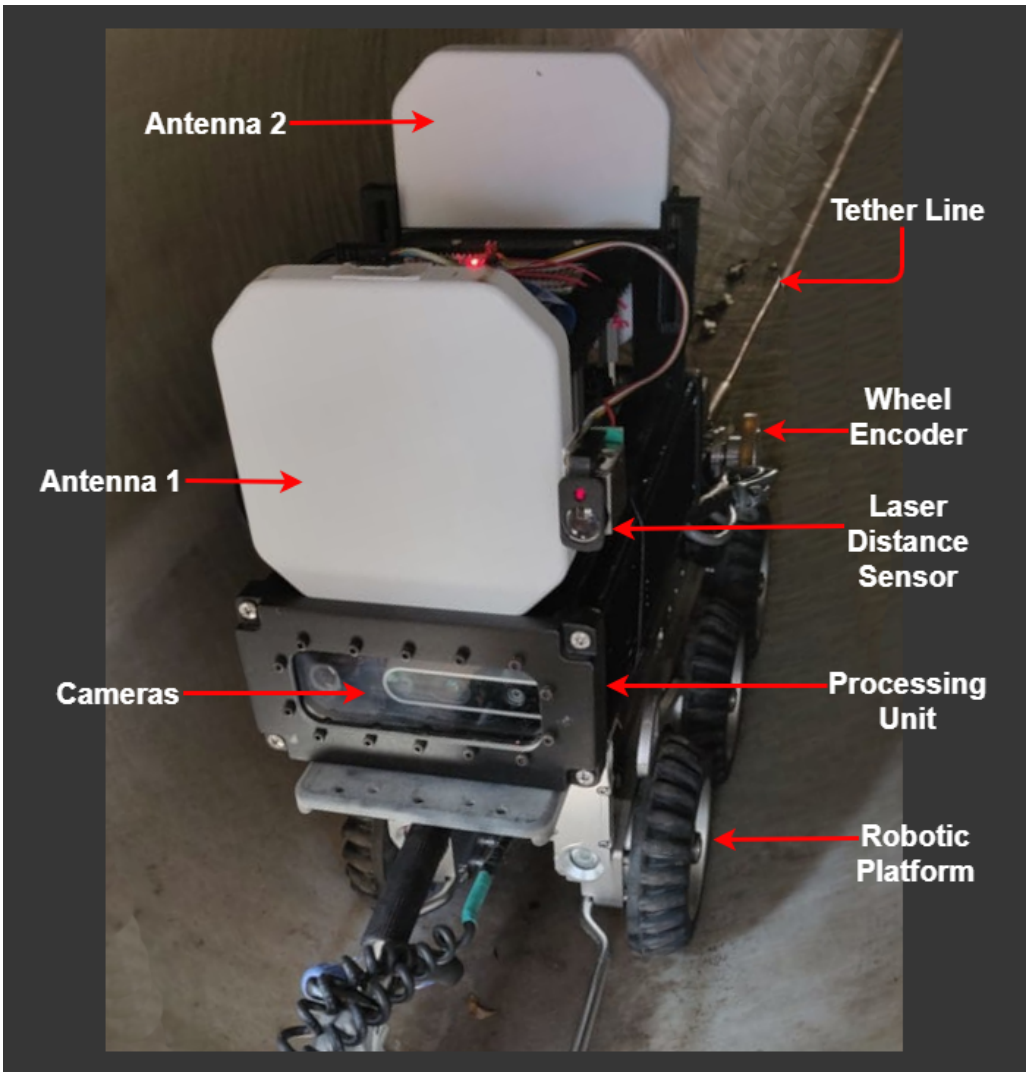


FIGURE 3.19: Robot with RFID unit mounted on top.

it to the localiser node, which will be displayed using RVIZ-like location visualisers through the location publisher node.

### 3.4.2 Robot Data Collection and Pre-processing for In-pipe Localisation

When integrating the second antenna into the model, the experiments showed that the two antennas produce different signal signatures for the same RFID tags in the same environment 3.22. This behaviour gave more confidence in using the two-antenna setup because it is known from the literature [4, 130] that having more RFID tags (more unique signals) improves the accuracy and having two unique signals from each RFID tag generates

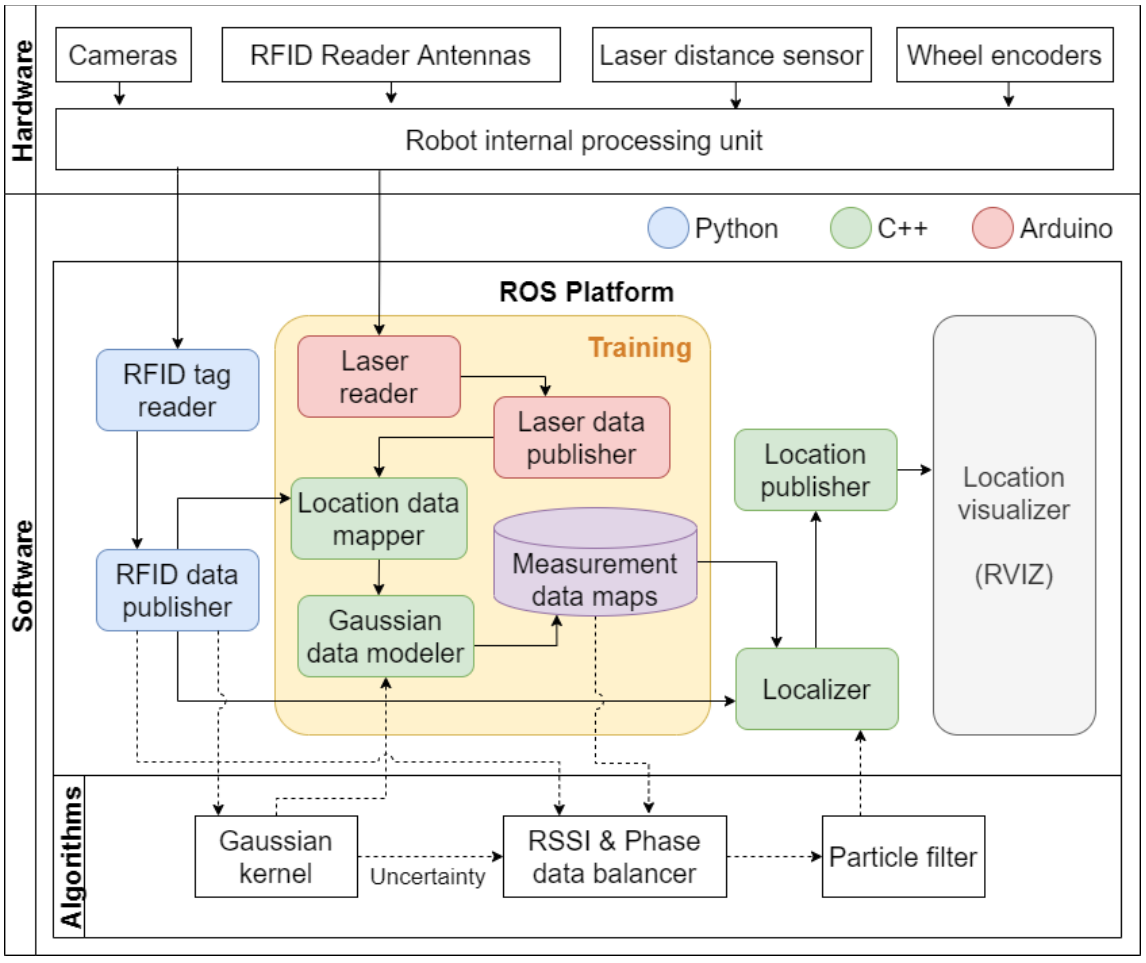


FIGURE 3.20: System architecture.

more signals without the need to increase the number of RFID tags, which will contribute to the accuracy of particle filter localisation.

The performance of the proposed model needed to be tested for a longer distance of around 50 m inside the pipeline. However, since the optimal deployment mechanism for RFID tags in underground pipelines is still in the research phase, the practical experiments were limited to collecting data from a 5 m pipe sample extracted from an underground Sydney Water pipeline. Therefore, to simulate 50 m of data the robot was deployed 10 times with unique RFID tags each time. These data were then aggregated into a single data model. This process was completed twice to generate the training and test data models.

### 3.4.3 Experiments and Results

This section presents the experiments and results evaluating the algorithm by varying each parameter that contributes to the final well-tuned performance and accuracy of the localisation.

#### 3.4.3.1 Robotic Data Collection and Processing

A 5 m long, 600 mm diameter extracted underground metallic pipe sample of Sydney Water was used to set up the laboratory test bed. RFID tags were deployed at equal spacing inside the pipe. Then the robot with the RFID unit was deployed in the pipeline from one end to the other as shown in Fig 3.21 collecting data from both antennas simultaneously. The laser distance reading from the robot was used as the ground truth data to prepare the measurement model.


FIGURE 3.21: Robot inside the pipe.

#### 3.4.3.2 The Signal Difference between the Two Antennas

The observations show that, having shared the same antenna model, the two UHF-RFID reader antennas produce significantly different signal patterns for the same UHF-RFID sensor. The literature in [145–149] mention few reasons to cause such incidents could be slight materialistic or electronic parts change/inconsistencies in manufacturing that affects the signal amplification. Hence, to determine the signal difference, two identical tests were conducted with the two UHF-RFID antennas. The experiments began with one antenna attached to the robot's front and scanning the pipe. A second test used the same setup

but with the second antenna attached to the robot's front and scanning the pipe. The signal difference between the identical UHF-RFID sensors placed in the pipe is shown in Fig. 3.22 with a correlation coefficient of 0.53. Obtaining distinct signal signatures from antennas for the same UHF-RFID sensor will significantly aid in localisation, as it can multiply the unique data measurements for a specific location as the number of antennas increases.

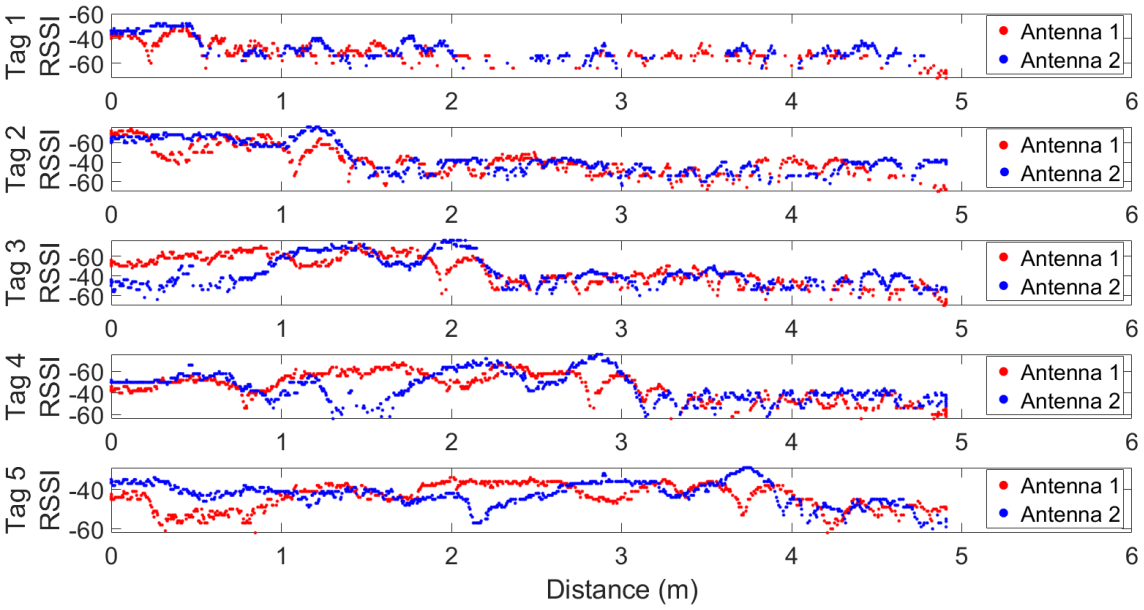


FIGURE 3.22: UHF-RFID sensor signal difference from two antennas of the same model [5].

As the literature indicates that signal interference between antennas may occur as a result of the hardware used to trigger both antennas simultaneously to receive signals [150], another test was conducted to determine if the current hardware exhibits any indication of such incidents. Data were collected from each antenna separately by running inside the pipe, and then from both antennas simultaneously. By comparing all these sets of data, resulting in a correlation coefficient of 0.92, it was determined that there is no significant effect on the signal when two antennas operate concurrently, with the hardware used here.

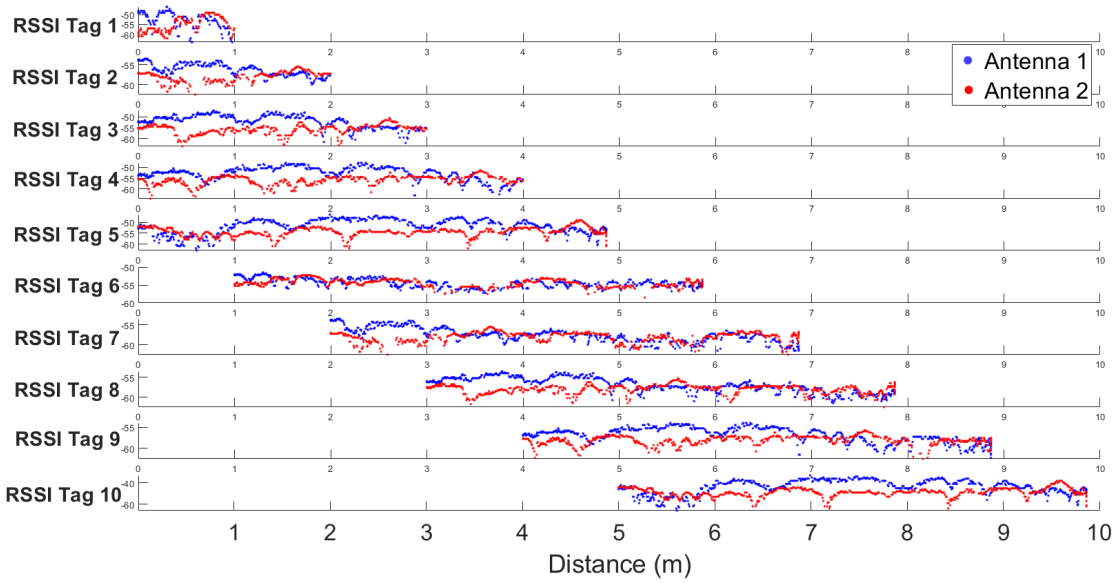


FIGURE 3.23: Training data sample.

#### 3.4.3.3 Test Data Preparation

During the Covid, access to a long pipe line to carry out the tests were not feasible. Therefore, it was decided to us the 5m pipeline to collect data from independent 10 runs to simulate a 50 m long pipeline. Fig 3.23 shows the concatenated 10 m section of data. This routine was repeated twice to create the training and testing data sets. At any given time, at least five RFID tags that could be uniquely identified by their EPC value were being detected from the sensor module. Next, for each RSSI signal generated from different RFID tags by a different antenna, a GP was trained to filter the outliers and normalise the data. Fig. 3.24 shows a section of training data from one antenna that contains the training data for six tags. The whole data set contains 100 individually trained GPs for 50 RFID tags received from two antennas in a 50 m long pipeline.

#### 3.4.3.4 Single vs. Double Antenna Comparison

Fig. 3.25 compares the localisation accuracy performance for the single and double antenna configurations. The double antenna configuration improves the accuracy up to 20 times more relative to the single antenna configuration. This is because when single

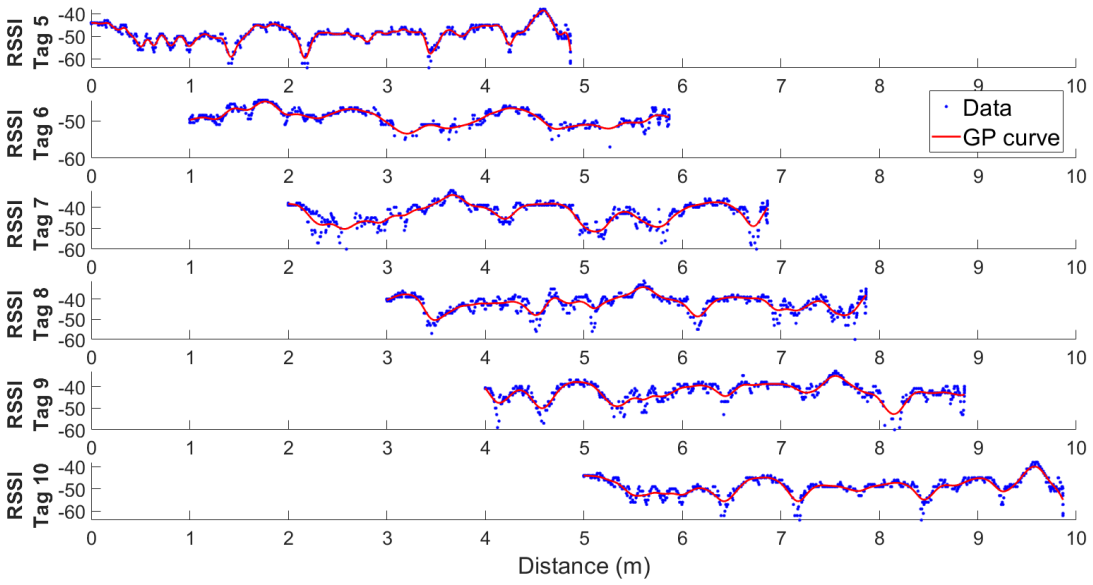


FIGURE 3.24: Example of GP training for RSSI signals received from a set of tags for one antenna.

antenna delivers two unique measurements for a particular robot location, the double antennas deliver four unique measurements (RSSI and phase data from each antenna) from each RFID tag to the particle filter algorithm, providing more information for accurate localisation.

#### 3.4.3.5 Effect of Phase Data on Localisation Result

As shown in Fig. 3.26, using phase data in combination with the RSSI data measurement model contributes to increasing the accuracy by 10 times over using the RSSI data measurement model alone. This is achieved by generating a measurement model for the particle filter by assigning high-priority weights to RSSI measurements and low-priority weights to phase measurements in Section 3.2.

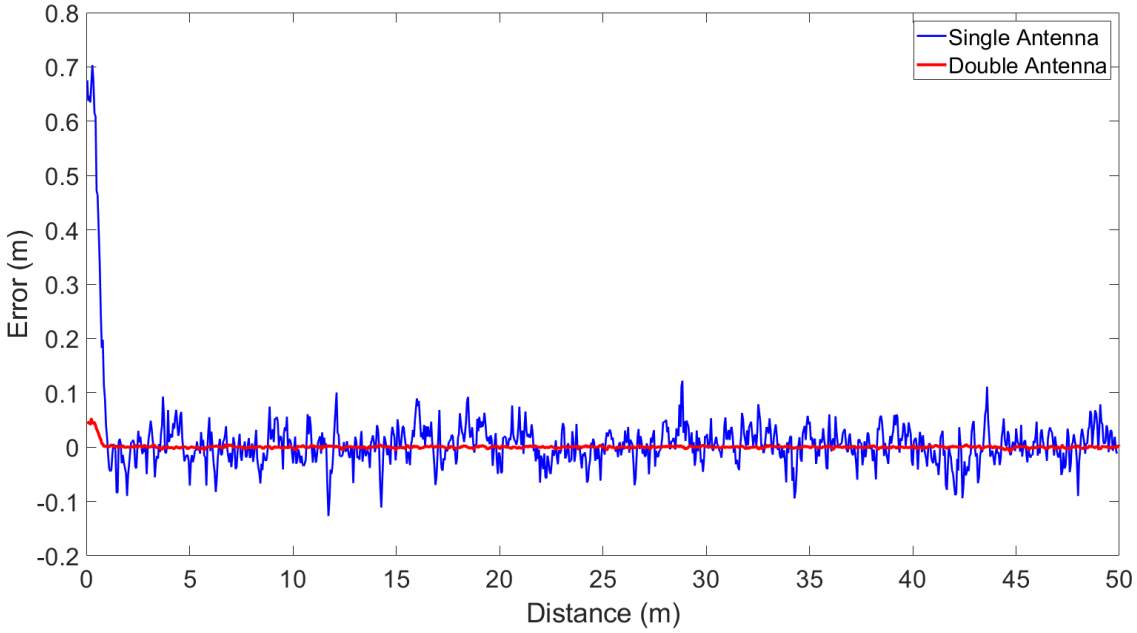


FIGURE 3.25: Single vs. double antenna performance.

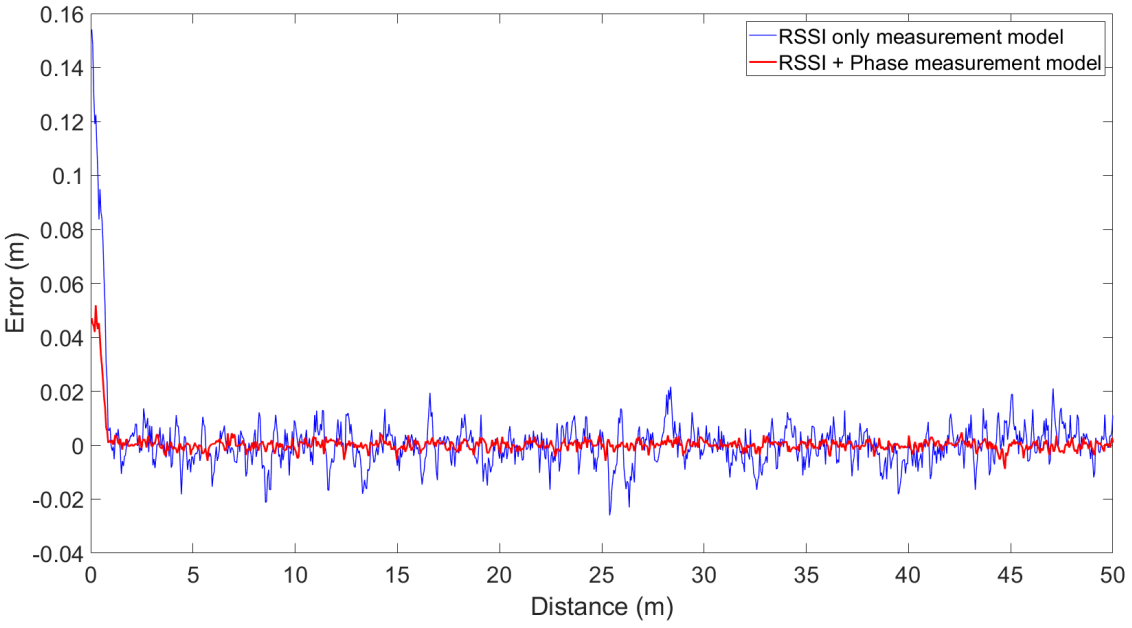


FIGURE 3.26: RSSI and phase data measurement model performance evaluation.

#### 3.4.3.6 RFID Tag Distribution Comparison

Performance comparisons were undertaken for different RFID tag distributions along the pipe. As seen in Fig. 3.27, when the distance between the RFID tags was reduced, the number of tags received to the antenna increases, improving the accuracy of localisation. As the objective is to achieve around 1 mm accuracy, the setup was finalised with 1 m tag distribution, which meets the project requirements and makes the solution more practical and economical.

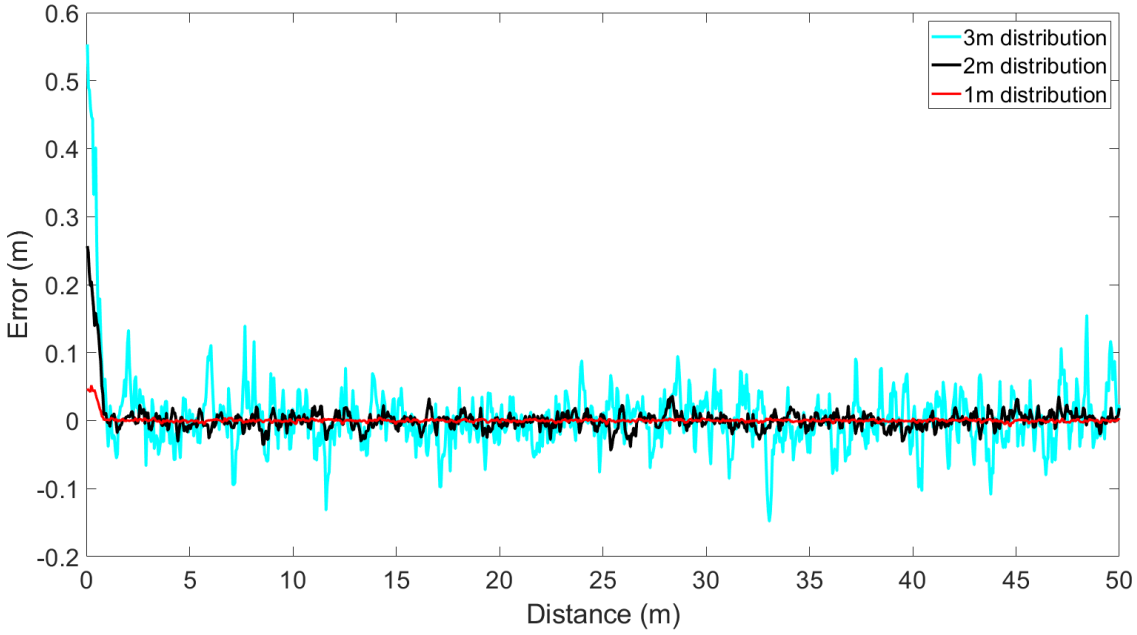


FIGURE 3.27: Tag distribution performance comparison.

#### 3.4.3.7 Number of Particles and Particle Spread Range Experiments

As seen in Fig. 3.28, increasing the particle numbers improves accuracy; however, the computational power installed in the robot is limited. Therefore, increasing the number of particles beyond 300 reduces the performance because of the delayed system response. Therefore, the optimal configuration is 300 particles for the hardware used in the prototype.

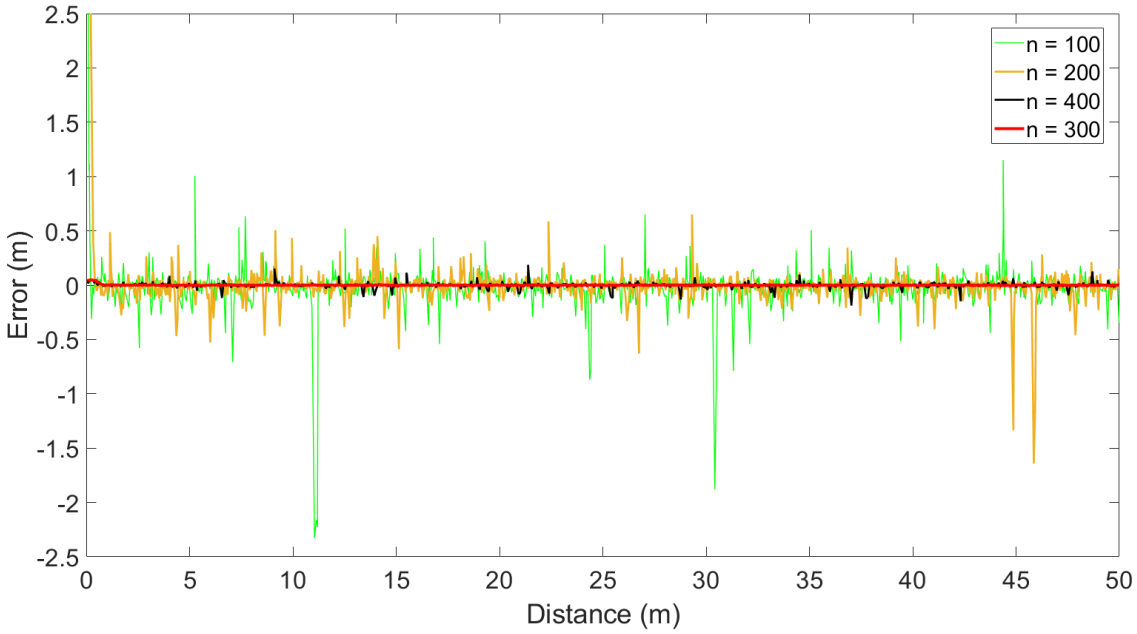


FIGURE 3.28: Performance comparison for different numbers of particles.

Fig. 3.29 shows the performance for different particle distributions. Spreading the particles over the whole pipe will reduce the accuracy because of the limited number of particles in a focused area of the pipe. As the starting location for the robot is known, reducing the particle distribution area around the starting location improves accuracy. However, reducing the distribution area too much will result in a longer time to recover from the error at the beginning, because the algorithm will find a local minimum optimisation point rather than locating the global minimum.

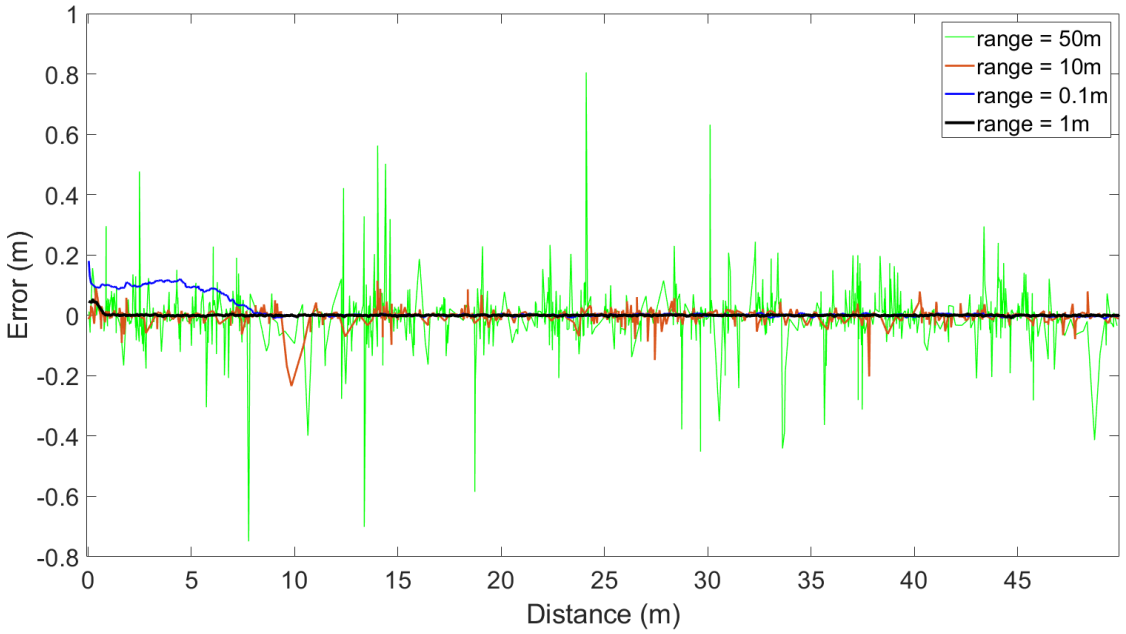


FIGURE 3.29: Particle distribution performance comparison.

#### 3.4.3.8 Performance Comparison with Standard Localisation Methods

Finally, using the optimal configuration parameters discussed above, accuracy of around 0.0018 m mean was achieved with 0.0016 standard deviation, as shown in Fig. 3.30. Fig. 3.31 shows the whiskers plot for 20 sets of trials performed with random noise. It is seen from the results that in some areas of the pipe, some RFID tags perform better reducing the uncertainty by providing less noisy measurements. It is due to several reasons including the quality of the RFID tag, the tag placement on the pipe, the pipe condition around the area of tag placement, and the robot's movement. Next, the localisation results were compared with the standard, well-known wheel encoder localisation method that is commonly used, as shown in Fig. 3.32. The accuracy of the encoder is sufficient for shorter distances because of negligible errors at the beginning, but for longer distances the error accumulates because of wheel slips. The RFID localisation accuracy is consistent along the pipe for longer distances, making it perfect for the required application. Further comparisons with the literature are presented in Chapter 4 Section 4.4.5.

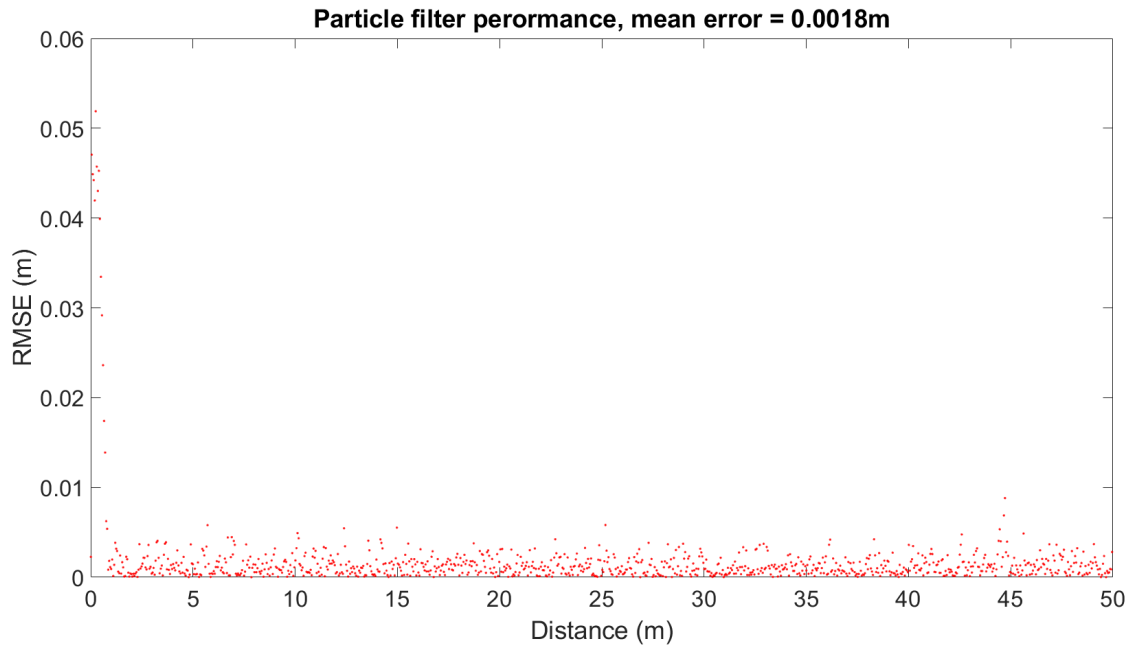


FIGURE 3.30: Particle filter performance. Mean error: 0.0018 m.

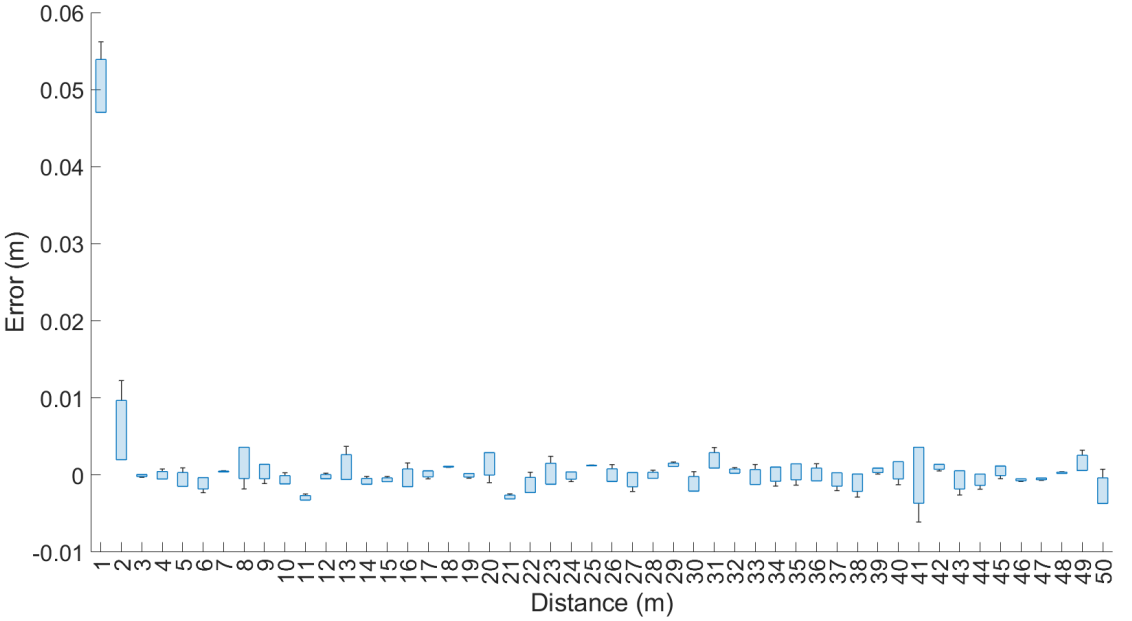


FIGURE 3.31: Whisker plot graph of 20 sets of trials with random noise.

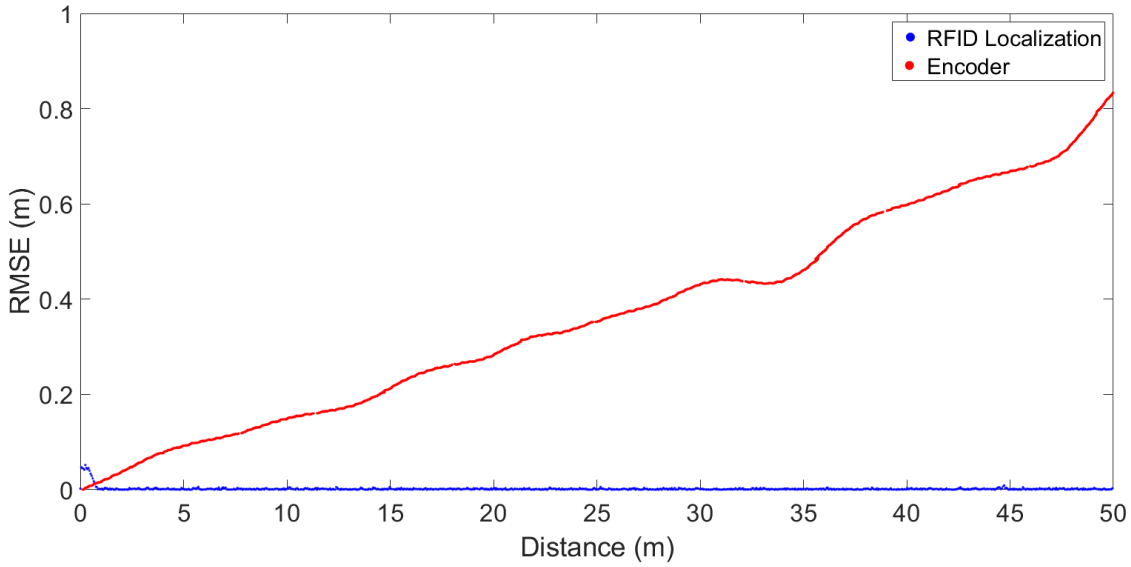


FIGURE 3.32: RFID vs. encoder.

Fig. 3.33 focuses the end of the 50 m long, three laser profile alignments of ground truth, encoder, and RFID localisation. As seen in the image, a mark on the top of the pipe crown was used to measure localisation alignment differences. It can be seen that the encoder-odometry-based laser profile is 0.817 m behind the ground truth laser profile. The RFID-localised laser profile has been perfectly aligned with the ground truth laser profile, giving 1 mm accuracy. Therefore, this system can be used to accurately align defects in laser profiles captured at different times, to monitor their evolution.

### 3.4.4 Discussion

The development of a robotic system that uses UHF-RFID signals to localise itself inside underground pipeline infrastructure was presented in this section. The system is equipped with a two-antenna sensor model and an improved measurement model. After the initial training phase, the scheme can be used for localisation without any support from the robot odometry system. The system has been validated via experiments carried out in a 50 m long simulated pipeline based on field-extracted pipe samples from the Sydney Water pipe network. Further, the optimal configuration parameters in terms of the algorithm and hardware configurations to achieve the best results were presented. The results showed that

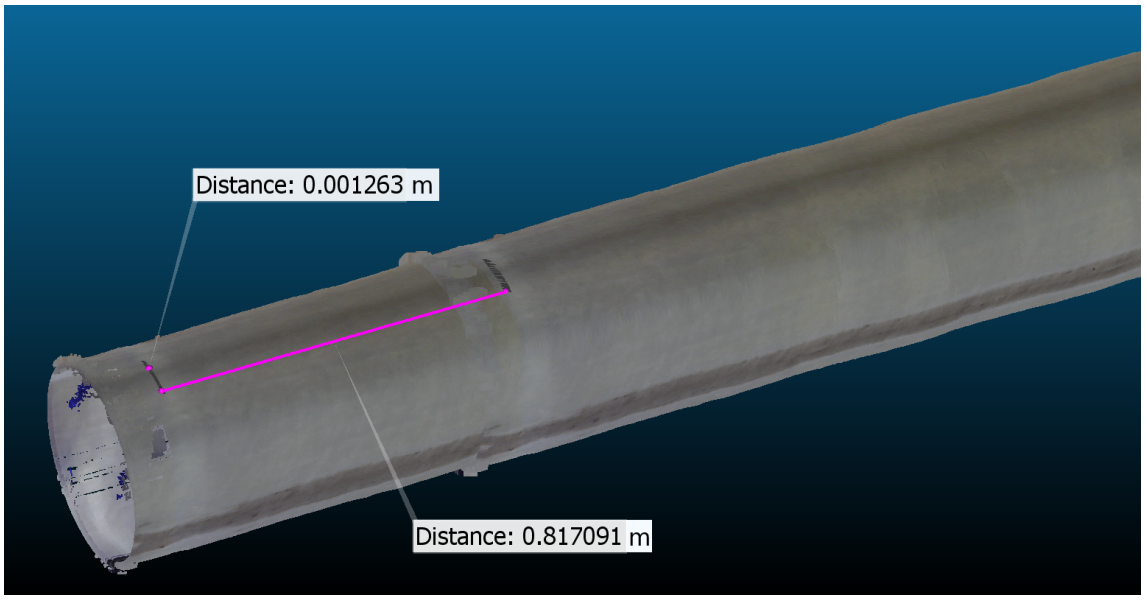


FIGURE 3.33: Laser profile localisation evaluation: RFID vs. encoder.

the proposed system is capable of localising the robot inside the pipeline with millimetre-level accuracy that is consistent along the pipe over long distances. The system was further evaluated by comparison with standard commonly used encoder-based localisation systems. To compare the encoder and RFID localisation results, an industry-standard IR laser distance sensor with 80 m range and 1 mm accuracy was used to produce the ground truth measurements. The results showed that the system performs substantially better than current standard wheel or tether line encoder-based localisation methods.

## 3.5 Summary

In this chapter, design and development of a UHF-RFID signal based robotic system for localisation inside pipelines has been presented. The robotic localisation uses a particle filter combined with a GP algorithm. Localisation accuracy is enhanced by integrating both RSSI and phase signals into the measurement model. The initial experiments were done with a single-antenna hardware model, which produced an approximate accuracy of 15 cm. To improve accuracy, a two-antenna sensor model with improved localisation algorithms was integrated. The system was validated in a 5 m long field-extracted pipe section from the Sydney Water network, simulating 50 m long pipe. The results

indicated that the system delivers millimetre-level accuracy. The proposed system was compared with commonly used standard encoder-based localisation systems, which showed that RFID localisation performs significantly better than encoders over longer distances. Finally, the system was evaluated using laser profile alignments for feature mapping. The results showed that the system is capable of aligning 50 m long laser profile scans with up to millimetre-level accuracy.

Because of COVID-19 pandemic restrictions, it has not been possible to test the localisation system in real underground pipe networks. Such performance evaluation work is planned for the future and will involve laser profiling to monitor defect evolution by aligning profiles taken at different times. The accuracy of the current system depends strongly on the accuracy of locations of the RFID tags deployed inside the pipeline. However, in most cases, the practical deployment of RFID tags inside the pipeline requires use of a robotic platform, which involves conventional erroneous localisation systems. Hence, the locations of tags deployed using a robot cannot be precisely known. Therefore, in the next chapter an improved system is discussed that can localise the robot accurately when the RFID tag locations are not exactly known.

The following publications are outcomes of the work presented in this chapter:

1. **A. Gunatilake**, K. Thiyagarajan, S. Kodagoda, "A Novel UHF-RFID Dual Antenna Signals Combined with Gaussian Process and Particle Filter for In-pipe Robot Localization," IEEE Robotics and Automation Letters. *(Accepted for publication.)*

2. **A. Gunatilake**, M. Galea, K. Thiyagarajan, S. Kodagoda, L. Piyathilaka, and P. Darji, "Using uhf-rfid signals for robot localization inside pipelines," in 2021 16$^{\text{th}}$ IEEE Conference on Industrial Electronics and Applications (ICIEA), 2021, pp. 1109-1114, doi: 10.1109/ICIEA51954.2021.9516284.

3. **A. Gunatilake**, K. Thiyagarajan, S. Kodagoda, "Evaluation of Battery-free UHF-RFID Sensor Wireless Signals for In-pipe Robotic Applications," IEEE Sensors Conference, 2021, pp. 1-4, doi: 10.1109/SENSORS47087.2021.9639827.

# Chapter 4

# RFID Based In-pipe SLAM

## 4.1 Introduction

This chapter discusses ways to overcome the shortcomings discussed in the Chapter 3 summary related to robot localisation in an unknown RFID deployment inside pipelines. To use the localisation method proposed in Chapter 3, RFID tags initially needed to be deployed inside the pipeline at accurately known locations. However, when deploying RFID tags inside pipelines a robot relies on conventional localisation methods, which are known to be error prone at longer distances [8, 140, 151, 152]. Most of the commonly used wheel or tether line encoder-based odometry systems become inaccurate over increasing distances because the accumulation of errors created along the travel distance make deployed RFID tag locations uncertain [26]. Hence, a system is required that is capable of simultaneously localising the robot and mapping the RFID locations accurately.

Many systems are currently available that can simultaneously localise a robot and map features in outdoor and indoor environments via visual odometry [153–158]. However, there are very few, localisation methods available for visual SLAM inside pipelines and they are poor in accuracy. Several studies have used stereo cameras [86], RGB-D sensors [90] and monocular cameras [88, 91] with machine learning algorithms to localise robots inside pipelines with limited accracy. Others have demonstrated SLAM localisation approaches

with the camera facing the pipe wall [159] and detecting surface changes in the wall while traversing along the pipe axis [160]; by detecting pipe joints or corners [161]; or by projecting structured light patterns on the wall [162, 163] using laser beam [164] or laser ring projections [165] to detect 3D surface feature changes using ToF images [166]. These approaches are obsolete for our purposes because of their limited accuracy and the limited number of perceptible visual features after liner application, which hides pre-existing features on a pipe's internal surface, making the surface smooth and even over most of its area.

Alternatively, some studies have proposed using ultrasound sensors and acoustic sensors for localisation [92, 167] inside pipes by measuring sound-induced vibrations or the latency of sound wave arrival from a fixed source [94, 112, 168]. Although these techniques work well for plastic pipes, they may not work well for underground metallic water pipes of different sizes and under different environmental conditions. Further, in situations where pipes are in the operational state, sound reflections and absorption by different water levels will produce inaccurate localisation results. Some studies have used additional sensors to support the accuracy of localisation results with IMU sensors and leak sensors by detecting junctions [169–172] with sensing variations in tilt, orientation changes and water leaks [173–176]. However, the metallic environment inside water pipes can interfere with a magnetometer [26, 177] and the slippery surface of the pipe may cause drift in the robot's location [173, 178], leading to misinformation in the accelerometer and introducing errors in the localisation. Further detection of water leaks using sensors for localisation is not an option since the objective is to prevent such incidents beforehand.

Since UHF-RFID signals are already in use for robot localisation [112], and potentially overcome the limitations of current localisation methods, the current research focused on discovering a better and more efficient robot localisation method that can simultaneously map RFID tag locations accurately.

This chapter proposes a battery-free RFID sensor localisation system that uses a RSSI signal-based customised SLAM algorithm to localise the robot and estimate RFID tag locations (Fig. 4.1).

The key contributions of this chapter are:

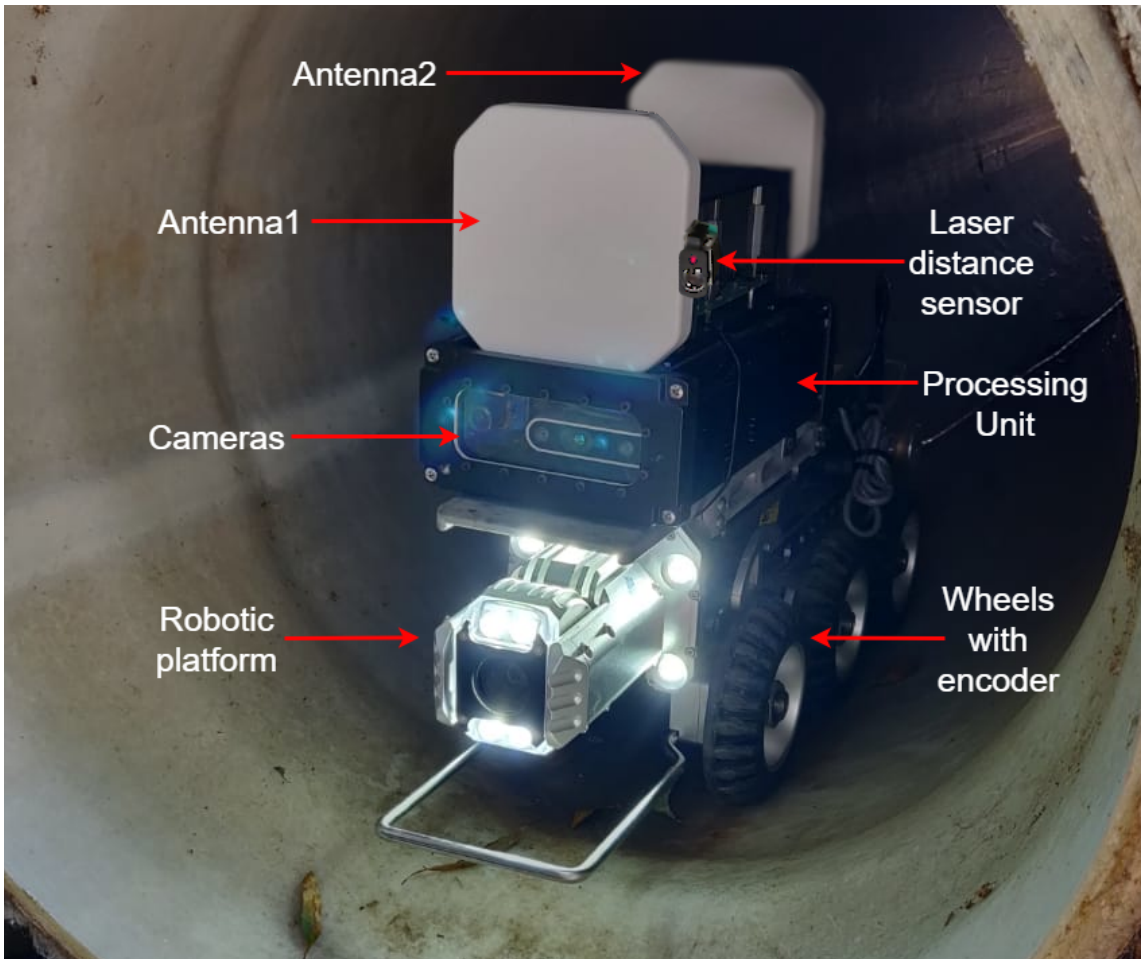


FIGURE 4.1: Crawler robot with the RFID unit fixed on top.

- A robotic simultaneous localisation and mapping with a custom measurement model using twin-antenna UHF-RFID signal cross-correlation is formulated.
- The system can be deployed from any location within the pipe and can travel in any direction while localising the robot with approximately 2.5-cm accuracy and mapping RFID tag locations inside the pipeline, where RFID locations are not exactly known.
- The system works independently without the aid of any other odometry system and requires only a training data set acquired in a laboratory pipe sample. It does not require any field calibration to perform at the site.

The rest of this chapter is structured as follows. Section 4.2 describes the methodology by formulating the algorithms. Section 4.3 describes the hardware and software architecture.

The experimental results are presented and discussed in Section 4.4. Finally, Section 4.5 concludes the chapter by summarising the key outcomes and briefly outlines intended future work.

## 4.2 Problem Formulation

Experiments presented in Chapter 3 showed that UHF-RFID sensor signals behave differently inside metallic pipe environments compared to open environments where the signal bounces off the pipe surface and creates multiple peak points. This presents a challenge for predicting the sensor location inside the pipeline, unlike with outdoor RFID SLAM where the RFID sensor creates only one peak point when the antenna is closest to it. However, this specific signal behaviour might be an advantage for formulating a SLAM algorithm to localise the robot and sensors inside the pipeline. Since each RFID sensor from each antenna gives a unique signal pattern, it can be used in a SLAM measurement model with signal cross-correlation mapping [85].

Most scans are done in a straight line from one manhole to the next, covering around 100 m of pipe length at a time. Therefore, unlike outdoor SLAM where there are too many parameters to predict, inside the pipeline robot localisation is mostly a One-dimensional (1D) SLAM problem along the pipe axis because the pipes are narrow and straight. Slight orientation changes are already detected using the solution proposed in Chapter 1.

Most SLAM approaches, such as Extended Kalman Filter (EKF)-SLAM, Fast-SLAM and ORB-SLAM, only estimate the robot's current location [179–181]. However, in this research, the complete trajectory of the robot needs to be estimated along with the RFID sensor locations. Therefore, pose-graph optimisation was chosen [182–186] which is further known to provide consistency, better accuracy and able to effectively process large number of data mapping [187].

### 4.2.1 Robot Localisation and Mapping

Conventional pose-graph optimisation problem solving [188–190] has been used to localise robots inside pipelines with respect to the RFID measurements received from sensor models. The motion model for a robot's movement along a pipe can be defined as in Equation (4.1):

$$x_t^r = g\left(u_t, x_{t-1}^r\right) + \omega_t \tag{4.1}$$

where $x_t^r$ is the 1D position of the robot along the axis of the pipeline at time $t$; $u_t$ is the input given to the robot at time $t$; $g$ is a non-linear function for state transitions; and $\omega_t$ is White Gaussian Noise where $\omega_t \sim N(0, R_t)$.

Thus, the RFID (landmark) measurement model for the robot can be defined as in Equation (4.2):

$$z_t^i = h\left(x_t^r, x^i\right) + \upsilon_t \tag{4.2}$$

where $z_t^i$ is the RFID measurement from the RFID landmark $i$ at time $t$; $x^i$ is the position of an RFID item $i$; $h$ is a non-linear function for measurement; and $\upsilon_t$ is White Gaussian Noise for measurement where $\upsilon_t \sim N(0, Q_t)$. The robot only senses RFID tags that are nearby. Therefore for some time indices $t$, there can be no measurements.

The conventional pose-graph optimisation problem [188] cost function can be defined as in Equation (4.3):

$$\begin{aligned} J &= x_0^{rT} \Omega_0 x_0 \\ &+ \sum_t^T \left(x_t^r - g\left(u_t, x_{t-1}^r\right)\right)^T R_t^{-1} \left(x_t^r - g\left(u_t, x_{t-1}^r\right)\right) \\ &+ \sum_t^T \sum_i^I \left(z_t^i - h\left(x_t^r, x^i\right)\right)^T Q_t^{-1} \left(z_t^i - h\left(x_t^r, x^i\right)\right) \end{aligned} \tag{4.3}$$

where $x_0$ is the initial state of the robot with uncertainty $\Omega_0^{-1}$; $R_t^{-1}$ is the covariance of motion noise; $Q_t^{-1}$ is the covariance of measurement noise; $T$ is the number of time steps for the robot; and $I$ is the number of features. The problem defined in Equation 4.3 can

be solved as an optimisation problem using Equation (4.4),

$$\mathbf{x}^* = \underset{\mathbf{x}}{argmin}\ J(\mathbf{x}) \tag{4.4}$$

where $\mathbf{x}$ is given as:

$$\mathbf{x} = \begin{bmatrix} \mathbf{x}^r_{0:T} \\ \mathbf{x}^{0:I} \end{bmatrix} \tag{4.5}$$

Using numerical methods this optimisation problem is solved iteratively to compute the gradient.

### 4.2.2 Pose Graph Optimisation with RFID Signal Mapping

The robot trajectory path and RFID (landmark) location estimations need to be simultaneously optimised. Therefore, RFID RSSI signal measurements need to be incorporated into the optimisation problem. This is achieved by incorporating the RSSI signal $s_t$ into the pose-graph optimisation problem in Equation (4.3) with an additional cost function $\phi$ that denotes the inconsistency of signal measurement along the pipe traverse. The updated equation is defined by Equation (4.6):

$$\begin{aligned} J &= x_0^{rT} \Omega_0 x_0 \\ &+ \sum_t^T \left(x_t^r - g\left(u_t, x_{t-1}^r\right)\right)^T R_t^{-1} \left(x_t^r - g\left(u_t, x_{t-1}^r\right)\right) \\ &+ \sum_t^T \sum_i^I \left(z_t^i - h\left(x_t^r, x^i\right)\right)^T Q_t^{-1} \left(z_t^i - h\left(x_t^r, x^i\right)\right) \\ &+ \sum_t^T \phi\left(t, \mathbf{x}^r_{0:T}, \mathbf{s}_{0:T}\right)^T P_t^{-1} \phi\left(t, \mathbf{x}^r_{0:T}, \mathbf{s}_{0:T}\right) \end{aligned} \tag{4.6}$$

where $\mathbf{x}^r_{0:T}$ are the robot positions along the pipe; $\mathbf{s}_{0:T}$ are the RFID signal measurements along the pipe; and $P_t$ is the covariance of the measurement model noise.

Function $\phi$ can be defined as in Equation (4.7):

$$\phi\left(t, \mathbf{x}^r_{0:T}, \mathbf{s}_{0:T}\right) = y\left(t, \mathbf{x}^r_{0:T}, \mathbf{s}_{0:T}\right) - f\left(t, \mathbf{x}^r_{0:T}, \mathbf{s}_{0:T}\right) \tag{4.7}$$

where $y$ is a function that calculates the distance between matching points of the signal $\mathbf{s}$, and $f$ is a function that calculates the distance between matching points in the estimations of $\mathbf{x}$.

### 4.2.3 RSSI Signal Cross-Correlation Matching

Let $\left[\mathbf{x}_{p1}^{r}, \mathbf{s}_{p1}\right]$ be the training data collected from the robot in the initial stage of the laboratory pipe environment, and $\left[\mathbf{x}_{p2}^{r}, \mathbf{s}_{p2}\right]$ be the data received from the robot during the localisation task. Before performing cross-correlation, an equal number of comparison data points are generated with data interpolation. Let the new sets of points be $\left[\mathbf{x}_{q1}^{r}, \mathbf{s}_{q1}\right]$, $\left[\mathbf{x}_{q2}^{r}, and \mathbf{s}_{q2}\right]$, where $[\mathbf{x}_{1}^{r}, \mathbf{s}_{1}]$, $[\mathbf{x}_{2}^{r}, and \mathbf{s}_{2}]$ be the subsets of points. the normalised cross-correlation coefficient $\gamma$ between the two sets of data can be calculated for each window using Equation (4.8):

$$\gamma = \frac{\sum_x \left(\mathbf{s}_1(x) - \overline{s_1}\right)\left(\mathbf{s}_2(x) - \overline{s_2}\right)}{\sqrt{\sum_x \left(\mathbf{s}_1(x) - \overline{s_1}\right)^2 \sum_x \left(\mathbf{s}_2(x) - \overline{s_2}\right)^2}} \tag{4.8}$$

When the signals are aligned properly, the difference (Euclidean distance) between the signals is calculated using Equation (4.9) to provide a confidence $\eta$ parameter for later use in the optimisation:

$$\eta = \frac{1}{\sum_x \left(\mathbf{s}_1(x) - \mathbf{s}_2(x)\right)^2} \tag{4.9}$$

The final confidence parameter $\epsilon$ is calculated using the results of both Equation (4.8) and Equation (4.9) as in Equation (4.10):

$$\epsilon = ((1+\gamma)\eta)^2 \tag{4.10}$$

where the best matching poses can be filtered by setting a threshold value to the calculated $\epsilon$. The corresponding poses that represent the filters $\mathbf{s}_1$ and $\mathbf{s}_2$ are added to the cost function Equation (4.7), with measured and expected distances given by Equation (4.11)

and Equation (4.12):

$$y_t = 0 \tag{4.11}$$

$$f_t = \widetilde{x_1^r} - \widetilde{x_2^r} \tag{4.12}$$

$\widetilde{x_1^r}$ and $\widetilde{x_2^r}$ are the corresponding poses when $\mathbf{s}_1$ and $\mathbf{s}_2$ signals are matching signals. The signal mapping process depends on a large number of poses in $\mathbf{x}_{0:T}^r$, which comes with heavy computational cost. However, the gradient (Jacobian) of the solution can be computed using a simple approximation of $f_t$, as in Equation (4.13):

$$F = [1, -1] \tag{4.13}$$

Further, the signal noise covariance $P_t$ is used as inversely proportional to $(\gamma \times \eta)$ to effectively weight the cost function in Equation (4.3).

## 4.3 Prototype Development

The system can be divided into a two-layered system architecture diagram as shown in Fig. 4.2.

### 4.3.1 Hardware Development

The RFID unit mounted on top of the robot was built using COTS components. A Thingmagic M6e Micro-LTE UHF 2 port RFID reader module with the embedded developer kit was used to implement the proposed system as it was easy to customise and supported by the open source Python MercuryAPI software community. Two 915 MHz General Purpose Panel RF antennas in the 902–928 MHz range with 5.5 dBi gain were used as the receiver antennas. An industry standard IR laser distance sensor with an 80 m range and 1 mm accuracy laser module was used to collect the robot's ground truth odometry. To compare the performance with the standard wheel encoder-based odometry, a 2,400 pulse-per-revolution rotary encoder was used to record the odometry. A Jetson Nano Developer kit board with Quad-core ARM 1.43 GHz CPU, 4 GB 64-bit

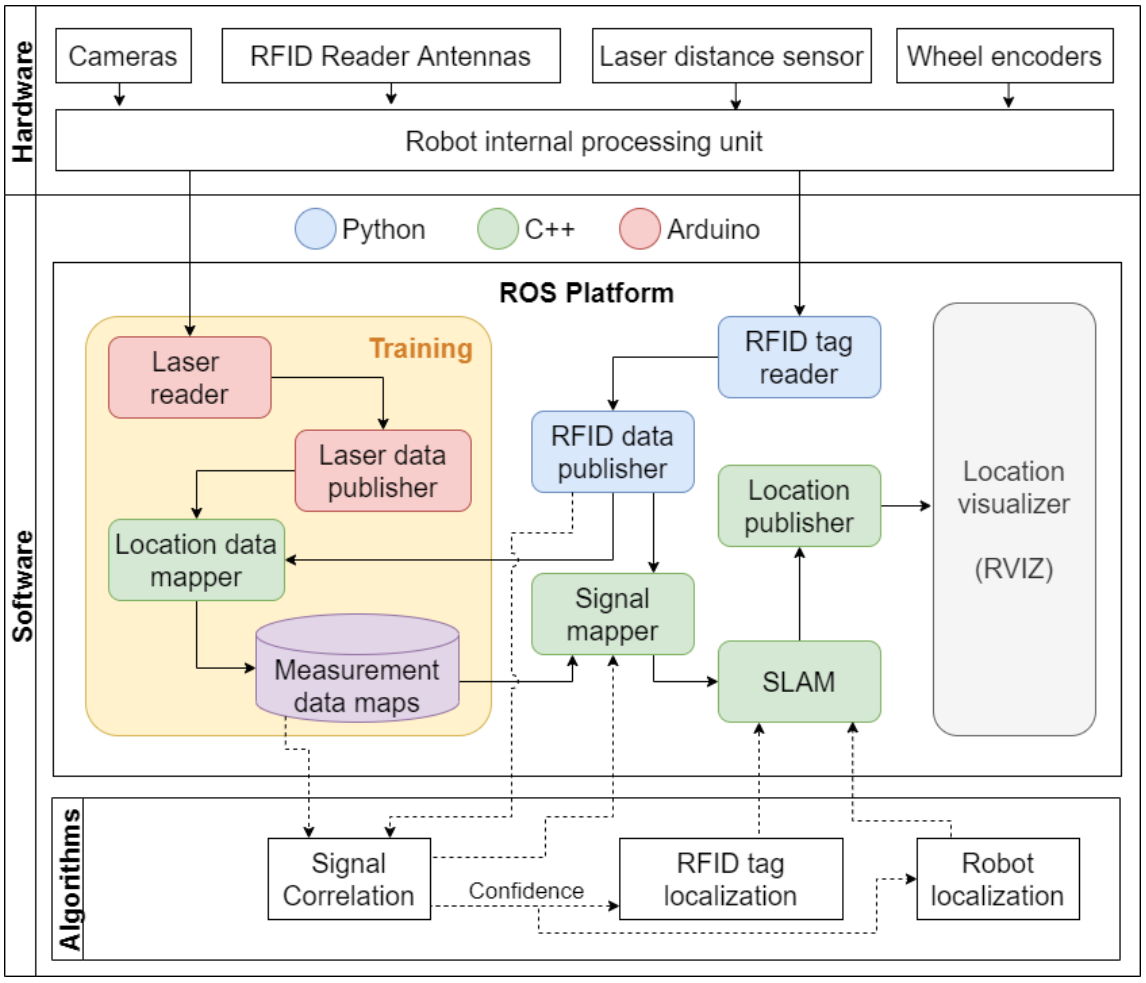


FIGURE 4.2: System architecture.

LPDDR4 RAM was used as the central processing unit to run the implemented system. The whole hardware system was assembled inside an enclosure and mounted on top of a robotic platform for deployment, as shown in Fig. 4.1.

### 4.3.2 Software Development

The software components are implemented using the ROS framework to gain the flexibility to modularise each component, as well as cross-language software support. Each individual component is implemented as an ROS node to make them communicate with each other effectively. RFID related components are implemented with Python as they are supported by the open source Python Mercury API library. To gain more structure and flexibility to implement the algorithms, the core integration is implemented

as C++ components. The laser distance sensor that tracks the ground truth odometry of the robot to create the measurement model is implemented as Arduino components. As the diagram elaborates, the RFID component receives the RSSI and phase data signals from the robot and publishes the data to the receiving components. In the training phase, the location mapper will combine the data with the robot odometry data received from the laser data publisher node. The collected data will be stored as measurement data maps for later use in the signal mapping. In the localisation phase, the data received from the robot will be mapped with the measurement model using the signal correlation algorithm. Based on the generated confidence values, the probabilities for robot and RFID tag locations will be calculated within the SLAM algorithm for each RFID tag signal. Finally, using these calculated values the highest probability of the robot localisation and RFID tag locations will be published to the location publisher node, which will be displayed in an RVIZ-like location visualiser system.

## 4.4 Experiments and Results

### 4.4.1 Data Collection and Modelling

First, all the RFID tags were placed in the middle of a 5 m long, 600 mm diameter sample lab pipe extracted from Sydney Water pipe network, which represents the conditions of a real-world underground water pipeline. Next, the robot was deployed from one end of the pipe to the other collecting the RSSI and phase signal patterns along the pipe that mapped to its location. A laser distance meter was used to map the robot's location for accurate ground truth measurement and accuracy validation.

When collecting data to generate the measurement data model and test data model the robot was deployed several times in the pipe that resulted in minor movement noises at each deployment. The observations showed that those minor movement noises of the robot pitch, roll and yaw did not impact much on the received signal strengths significantly. The comparison of two RFID signal differences at two deployments of the robot with minor movement noises gave approximately 0.95 correlation coefficient. Therefore, slight tilt or

role of the robot do not drastically affect the localisation accuracy. However, major role or tilt may cause localisation errors.

Next, a measurement model was created by mapping the robot's odometry values with all the RFID tag signals, uniquely identified by the tag EPC value. To increase the accuracy of the measurement model, the signal values were interpolated up to millimetre level. Fig. 4.3 shows the measurement data for the first 10 RFID tags. In total, around 50 tags were stored in the measurement model and distributed in the 50 m long pipeline with roughly 1 m separation. In practice, when deploying RFID sensor tags inside a pipeline, robot localisation is inaccurate because of the use of conventional localisation methods. Therefore, the locations of the RFID tags were not precisely known. Hence, the proposed localisation algorithm treats the RFID tag locations as unknown and performs the search for their locations.

Using the signal cross-correlation method and the pose-graph optimisation problem-solving localisation algorithm proposed in Section 4.2, the robot was deployed inside the real-world water pipeline and start estimating its trajectory while generating an RFID sensor tag location map using the received RFID RSSI signal patterns.

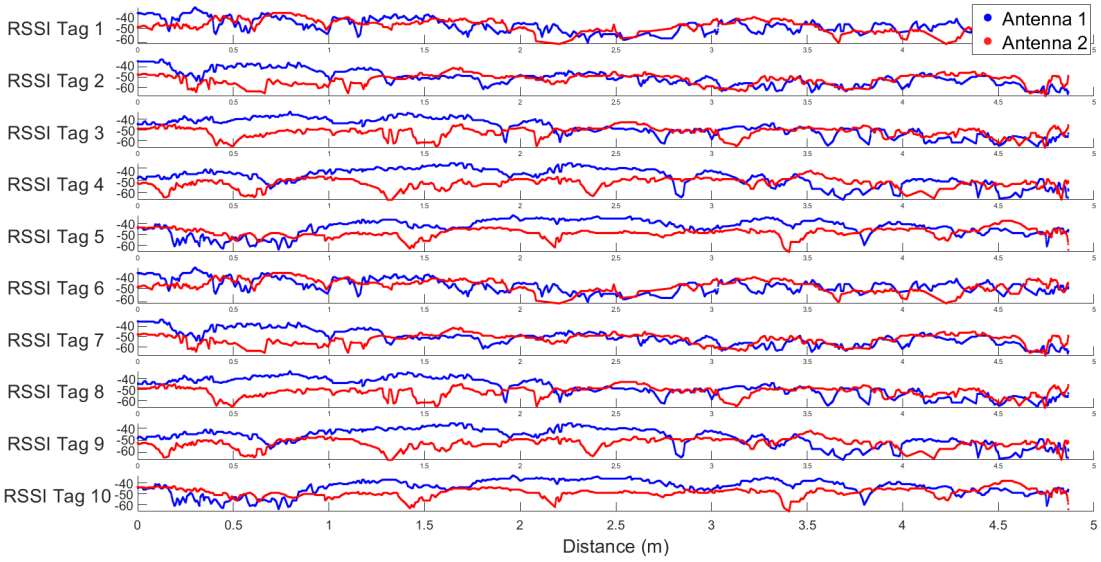


FIGURE 4.3: First 10 segments of the measurement model.

### 4.4.2 Signal Cross-correlation Mapping

Fig. 4.4 presents an example of a result from signal cross-correlation mapping for a given RFID tag for a given antenna. The top graph shows the measurement model signal pattern that maps to the laser distance readings. The middle graph contains the signal data received in real time that needs to align with the measurement model to map with the distance to identify the travel distance during the period of the received signal. The hardware can receive data at a frequency of approximately 70 Hz. The density and quality of the received signal data depend on the robot speed. Therefore, the signal scaling described in Section 4.2.3 when performing cross-correlation depends on the robot speed. Hence, the scale parameters are updated proportionally based on the speed of the robot via integration with the robot control commands. The bottom graph in Fig. 4.4 shows the results obtained by mapping the received signal to the matching measurement model signal, which facilitates correlating the data points with distance values.

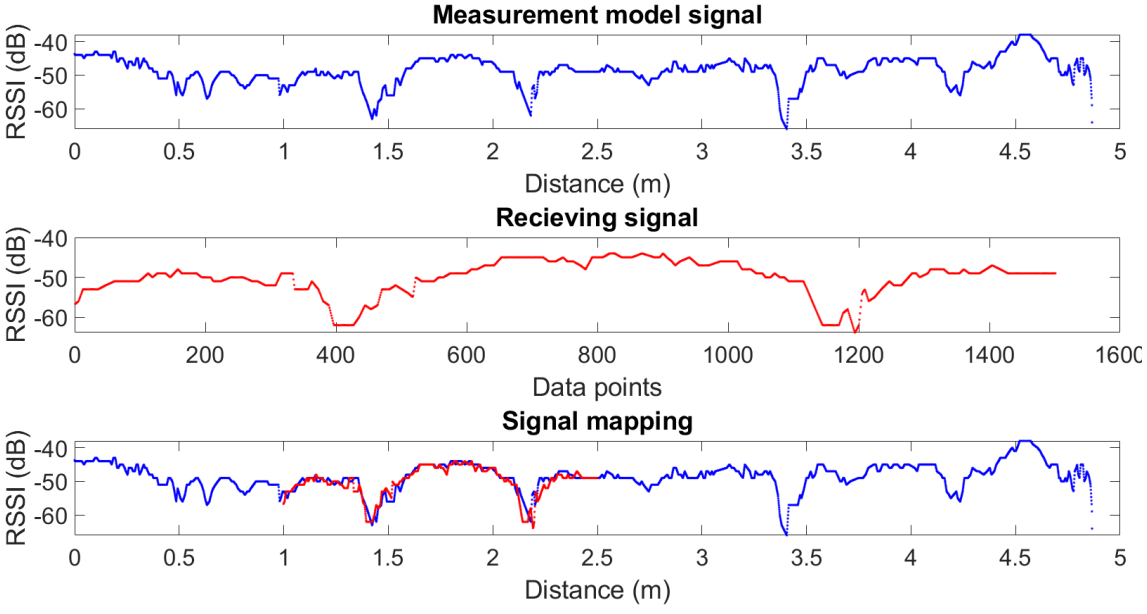


FIGURE 4.4: Signal cross-correlation mapping.

### 4.4.3 Robot Localisation

Fig. 4.5 shows the best performing robot localisation with its optimal configuration parameters, and Fig. 4.6 shows the mean error graph for the system performance. At the beginning of its travel path, the robot's localisation accuracy is lower because of the lack of received signal data points. The received signal might map to wrong locations in the measurement signal when it is too small. At around 3 m, when there are sufficient data to accurately map the signals, the accuracy of the robot localisation stabilises.

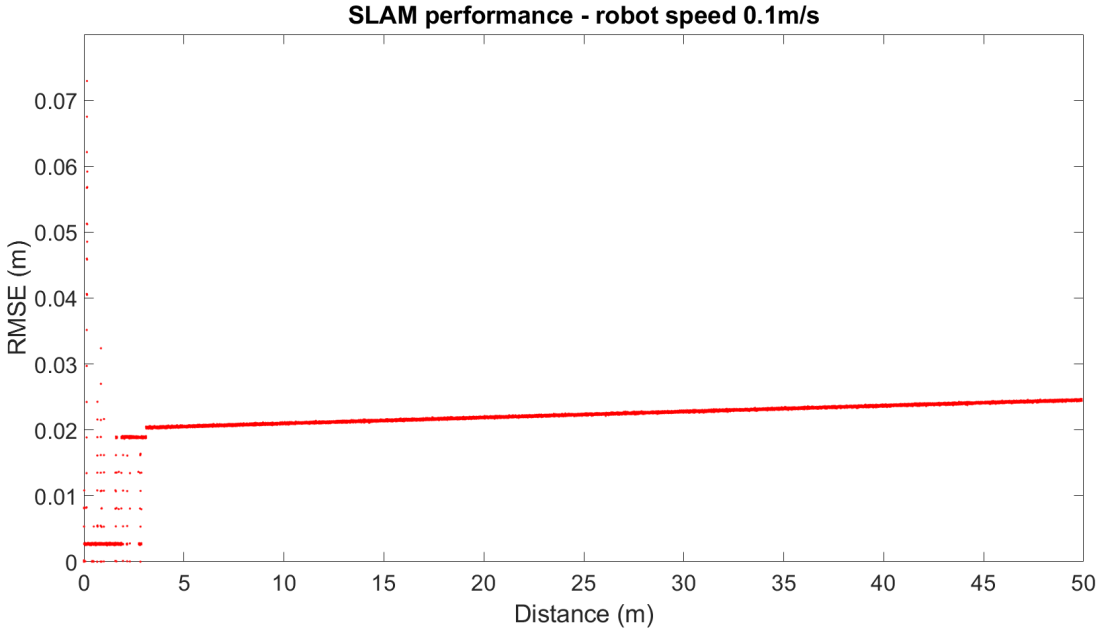


FIGURE 4.5: SLAM performance.

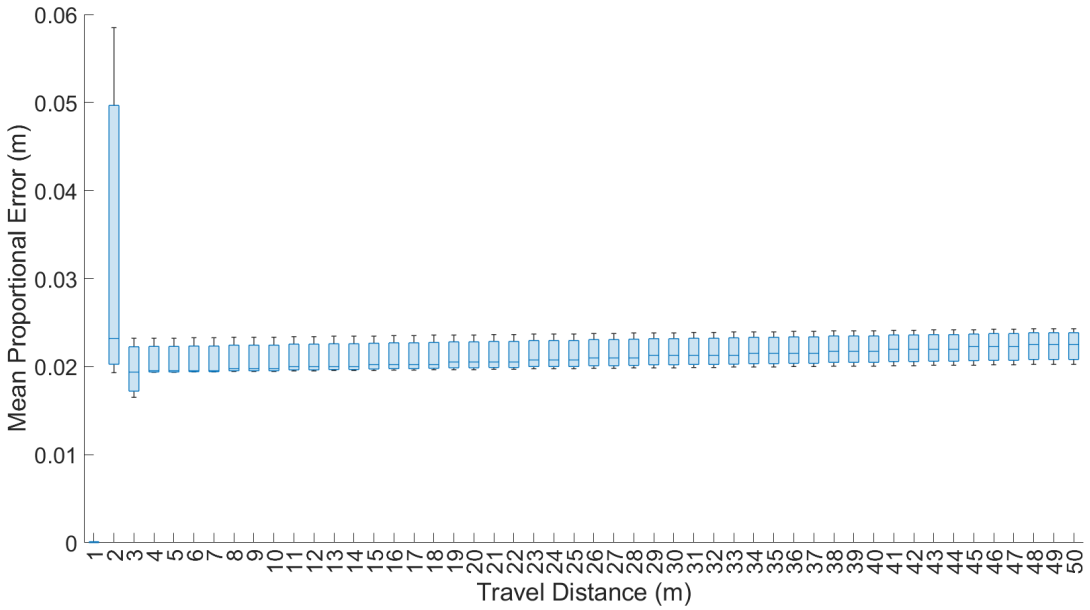


FIGURE 4.6: Whisker plot graph of 20 sets of trials with random noise.

Fig. 4.7 shows localisation results for different speeds of the robot. As the frequency of the RFID data received by the robot is at its max and is consistent, when the robot travels faster, the number of data points received at a particular location decreases, resulting in reduction in localisation accuracy. This is because when there are too few data points between RSSI signal readings, the signal cross-correlation mapping accuracy decreases, resulting in alignment of the received signal with inaccurate positions in the measurement model signal.

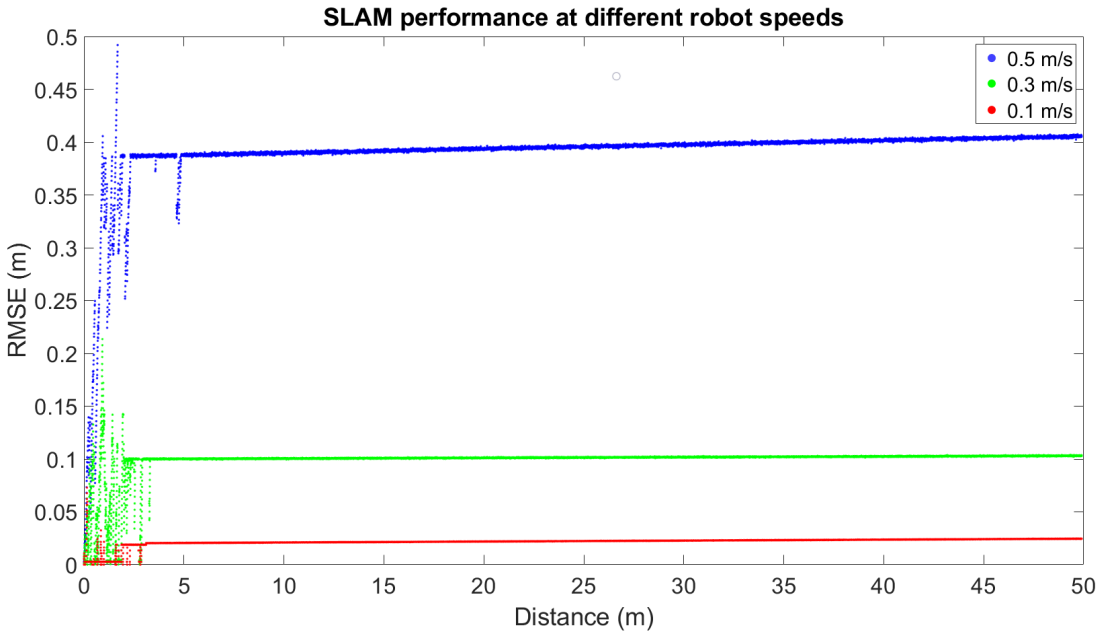


FIGURE 4.7: SLAM accuracy at different speeds of the robot.

### 4.4.4 RFID Tag Location Mapping

Fig. 4.8 shows the results from generating RFID tag signal maps. Since the RFID tag location is known to be at the middle of the signal pattern when building the measurement data model, the tag location inside the real underground pipeline can be located with signal cross-correlation mapping from the generated map. Comparison with the testing data allows the accuracy of the estimated RFID tag locations to be evaluated. The post-analytical results showed that the RFID tag locations were estimated with 2.5 cm accuracy.

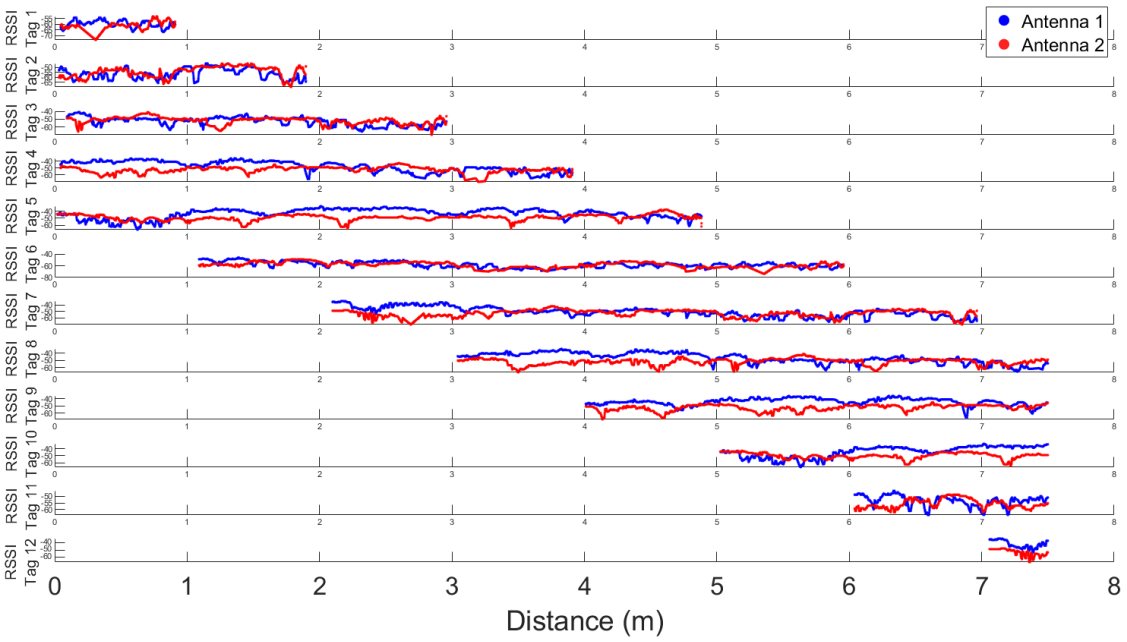


FIGURE 4.8: RFID tag signal mapping results at 7.5 m distance in pipe.

### 4.4.5 Comparison among Localisation Methods

A performance comparison was undertaken between the proposed system, the commonly used encoder odometry-based robot localisation system and the GP combined particle filter-based two-antenna model localisation method proposed in the Chapter 3 research work (when RFID tag locations are known).

Fig. 4.9 compares the results from the particle filter-based approach when the RFID terrain is known and the proposed SLAM-based approach when the RFID terrain is not known. In a known RFID terrain, the particle filter-based approach works well with millimetre-level accuracy but when the RFID terrain is not known, it is not applicable. Therefore, the SLAM approach can be used to generate an RFID terrain map with 2.5 cm localisation accuracy, and once the RFID terrain is known, particle filter-based localisation can be used for future localisation with better accuracy.

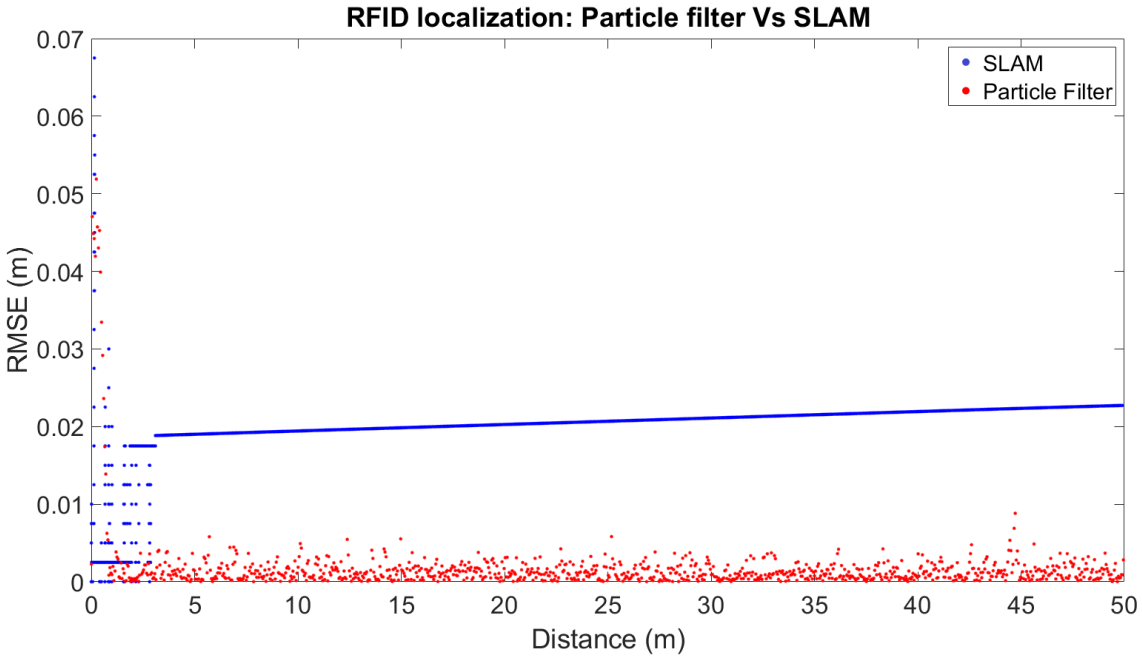


FIGURE 4.9: Particle filter vs. SLAM performance.

Fig. 4.10 compares the results from the proposed RFID-based localisation methods and the standard, commonly used encoder-based localisation method. The laser distance data were used as the ground truth measurement. It is clear that both particle filter and SLAM-based wireless RFID localisation performs far better than encoder-based localisation for long distances.

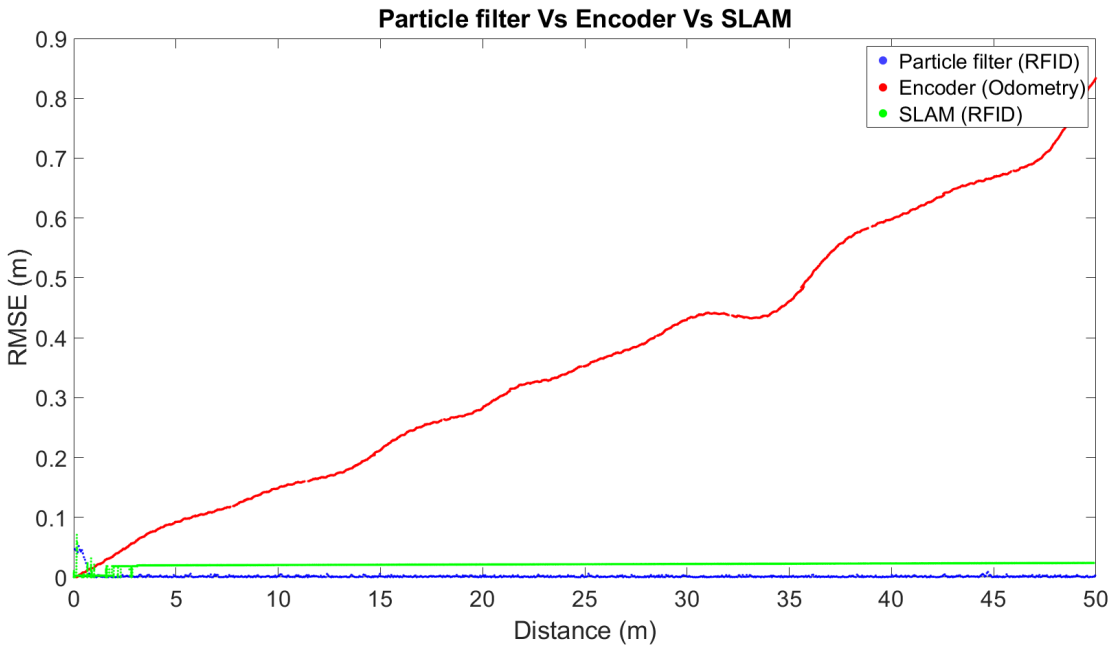


FIGURE 4.10: Particle filter vs. SLAM vs. encoder odometry performance.

Another comparison was made with methods proposed in the literature and conventional methods. Table 4.1 summarises the comparison results. The localisation methods proposed in this thesis show competitive accuracy compared with results for other methods reported in literature. Two typical conventional localisation methods [151, 152] show around 31 and 27 cm accuracy; two methods employing two RFID antennas in recent studies [140, 141] for outdoor and indoor localisation show around 50 and 6 cm accuracy; and an in-pipe localisation method proposed by Wu et al. [176] shows around 25 cm accuracy. The RFID localisation methods proposed in this thesis exhibit superior accuracy of 2.5 cm to 1 mm accuracy inside pipelines. Such accuracy has been achieved by using a twin antenna model, employing signal pattern difference of two antennas as an advantage, employing the signal reflection on the pipe surface and its long travel distance inside the pipe as an advantage, creating unique signal measurement models with training data, experimenting with best calibration parameters in hardware, software and algorithm, treating the localisation problem as one dimensional, etc.

Fig. 4.11 focuses the end of the 50 m long four laser profile alignments of ground truth; encoder; RFID particle filter localisation in a known terrain; and RFID SLAM localisation

| **Method** | **Position error Mean / mm** | **Position error Std. dev. / mm** |
|---|---|---|
| Conventional method in [151] | 271 | 113 |
| Conventional method in [152] | 310 | 139 |
| Method proposed in [140] | 500 | 200 |
| Method proposed in [141] | 59 | 36 |
| Method proposed in [176] | 250 | Not Given |
| Encoder based method | 833 | 214 |
| Proposed GP based PF method in chapter 3 | 1.8 | 1.62 |
| Proposed SLAM method | 23.3 | 3.8 |

TABLE 4.1: Performance comparison with existing localisation methods.

in unknown terrain. As seen in the image, a mark on the top of the pipe crown was used to measure localisation alignment differences. It is apparent that the encoder-localised laser profile is 0.817 m behind the ground truth laser profile. The RFID-localised laser profile in known terrain is perfectly aligned with the ground truth laser profile, with 0.001 m accuracy. The laser profile generated using RFID SLAM localisation aligns with the ground truth with 0.021 m distance accuracy. This proves that in practice, both RFID localisation techniques work well compared with standard encoder-based localisation for in-pipe robotics.

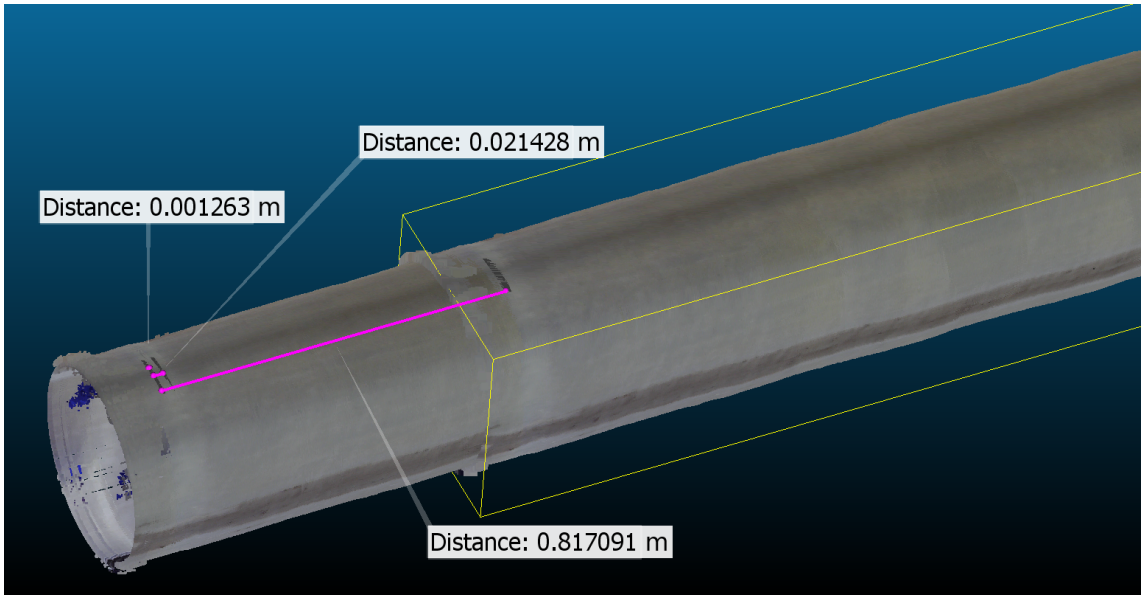


FIGURE 4.11: Laser profile localisation evaluation: RFID vs. encoder.

## 4.5 Summary

The chapter has described the development of a robotic system that uses battery-free UHF-RFID sensor signals for robot localisation, and a RFID RSSI signal cross-correlation mapping technique combined with a customised simultaneous localisation and mapping algorithm. The system was extensively tested and validated in sample laboratory pipe extracted from the Sydney Water pipe network, simulating a 50 m long pipeline. The results showed that the proposed system works well at localising the robot, with approximately 2.5 cm accuracy in unknown RFID terrain, simultaneously building an RFID tag location map. Further, the robot can be deployed from any location of the pipe and can travel at any direction while localising accurately. The system was evaluated against standard commonly used encoder-based localisation methods and existing indoor and outdoor localisation methods. The proposed solution provides superior results for longer distances. In future, the system can be further tested in different pipes under different environmental conditions and with longer pipe lengths.

The following publication was an outcome of the work presented in this chapter:

1. **A. Gunatilake**, K.Thiyagarajan, S. Kodagoda, "Robot Simultaneous Localization and Mapping Inside Pipelines Using UHF-RFID Signals," IEEE Robotics and Automation Letters. *(Under Review)*

# Chapter 5

# Conclusions

This thesis addresses current shortcomings of robotic sensing and localisation for effective monitoring of liners applied in underground water pipelines that become corroded, resulting in pipe burst and ground collapse through ageing of pipe assets and liner application imperfections. A complete robotic solution that can generate millimetre-level accuracy RGB-D maps to inspect the quality of pipe liner application inside the pipeline using accurate localisation methods based on UHF-RFID signals, is proposed.

The stereo vision-combined, structured IR laser-projected 3D profiling system is capable of generating millimetre-level accuracy RGB-D maps inside pipelines in real time. Further, it is capable of generating heat maps to provide an indication of the severity of any defects identified, while the RGB map provides true colour information enabling proper assessment of defect nature. This will help water utilities to properly monitor their pipelines, identify defects, and quantify them before and after liner application.

The accuracy of the laser profiling system and comparison between scans by aligning them is strongly dependent on the robot localisation system. Currently available conventional odometry systems did not meet the project requirements. Therefore, after evaluating many sensor technologies, a particle filter combined GP algorithm-based UHF-RFID signal localisation system was researched and implemented to localise the robot inside pipelines with up to millimetre-level accuracy when RFID tag locations are known. The proposed

localisation system can be used to localise a wide range of robotic systems including floating robots and drones inside pipelines, as it is wireless.

To achieve robot localisation in situations where RFID locations are not precisely known inside pipelines, a simultaneous localisation and mapping system was proposed and developed with a UHF-RFID signal cross-correlation-based improved measurement model. The proposed system is capable of localising the robot with up to approximately 2.5 cm accuracy.

The whole system was tested and validated in a field-extracted real underground water pipe sample from the Sydney Water network under different conditions simulating a 50 m pipe in the laboratory environment. The laser profiling system proposed in Chapter 1 was evaluated in field trials in real underground drinking water pipelines with different liner technologies located in Sydney, Australia.

## 5.1 Summary of Contributions

### 5.1.1 Robotic Mapping of Internal Pipeline Defects through Stereo Vision-combined Laser Profiling

- A stereo vision-based laser profiling system is proposed with an integrated mobile robotic platform for real-time RGB-D mapping and true colour information extracted from the pipelines using colour and IR cameras. The proposed approach requires only one-time calibration and generates RGB-D maps with 1 mm accuracy for pipe diameters ranging from 400 to 700 mm.

- The system generates heat maps that highlight and measure defective areas in scanned pipelines, which enables easy monitoring of damaged areas and their evolution in the long term.

- The stereo vision is utilised for detecting the orientation of the robot by determining yaw and pitch parameters, which assists in accurate RGB-D map building.

- The proposed system has been tested with different liner technologies in real underground drinking water pipelines for 120 m of pipe lengths in Sydney Water pipe network.

### 5.1.2 UHF-RFID Sensor Wireless Signals for Accurate In-pipe Robot Localisation

- A UHF-RFID signal-based robotic localisation system is presented that uses a particle filter combined GP algorithm. Its accuracy is further enhanced by utilising both RSSI and phase data in the particle filter measurement model.
- The system can be used for robot localisation without the aid of any other odometry systems after creating an initial measurement model, and can accurately localise the robot up to millimetre level.
- The system is capable of aligning the laser profile scans taken at different times with millimetre-level accuracy to map corresponding defects in each 3D profile for monitoring their evolution. The solution has been tested in sample laboratory pipes extracted from the Sydney Water network, simulating a pipe length of 50 m.

### 5.1.3 Simultaneous Localisation and Mapping Inside Pipelines Using UHF-RFID Signals

- A robotic localisation system is presented that uses a simultaneous localisation and mapping algorithm, with a custom measurement model using UHF-RFID signal cross-correlation.
- The system can be deployed from any location within the pipe and can travel in any direction while localising the robot with approximately 2.5 cm accuracy, and mapping RFID tag locations inside the pipeline where RFID locations are not exactly known.
- The system works independently without the aid of any other odometry systems and only requires a training data set acquired from a laboratory pipe sample. It does not require any field calibration to perform at the site.

## 5.2 Discussions and Future Research

The current version of the robotic sensing system was developed to scan straight pipes ranging from 400 to 700 mm in diameter and spanning around 100 m of length from one manhole to the next. In future, the system can be extended to other pipe sizes with more complex pipe networks including bends and pipe junctions. Further research should aim to overcome the limitation discussed in relation to the laser profiling unit, where black surfaces present low measurement accuracy and possible issues relating to shading.

Currently, the proposed UHF-RFID localisation system works with a pre-acquired, one-time training data set in the laboratory. In future, research might focus on finding a solution that can localise the robot without the requirement for training data sets. Insights into an analytical model representing the unique UHF-RFID signal pattern inside pipelines may be useful. To achieve higher accuracy in robot localisation, the proposed solution requires a large number of RFID tags deployed inside the pipeline with 1 m separation. Future research might focus on minimising the number of RFID tag deployments, while maintaining localisation accuracy.

As a result of the COVID-19 pandemic and associated movement restrictions, the UHF-RFID-based localisation systems proposed in Chapter 3 and 4 were tested only in the laboratory environment, employing a field-extracted pipe sample. In future, the system should be tested in the real-world underground Sydney Water pipe network for longer pipe lengths and further validation, as well as further improvements.

# Bibliography


[1] David Wiley. 3 Tips to Avoid Future Pipe Lining Complications, Jul 2018. URL `https://www.nuflowmidwest.com/3-tips-to-avoid-future-pipe-lining-complications/`.

[2] Amal Gunatilake, Lasitha Piyathilaka, Sarath Kodagoda, Stephen Barclay, and Dammika Vitanage. Real-Time 3D Profiling with RGB-D Mapping in Pipelines Using Stereo Camera Vision and Structured IR Laser Ring. In *2019 14th IEEE Conference on Industrial Electronics and Applications (ICIEA)*, pages 916–921, 2019. doi: 10.1109/ICIEA.2019.8834089.

[3] Amal Gunatilake, Lasitha Piyathilaka, Antony Tran, Vinoth Kumar Vishwanathan, Karthick Thiyagarajan, and Sarath Kodagoda. Stereo Vision Combined With Laser Profiling for Mapping of Pipeline Internal Defects. *IEEE Sensors Journal*, 21(10): 11926–11934, 2021. doi: 10.1109/JSEN.2020.3040396.

[4] Amal Gunatilake, Mitchell Galea, Karthick Thiyagarajan, Sarath Kodagoda, Lasitha Piyathilaka, and Poojaben Darji. Using UHF-RFID Signals for Robot Localization Inside Pipelines. In *2021 IEEE 16th Conference on Industrial Electronics and Applications (ICIEA)*, pages 1109–1114, 2021. doi: 10.1109/ICIEA51954.2021.9516284.

[5] Amal Gunatilake, Karthick Thiyagarajan, and Sarath Kodagoda. Evaluation of Battery-free UHF-RFID Sensor Wireless Signals for In-pipe Robotic Applications. In *2021 IEEE SENSORS*, pages 1–4, 2021.

[6] Maria Almeida, Dídia Covas, and Paula Beceiro. *Rehabilitation of sewers and manholes: technologies and operational practices*, volume 6. TRUST Manual of Best Practice, 04 2015. doi: 10.13140/RG.2.1.3207.0005.

[7] Zheng Liu and Yehuda Kleiner. State of the art review of inspection technologies for condition assessment of water pipes. *Measurement*, 46(1):1–15, January 2013. doi: 10.1016/j.measurement.2012.05.032.

[8] Carlos Rizzo, Teresa Seco, Jesús Espelosín, Francisco Lera, and José Luis Villarroel. An alternative approach for robot localization inside pipes using RF spatial fadings. *Robotics and Autonomous Systems*, 136:103702, February 2021. doi: 10.1016/j.robot.2020.103702.

[9] Jaime Valls Miro, Dave Hunt, Nalika Ulapane, and Michael Behrens. Towards automatic robotic NDT dense mapping for pipeline integrity inspection. In *Field and Service Robotics*, pages 319–333. Springer International Publishing, November 2017. doi: 10.1007/978-3-319-67361-5_21.

[10] Josep M. Mirats Tur and William Garthwaite. Robotic devices for water main in-pipe inspection: A survey. *Journal of Field Robotics*, 27(4):491–508, June 2010. doi: 10.1002/rob.20347.

[11] Linh Nguyen and Jaime Valls Miro. Efficient evaluation of remaining wall thickness in corroded water pipes using pulsed eddy current data. *IEEE Sensors Journal*, 20 (23):14465–14473, December 2020. doi: 10.1109/jsen.2020.3007868.

[12] Jaime Valls Miro, Nalika Ulapane, Lei Shi, Dave Hunt, and Michael Behrens. Robotic pipeline wall thickness evaluation for dense nondestructive testing inspection. *Journal of Field Robotics*, 35(8):1293–1310, November 2018. doi: 10.1002/rob.21828.

[13] Nalika Ulapane, Karthick Thiyagarajan, Jaime Valls Miro, and Sarath Kodagoda. Surface representation of pulsed eddy current sensor signals for improved ferromagnetic material thickness quantification. *IEEE Sensors Journal*, 21(4):5413–5422, February 2021. doi: 10.1109/jsen.2020.3034571.

[14] Linh Nguyen and Jaime Valls Miro. An efficient 3-d model for remaining wall thicknesses of cast iron pipes in nondestructive testing. *IEEE Sensors Letters*, 4 (7):1–4, July 2020. doi: 10.1109/lsens.2020.2999330.

[15] Sarath Kodagoda and Karthick Thiyagarajan. Performance monitoring of liners: Parameter identification, Oct 2018. URL `https://www.waterportal.com.au/smartlinings/images/Deliverables/31_UTS_Literature_Review_FINAL.pdf`.

[16] Dammika Vitanage, Greg Allen, and Jayantha Kumarasiri Kodikara. Collaborative research on condition assessment and pipe failure prediction for critical water mains. *Water Asset Management International*, 10(3):15 – 18, 2014. ISSN 1814-5434.

[17] Susen Das, Alireza Bayat, Leon Gay, Mahmoud Salimi, and John Matthews. A comprehensive review on the challenges of cured-in-place pipe (cipp) installations. *Journal of Water Supply: Research and Technology - Aqua*, 65, 10 2016. doi: 10.2166/aqua.2016.119.

[18] John Matthews, W Condit, Ryan Wensink, and Gary Lewis. Performance evaluation of innovative water main rehabilitation cured-in-place pipe lining product in cleveland. *Battelle Memorial Institute, EPA (Environmental Protection Agency). NJ and OH*, 02 2012. doi: 10.13140/2.1.3259.5526.

[19] H. Ji, D. Koo, and Jeong-Hee Kang. Short- and long-term structural characterization of cured-in-place pipe liner with reinforced glass fiber material. *International Journal of Environmental Research and Public Health*, 17, 2020.

[20] A. Selvakumar, John Matthews, Sai Vaidya, and Wendy Condit. Large-diameter sewer rehabilitation using a spray-applied fiber-reinforced geopolymer mortar. *Practice Periodical on Structural Design and Construction*, 20, 11 2015.

[21] A. Selvakumar, John Matthews, and Wendy Condit. Performance evaluation of an innovative fiber reinforced geopolymer spray-applied mortar for large diameter wastewater main rehabilitation in houston, tx. *United States Environmental Protection Agencies, EPA (Environmental Protection Agency). NJ and OH*, 12 2014. doi: 10.13140/2.1.2185.2964.

[22] A. Selvakumar, John Matthews, and Wendy Condit. Performance evaluation of innovative water main rehabilitation spray-on lining product in somerville, nj. *United States Environmental Protection Agencies, EPA (Environmental Protection Agency). NJ and OH*, 02 2012.

[23] Awe, Olukayode. Testing of innovative pipe renewal liners for renovation of potable water distribution pipelines. Master's thesis, University of Waterloo, 2017. URL `http://hdl.handle.net/10012/12755`.

[24] Daniil Vasilikis and Spyros Karamanos. Mechanical behavior and wrinkling of lined pipes. *International Journal of Solids and Structures*, 49:3432–3446, 11 2012. doi: 10.1016/j.ijsolstr.2012.07.023.

[25] Daisy Sharma, Manju Rawat, Jyoti Sharma, Suresh Ahuja, Avinash Chandra, Sanghamitra Barman, and Raj Arya. *Polymer Coatings Technology and Applications: Polymer Coating Mehods.* CRC Press, 01 2021. ISBN 9780429199226. doi: 10.1201/9780429199226.

[26] Andreu Corominas Murtra and Josep M. Mirats Tur. Imu and cable encoder data fusion for in-pipe mobile robot localization. In *2013 IEEE Conference on Technologies for Practical Robot Applications (TePRA)*, pages 1–6, 2013. doi: 10.1109/TePRA.2013.6556377.

[27] K Thiyagarajan, S Kodagoda, L Van Nguyen, and R Ranasinghe. Sensor Failure Detection and Faulty Data Accommodation Approach for Instrumented Wastewater Infrastructures. *IEEE Access*, 6:56562–56574, 2018. ISSN 2169-3536 VO - 6. doi: 10.1109/ACCESS.2018.2872506.

[28] L. Chun-Lei, S. Hao, L. Chun-Lai, and L. Jin-Yang. Intelligent detection for tunnel shotcrete spray using deep learning and lidar. *IEEE Access*, 8:1755–1766, 2020.

[29] Z. Li, P. C. Gogia, and M. Kaess. Dense surface reconstruction from monocular vision and lidar. In *2019 International Conference on Robotics and Automation (ICRA)*, pages 6905–6911, 2019.

[30] J. Zhang, Z. Lu, W. Li, and Q. Liao. A robust and fast 3d face reconstruction method using realsense camera. In *2017 International Conference on Wireless*

*Communications, Signal Processing and Networking (WiSPNET)*, pages 2691–2695, 2017.

[31] J. Feulner, J. Penne, E. Kollorz, and J. Hornegger. Robust real-time 3d modeling of static scenes using solely a time-of-flight sensor. In *2009 IEEE Computer Society Conference on Computer Vision and Pattern Recognition Workshops*, pages 74–81, 2009.

[32] S. M. Ayaz, D. Khan, and M. Y. Kim. 3d handheld scanning based on multiview 3d registration using kinect sensing device. In *2017 IEEE International Conference on Multisensor Fusion and Integration for Intelligent Systems (MFI)*, pages 330–335, 2017.

[33] M Nasrollahi, N Bolourian, Z Zhu, and A Hammad. Designing LiDAR-equipped UAV platform for structural inspection. In *35th International Symposium on Automation and Robotics in Construction and International AEC/FM Hackathon: The Future of Building Things, ISARC 2018*, Department of Building, Civil and Environmental Engineer, Concordia University, Canada, 2018. International Association for Automation and Robotics in Construction I.A.A.R.C).

[34] Yoshiaki Bando, Hiroki Suhara, Motoyasu Tanaka, Tetsushi Kamegawa, Katsutoshi Itoyama, Kazuyoshi Yoshii, Fumitoshi Matsuno, and Hiroshi G. Okuno. Sound-based online localization for an in-pipe snake robot. In *2016 IEEE International Symposium on Safety, Security, and Rescue Robotics (SSRR)*. IEEE, October 2016. doi: 10.1109/ssrr.2016.7784300.

[35] Rob Worley, Ke Ma, Gavin Sailor, Michele M. Schirru, Rob Dwyer-Joyce, Joby Boxall, Tony Dodd, Richard Collins, and Sean Anderson. Robot localization in water pipes using acoustic signals and pose graph optimization. *Sensors*, 20(19): 5584, September 2020. doi: 10.3390/s20195584.

[36] Karthick Thiyagarajan, Sarath Kodagoda, Ravindra Ranasinghe, Dammika Vitanage, and Gino Iori. Robust Sensor Suite Combined with Predictive Analytics Enabled Anomaly Detection Model for Smart Monitoring of Concrete Sewer Pipe

Surface Moisture Conditions. *IEEE Sensors Journal*, 20(15):8232–8243, 2020. ISSN 1530-437X. doi: 10.1109/JSEN.2020.2982173.

[37] Karthick Thiyagarajan, Sarath Kodagoda, Ravindra Ranasinghe, and Gino Iori. Robust sensing suite for measuring temporal dynamics of surface temperature in sewers. *Scientific Reports*, 8, 10 2018. doi: 10.1038/s41598-018-34121-3.

[38] M. Kamata, S. Yamazaki, Y. Tanise, Y. Yamada, and T. Nakamura. Morphological change in peristaltic crawling motion of a narrow pipe inspection robot inspired by earthworm's locomotion. *Advanced Robotics*, 32(7):386–397, 2018. doi: 10.1080/01691864.2017.1417158.

[39] GH Mills, JHW Liu, BY Kaddouh, AE Jackson, and RC Richardson. Miniature magnetic robots for in-pipe locomotion, November 2018. URL `https://eprints.whiterose.ac.uk/145800/`. © Elsevier. This work is under the international license Creative Commons Attribution-NonCommercial-NoDerivatives 4.0. To view a copy of this license, visit https://creativecommons.org/licenses/by-nc-nd/4.0/.

[40] Keichi Kusunose, Tetsuya Akagi, Shujiro Dohta, Wataru Kobayashi, and Kengo Nakagawa. Development of pipe holding mechanism and bending unit using extension type flexible actuator for flexible pipe inspection robot. *International Journal of Mechanical Engineering and Robotics Research*, 8(1):129–134, 2019.

[41] Kentaro Miyasaka, Ginjiro Kawano, and Hideyuki Tsukagoshi. Long-mover: Flexible tube in-pipe inspection robot for long distance and complex piping. In *2018 IEEE/ASME International Conference on Advanced Intelligent Mechatronics (AIM)*, pages 1075–1080, 2018. doi: 10.1109/AIM.2018.8452690.

[42] Rohit Kashyap, Rahul Kashyap, Rohan Kumbhar, and Amrut Chari. Design of reconfigurable in-pipe exploration robots. In *2018 International Conference on Current Trends towards Converging Technologies (ICCTCT)*, pages 1–6, 2018. doi: 10.1109/ICCTCT.2018.8551187.

[43] Qingyou Liu, Tao Ren, and Yonghua Chen. Characteristic analysis of a novel in-pipe driving robot. *Mechatronics*, 23(4):419–428, 2013.

[44] Young-Sik Kwon and Byung-Ju Yi. Development of a pipeline inspection robot system with diameter of 40mm to 70mm (tbot-40). In *2010 IEEE International Conference on Mechatronics and Automation*, pages 258–263, 2010. doi: 10.1109/ICMA.2010.5589084.

[45] A Cengel Yunus. *Fluid Mechanics: Fundamentals And Applications (Si Units)*. Tata McGraw Hill Education Private Limited, 2010.

[46] Edwin Dertien, Mohammad Mozaffari Foumashi, Kees Pulles, and Stefano Stramigioli. Design of a robot for in-pipe inspection using omnidirectional wheels and active stabilization. In *2014 IEEE International Conference on Robotics and Automation (ICRA)*, pages 5121–5126, 2014. doi: 10.1109/ICRA.2014.6907610.

[47] S. Cowls and S. Jordan. The enhancement and verification of a pulse induction based buried pipe and cable survey system. In *OCEANS '02 MTS/IEEE*, volume 1, pages 508–511 vol.1, 2002. doi: 10.1109/OCEANS.2002.1193320.

[48] Dongwoo Lee, Jungwan Park, Dongjun Hyun, GyungHwan Yook, and Hyun-seok Yang. Novel mechanisms and simple locomotion strategies for an in-pipe robot that can inspect various pipe types. *Mechanism and Machine Theory*, 56:52–68, 2012.

[49] Jun-ya Nagase and Fumika Fukunaga. Development of a novel crawler mechanism for pipe inspection. In *IECON 2016 - 42nd Annual Conference of the IEEE Industrial Electronics Society*, pages 5873–5878, 2016. doi: 10.1109/IECON.2016.7793844.

[50] Ren Tao, Yonghua Chen, and Liu Qingyou. A helical drive in-pipe robot based on compound planetary gearing. *Advanced Robotics*, 28(17):1165–1175, 2014.

[51] Enna Sachdeva, Akash Singh, Abhishek Sarkar, and K. Madhava Krishna. Design and optimal springs stiffness estimation of a modular omnicrawler in-pipe climbing robot. In *2017 IEEE International Conference on Robotics and Biomimetics (ROBIO)*, pages 1912–1917, 2017. doi: 10.1109/ROBIO.2017.8324698.

[52] Saeed Jerban and Majid M. Moghaddam. On the in-pipe inspection robots traversing through elbows. *International Journal of Robotics Theory and Applications*, 4:19–27, 08 2015.

[53] Atsushi Kakogawa and Shugen Ma. Design of a multilink-articulated wheeled pipeline inspection robot using only passive elastic joints. *Advanced Robotics*, 32 (1):37–50, 2018.

[54] Danial Waleed, Syed Hamdan Mustafa, Shayok Mukhopadhyay, Mamoun F. Abdel-Hafez, Mohammad Abdel Kareem Jaradat, Kevin Rose Dias, Fahad Arif, and Jawwad Imtiaz Ahmed. An in-pipe leak detection robot with a neural-network-based leak verification system. *IEEE Sensors Journal*, 19(3):1153–1165, 2019. doi: 10.1109/JSEN.2018.2879248.

[55] Changrak Choi, Dimitris Chatzigeorgiou, Rached Ben-Mansour, and Kamal Youcef-Toumi. Design and analysis of novel friction controlling mechanism with minimal energy for in-pipe robot applications. In *2012 IEEE International Conference on Robotics and Automation*, pages 4118–4123, 2012. doi: 10.1109/ICRA.2012.6225380.

[56] Argel A. Bandala, Jose Martin Z. Maningo, Arvin H. Fernando, Ryan Rhay P. Vicerra, Micah Antoinette B. Antonio, Julianne Alyson I. Diaz, Manuel Ligeralde, and Philix Anton R. Mascardo. Control and mechanical design of a multi-diameter tri-legged in- pipe traversing robot. In *2019 IEEE/SICE International Symposium on System Integration (SII)*, pages 740–745, 2019. doi: 10.1109/SII.2019.8700363.

[57] O. Duran, K. Althoefer, and L.D. Seneviratne. Automated pipe inspection using ann and laser data fusion. In *IEEE International Conference on Robotics and Automation, 2004. Proceedings. ICRA '04. 2004*, volume 5, pages 4875–4880 Vol.5, 2004. doi: 10.1109/ROBOT.2004.1302490.

[58] Mohammadreza Motamedi, Farrokh Faramarzi, and Olga Duran. New concept for corrosion inspection of urban pipeline networks by digital image processing. In *IECON 2012 - 38th Annual Conference on IEEE Industrial Electronics Society*, pages 1551–1556, 2012. doi: 10.1109/IECON.2012.6388510.

[59] O. Duran, K. Althoefer, and L.D. Seneviratne. A sensor for pipe inspection: model, analysis and image extraction. In *Proceedings 2003 International Conference on Image Processing (Cat. No.03CH37429)*, volume 3, pages III–597, 2003. doi: 10.1109/ICIP.2003.1247315.

[60] N. Giovanangeli, L. Piyathilaka, S. Kodagoda, K. Thiyagarajan, S. Barclay, and D. Vitanage. Design and development of drill-resistance sensor technology for accurately measuring microbiologically corroded concrete depths. In *Proceedings of the 36th International Symposium on Automation and Robotics in Construction*, pages 735–742. IAARC, 2019. doi: 10.22260/isarc2019/0099.

[61] Martin Ams, Peter Ha, Shima Taheri, Simon Clark, Michael J. Withford, Heriberto Bustamante, Jose Gonzalez, and Louisa Vorreiter. Fibre optic temperature and humidity sensors for harsh wastewater environments. In *2017 Eleventh International Conference on Sensing Technology (ICST)*, pages 1–3, 2017. doi: 10.1109/ICSensT.2017.8304493.

[62] Karthick Thiyagarajan, Sarath Kodagoda, Linh Van Nguyen, and Ravindra Ranasinghe. Sensor Failure Detection and Faulty Data Accommodation Approach for Instrumented Wastewater Infrastructures. *IEEE Access*, 6:56562–56574, 2018. doi: 10.1109/ACCESS.2018.2872506.

[63] R. V. Canales and C. M. Furukawa. Signal processing for corrosion assessment in pipelines with ultrasound pig using matched filter. In *2010 9th IEEE/IAS International Conference on Industry Applications - INDUSCON 2010*, pages 1–6, 2010. doi: 10.1109/INDUSCON.2010.5740075.

[64] Z Liu and D Krys. The use of laser range finder on a robotic platform for pipe inspection. *Mechanical Systems and Signal Processing*, 31:246–257, 2012. ISSN 08883270 (ISSN). doi: 10.1016/j.ymssp.2012.03.006.

[65] J Saenz, N Elkmann, T Stuerze, S Kutzner, and H Althoff. Robotic systems for cleaning and inspection of large concrete pipes. In *2010 1st International Conference on Applied Robotics for the Power Industry, CARPI 2010*, Fraunhofer IFF, 39106 Magdeburg, Germany, 2010. ISBN 9781424466337 (ISBN). doi: 10.1109/CARPI.2010.5624448.

[66] O Duran, K Althoefer, and L D Seneviratne. Automated pipe defect detection and categorization using caniera/laser-based profiler and artificial neural network. *IEEE*

*Transactions on Automation Science and Engineering*, 4(1):118–126, 2007. ISSN 15455955 (ISSN). doi: 10.1109/TASE.2006.873225.

[67] J.-S. Yoon, M Sagong, J S Lee, and K.-s. Lee. Feature extraction of a concrete tunnel liner from 3D laser scanning data. *NDT and E International*, 42(2):97–105, 2009. ISSN 09638695 (ISSN). doi: 10.1016/j.ndteint.2008.10.001.

[68] O. Duran, K. Althoefer, and L.D. Seneviratne. Laser profiler model for robot-based pipe inspection. In *Proceedings World Automation Congress, 2004.*, volume 15, pages 353–358, 2004.

[69] O. Duran, K. Althoefer, and L.D. Seneviratne. Experiments using a laser-based transducer and automated analysis techniques for pipe inspection. In *2003 IEEE International Conference on Robotics and Automation (Cat. No.03CH37422)*, volume 2, pages 2561–2566 vol.2, 2003. doi: 10.1109/ROBOT.2003.1241978.

[70] R Rantoson, C Stolz, D Fofi, and F Mériaudeau. Non contact 3D measurement scheme for transparent objects using UV structured light. In *2010 20th International Conference on Pattern Recognition, ICPR 2010*, pages 1646–1649, Laboratoire Le2i-CNRS UMR 5158, Université de Bourgogne, 12, Rue de la Fonderie, 71 200 Le Creusot, France, 2010. ISBN 10514651 (ISSN); 9780769541099 (ISBN). doi: 10.1109/ICPR.2010.407.

[71] J Kofman, J T Wu, and K Borribanbunpotkat. Multiple-line full-field laser-camera range sensor. In *Optomechatronic Computer-Vision Systems II*, volume 6718, Dept. Systems Design Engineering, University of Waterloo, Waterloo, ON N2L 3G1, Canada, 2007. ISBN 0277786X (ISSN); 9780819468666 (ISBN). doi: 10.1117/12.754551.

[72] N Stanić, M Lepot, M Catieau, J Langeveld, and F.H.L.R. Clemens. A technology for sewer pipe inspection (part 1): Design, calibration, corrections and potential application of a laser profiler. *Automation in Construction*, 75:91–107, 2017. ISSN 09265805 (ISSN). doi: 10.1016/j.autcon.2016.12.005.

[73] Mathieu Lepot, Nikola Stanić, and François H L R Clemens. A technology for sewer pipe inspection (Part 2): Experimental assessment of a new laser profiler for sewer

defect detection and quantification. *Automation in Construction*, 73:1–11, 2017. ISSN 0926-5805. doi: https://doi.org/10.1016/j.autcon.2016.10.010.

[74] E Ujkani, J Dybedal, A Aalerud, K B Kaldestad, and G Hovland. Visual Marker Guided Point Cloud Registration in a Large Multi-Sensor Industrial Robot Cell. In *14th IEEE/ASME International Conference on Mechatronic and Embedded Systems and Applications, MESA 2018*, Department of Engineering Sciences, Mechatronics Group, University of Agder, Norway, 2018. IEEE Inc. ISBN 9781538646434 (ISBN). doi: 10.1109/MESA.2018.8449195.

[75] Luis R Ramírez-Hernández, Julio C Rodríguez-Quiñonez, Moises J Castro-Toscano, Daniel Hernández-Balbuena, Wendy Flores-Fuentes, Raúl Rascón-Carmona, Lars Lindner, and Oleg Sergiyenko. Improve three-dimensional point localization accuracy in stereo vision systems using a novel camera calibration method. *International Journal of Advanced Robotic Systems*, 17(1):1729881419896717, 2020. doi: 10.1177/1729881419896717.

[76] Guo Ning, Li Lei, Yan Feng, and Li Tongtong. Binocular stereo vision calibration based on constrained sparse beam adjustment algorithm. *Optik*, 208:163917, 2020. ISSN 0030-4026. doi: https://doi.org/10.1016/j.ijleo.2019.163917.

[77] Shoubo Yang, Yang Gao, Zhen Liu, and Guangjun Zhang. A calibration method for binocular stereo vision sensor with short-baseline based on 3d flexible control field. *Optics and Lasers in Engineering*, 124:105817, 2020. ISSN 0143-8166. doi: https://doi.org/10.1016/j.optlaseng.2019.105817.

[78] Mo Yuda, Zou Xiangjun, Situ Weiming, and Luo Shaofeng. Target accurate positioning based on the point cloud created by stereo vision. In *2016 23rd International Conference on Mechatronics and Machine Vision in Practice (M2VIP)*, pages 1–5, 2016. doi: 10.1109/M2VIP.2016.7827268.

[79] P. Li, R. Wang, Y. Wang, and W. Tao. Evaluation of the icp algorithm in 3d point cloud registration. *IEEE Access*, 8:68030–68048, 2020.

[80] Hoon Lim, Jae Youn Choi, Young Sik Kwon, Eui-Jung Jung, and Byung-Ju Yi. SLAM in indoor pipelines with 15mm diameter. In *2008 IEEE*

*International Conference on Robotics and Automation*. IEEE, May 2008. doi: 10.1109/robot.2008.4543826.

[81] Andreu Corominas Murtra and Josep M. Mirats Tur. IMU and cable encoder data fusion for in-pipe mobile robot localization. In *2013 IEEE Conference on Technologies for Practical Robot Applications (TePRA)*. IEEE, April 2013. doi: 10.1109/tepra.2013.6556377.

[82] Hongjun Chen, Haiming Qi, and Xiaohua Zhang. Research of pipeline robot tracing amp; localization technology based on elf-ep communication. In *2008 IEEE International Symposium on Industrial Electronics*, pages 1300–1305, 2008. doi: 10.1109/ISIE.2008.4676936.

[83] J.Bruce Nestleroth and Richard J. Davis. Application of eddy currents induced by permanent magnets for pipeline inspection. *NDT & E International*, 40(1):77–84, 2007. ISSN 0963-8695. doi: https://doi.org/10.1016/j.ndteint.2006.07.002.

[84] You Wu, Elizabeth Mittmann, Crystal Winston, and Kamal Youcef-Toumi. A practical minimalism approach to in-pipe robot localization. In *2019 American Control Conference (ACC)*. IEEE, July 2019. doi: 10.23919/acc.2019.8814648.

[85] Byeolteo Park and Hyun Myung. Resilient underground localization using magnetic field anomalies for drilling environment. *IEEE Transactions on Industrial Electronics*, 65(2):1377–1387, 2018. doi: 10.1109/TIE.2017.2733420.

[86] Peter Hansen, Hatem Alismail, Brett Browning, and Peter Rander. Stereo visual odometry for pipe mapping. In *2011 IEEE/RSJ International Conference on Intelligent Robots and Systems*. IEEE, September 2011. doi: 10.1109/iros.2011.6094911.

[87] *INS-Assisted Monocular Robot Localization*, volume Volume 8: Dynamic Systems and Control, Parts A and B of *ASME International Mechanical Engineering Congress and Exposition*, 11 2010. doi: 10.1115/IMECE2010-39531. URL `https://doi.org/10.1115/IMECE2010-39531`.

[88] Peter Hansen, Hatem Alismail, Peter Rander, and Brett Browning. Monocular visual odometry for robot localization in LNG pipes. In *2011 IEEE*

*International Conference on Robotics and Automation*. IEEE, May 2011. doi: 10.1109/icra.2011.5979681.

[89] Peter Hansen, Hatem Alismail, Peter Rander, and Brett Browning. Pipe mapping with monocular fisheye imagery. In *2013 IEEE/RSJ International Conference on Intelligent Robots and Systems*, pages 5180–5185, 2013. doi: 10.1109/IROS.2013.6697105.

[90] D. Alejo, F. Caballero, and L. Merino. RGBD-based robot localization in sewer networks. In *2017 IEEE/RSJ International Conference on Intelligent Robots and Systems (IROS)*. IEEE, September 2017. doi: 10.1109/iros.2017.8206263.

[91] Peter Hansen, Hatem Alismail, Peter Rander, and Brett Browning. Visual mapping for natural gas pipe inspection. *The International Journal of Robotics Research*, 34 (4-5):532–558, November 2014. doi: 10.1177/0278364914550133.

[92] Ke Ma, Juanjuan Zhu, Tony J. Dodd, Richard Collins, and Sean R. Anderson. Robot mapping and localisation for feature sparse water pipes using voids as landmarks. In *Towards Autonomous Robotic Systems*, pages 161–166. Springer International Publishing, 2015. doi: 10.1007/978-3-319-22416-9_19.

[93] Teresa Seco, Carlos Rizzo, Jesús Espelosín, and José Luis Villarroel. A robot localization system based on rf fadings using particle filters inside pipes. In *2016 International Conference on Autonomous Robot Systems and Competitions (ICARSC)*, pages 28–34, 2016. doi: 10.1109/ICARSC.2016.22.

[94] Rob Worley, Yicheng Yu, and Sean Anderson. Acoustic echo-localization for pipe inspection robots. In *2020 IEEE International Conference on Multisensor Fusion and Integration for Intelligent Systems (MFI)*, pages 160–165, 2020. doi: 10.1109/MFI49285.2020.9235225.

[95] Christine Evers and Patrick A. Naylor. Acoustic slam. *IEEE/ACM Transactions on Audio, Speech, and Language Processing*, 26(9):1484–1498, 2018. doi: 10.1109/TASLP.2018.2828321.

[96] Miranda Kreković, Ivan Dokmanić, and Martin Vetterli. Echoslam: Simultaneous localization and mapping with acoustic echoes. In *2016 IEEE International*

*Conference on Acoustics, Speech and Signal Processing (ICASSP)*, pages 11–15, 2016. doi: 10.1109/ICASSP.2016.7471627.

[97] Usama Saqib and Jesper Rindom Jensen. Sound-based distance estimation for indoor navigation in the presence of ego noise. In *2019 27th European Signal Processing Conference (EUSIPCO)*, pages 1–5, 2019. doi: 10.23919/EUSIPCO.2019.8902694.

[98] Daniele Salvati, Carlo Drioli, and Gian Luca Foresti. Sound source and microphone localization from acoustic impulse responses. *IEEE Signal Processing Letters*, 23 (10):1459–1463, 2016. doi: 10.1109/LSP.2016.2601878.

[99] Evangelos Giannelos, Emmanouil Andrianakis, Konstantinos Skyvalakis, Antonis G. Dimitriou, and Aggelos Bletsas. Robust rfid localization in multipath with phase-based particle filtering and a mobile robot. *IEEE Journal of Radio Frequency Identification*, pages 1–1, 2021. doi: 10.1109/JRFID.2021.3086759.

[100] Emidio DiGiampaolo and Francesco Martinelli. A robotic system for localization of passive uhf-rfid tagged objects on shelves. *IEEE Sensors Journal*, 18(20):8558–8568, 2018. doi: 10.1109/JSEN.2018.2865339.

[101] Zheng Liu, Zhe Fu, Tongyun Li, Ian White, Richard Penty, and Michael Crisp. An isar-sar based localization method using passive uhf rfid system with mobile robotic platform. In *2020 IEEE International Conference on RFID (RFID)*, pages 1–7, 2020. doi: 10.1109/RFID49298.2020.9244907.

[102] Anastasios Tzitzis, Spyros Megalou, Stavroula Siachalou, Tsardoulias G. Emmanouil, Athanasios Kehagias, Traianos V. Yioultsis, and Antonis G. Dimitriou. Localization of rfid tags by a moving robot, via phase unwrapping and non-linear optimization. *IEEE Journal of Radio Frequency Identification*, 3(4):216–226, 2019. doi: 10.1109/JRFID.2019.2936969.

[103] Luca Catarinucci, Salvatore Tedesco, and Luciano Tarricone. Customized ultra high frequency radio frequency identification tags and reader antennas enabling reliable mobile robot navigation. *IEEE Sensors Journal*, 13(2):783–791, 2013. doi: 10.1109/JSEN.2012.2227715.

[104] Fabio Bernardini, Alice Buffi, Daniele Fontanelli, David Macii, Valerio Magnago, Mirko Marracci, Andrea Motroni, Paolo Nepa, and Bernardo Tellini. Robot-based indoor positioning of uhf-rfid tags: The sar method with multiple trajectories. *IEEE Transactions on Instrumentation and Measurement*, 70:1–15, 2021. doi: 10.1109/TIM.2020.3033728.

[105] A. Buffi, P. Nepa, and R. Cioni. Sarfid on drone: Drone-based uhf-rfid tag localization. In *2017 IEEE International Conference on RFID Technology Application (RFID-TA)*, pages 40–44, 2017. doi: 10.1109/RFID-TA.2017.8098872.

[106] S. R. Rusu, M. J. D. Hayes, and J. A. Marshall. Localization in large-scale underground environments with rfid. In *2011 24th Canadian Conference on Electrical and Computer Engineering(CCECE)*, pages 001140–001143, 2011. doi: 10.1109/CCECE.2011.6030640.

[107] C. Li, L. Mo, and D. Zhang. Review on uhf rfid localization methods. *IEEE Journal of Radio Frequency Identification*, 3(4):205–215, 2019. doi: 10.1109/JRFID.2019.2924346.

[108] J. Virtanen, L. Ukkonen, T. Björninen, L. Sydänheimo, and A. Z. Elsherbeni. Temperature sensor tag for passive uhf rfid systems. In *2011 IEEE Sensors Applications Symposium*, pages 312–317, 2011. doi: 10.1109/SAS.2011.5739788.

[109] E. M. Amin, M. S. Bhuiyan, N. C. Karmakar, and B. Winther-Jensen. Development of a low cost printable chipless rfid humidity sensor. *IEEE Sensors Journal*, 14(1): 140–149, 2014. doi: 10.1109/JSEN.2013.2278560.

[110] I. Gammoudi, B. Aissa, M. Nedil, and M. M. Abdallah. Cnt-rfid passive tag antenna for gas sensing in underground mine. In *2015 IEEE International Symposium on Antennas and Propagation USNC/URSI National Radio Science Meeting*, pages 1758–1759, 2015. doi: 10.1109/APS.2015.7305268.

[111] Saber Kazeminasab, Mohsen Aghashahi, Rouxi Wu, and M. Katherine Banks. Localization techniques for in-pipe robots in water distribution systems. In *2020 8th International Conference on Control, Mechatronics and Automation (ICCMA)*, pages 6–11, 2020. doi: 10.1109/ICCMA51325.2020.9301560.

[112] Carlos Rizzo, Vijay Kumar, Francisco Lera, and José Luis Villarroel. Rf odometry for localization in pipes based on periodic signal fadings. In *2014 IEEE/RSJ International Conference on Intelligent Robots and Systems*, pages 4577–4583, 2014. doi: 10.1109/IROS.2014.6943211.

[113] F. Martinelli. A robot localization system combining rssi and phase shift in uhf-rfid signals. *IEEE Transactions on Control Systems Technology*, 23(5):1782–1796, 2015. doi: 10.1109/TCST.2014.2386777.

[114] J. Zhang, Y. Lyu, J. Patton, S. C. G. Periaswamy, and T. Roppel. BFVP: A Probabilistic UHF RFID Tag Localization Algorithm Using Bayesian Filter and a Variable Power RFID Model. *IEEE Transactions on Industrial Electronics*, 65(10): 8250–8259, 2018. doi: 10.1109/TIE.2018.2803720.

[115] Y. Xu, K. Xu, J. Wan, Z. Xiong, and Y. Li. Research on particle filter tracking method based on kalman filter. In *2018 2nd IEEE Advanced Information Management,Communicates,Electronic and Automation Control Conference (IMCEC)*, pages 1564–1568, 2018. doi: 10.1109/IMCEC.2018.8469578.

[116] N. Y. Ko and T. G. Kim. Comparison of kalman filter and particle filter used for localization of an underwater vehicle. In *2012 9th International Conference on Ubiquitous Robots and Ambient Intelligence (URAI)*, pages 350–352, 2012. doi: 10.1109/URAI.2012.6463013.

[117] Christopher K Williams and Carl Edward Rasmussen. *Gaussian processes for machine learning*, volume 2. MIT press Cambridge, MA, 2006.

[118] Andreas Krause, Ajit Singh, and Carlos Guestrin. Near-optimal sensor placements in gaussian processes: Theory, efficient algorithms and empirical studies. *Journal of Machine Learning Research*, 9:235–284, 02 2008. doi: 10.1145/1390681.1390689.

[119] Neil Lawrence. Gaussian process latent variable models for visualisation of high dimensional data. In S. Thrun, L. Saul, and B. Schölkopf, editors, *Advances in Neural Information Processing Systems*, volume 16. MIT Press, 2004.

[120] C. Karen Liu, Aaron Hertzmann, and Zoran Popović. Learning physics-based motion style with nonlinear inverse optimization. *ACM Trans. Graph.*, 24(3):1071–1081, July 2005. ISSN 0730-0301. doi: 10.1145/1073204.1073314.

[121] Andrew Howard, Sajid Siddiqi, and Gaurav S Sukhatme. An experimental study of localization using wireless ethernet. In *Field and Service Robotics*, pages 145–153. Springer, 2003.

[122] Andreas Haeberlen, Eliot Flannery, Andrew Ladd, Algis Rudys, Dan Wallach, and Lydia Kavraki. Practical robust localization over large-scale 802.11 wireless networks. *Proceedings of the Annual International Conference on Mobile Computing and Networking, MOBICOM*, pages 70–84, 01 2004. doi: 10.1145/1023720.1023728.

[123] Julie Letchner, Dieter Fox, and Anthony LaMarca. Large-scale localization from wireless signal strength. In *AAAI*, pages 15–20, 2005.

[124] Karthick Thiyagarajan, Parikshit Acharya, Lasitha Piyathilaka, and Sarath Kodagoda. Numerical modeling of the effects of electrode spacing and multilayered concrete resistivity on the apparent resistivity measured using wenner method. In *2020 15th IEEE Conference on Industrial Electronics and Applications (ICIEA)*, pages 200–206, 2020. doi: 10.1109/ICIEA48937.2020.9248217.

[125] Pradipta Sarkar. Sequential monte carlo methods in practice. *Technometrics*, 45(1): 106, 2003.

[126] Mahesh Vemula, MÓnica F. Bugallo, and Petar M. Djuric. Performance comparison of gaussian-based filters using information measures. *IEEE Signal Processing Letters*, 14(12):1020–1023, 2007. doi: 10.1109/LSP.2007.906214.

[127] Liangqun Li, Zhenglong Yi, and Weixin Xie. Gaussian sum quadrature particle filtering. In *2014 12th International Conference on Signal Processing (ICSP)*, pages 234–238, 2014. doi: 10.1109/ICOSP.2014.7015004.

[128] Jinlong Xian and Yulong Geng. Multi-user detection based on gaussian particle filter in impulsive noise. In *2013 2nd International Symposium on Instrumentation and Measurement, Sensor Network and Automation (IMSNA)*, pages 349–352, 2013. doi: 10.1109/IMSNA.2013.6743287.

[129] Hui-ying Dong, Bin Cao, and Yue-ping Yang. Application of particle filter for target tracking in wireless sensor networks. In *2010 International Conference on Communications and Mobile Computing*, volume 3, pages 504–508, 2010. doi: 10.1109/CMC.2010.228.

[130] Saber Kazeminasab, Mohsen Aghashahi, Rouxi Wu, and M. Katherine Banks. Localization techniques for in-pipe robots in water distribution systems. In *2020 8th International Conference on Control, Mechatronics and Automation (ICCMA)*, pages 6–11, 2020. doi: 10.1109/ICCMA51325.2020.9301560.

[131] Yuanxin Wu, Xiaoping Hu, D. Hu, and Meiping Wu. Comments on "gaussian particle filtering". *IEEE Transactions on Signal Processing*, 53(8):3350–3351, 2005. doi: 10.1109/TSP.2005.851187.

[132] Juan Zhang, Zhigang Liu, and Yuehan Lin. Correlation gaussian particle filter for robust visual tracking. In *2020 Chinese Control And Decision Conference (CCDC)*, pages 4854–4857, 2020. doi: 10.1109/CCDC49329.2020.9163946.

[133] Juho Kokkala and Simo Sarkka. Split-gaussian particle filter. In *2015 23rd European Signal Processing Conference (EUSIPCO)*, pages 484–488, 2015. doi: 10.1109/EUSIPCO.2015.7362430.

[134] Jing Wang, Hong Man, and Yafeng Yin. Multitarget tracking using gaussian process dynamical model particle filter. In *2008 15th IEEE International Conference on Image Processing*, pages 1580–1583, 2008. doi: 10.1109/ICIP.2008.4712071.

[135] Chao Shao. Improving the gaussian sum particle filtering by mmse constraint. In *2008 9th International Conference on Signal Processing*, pages 34–37, 2008. doi: 10.1109/ICOSP.2008.4697062.

[136] Tiancheng Li, Miodrag Bolic, and Petar M. Djuric. Resampling methods for particle filtering: Classification, implementation, and strategies. *IEEE Signal Processing Magazine*, 32(3):70–86, 2015. doi: 10.1109/MSP.2014.2330626.

[137] Carl Edward Rasmussen. *Gaussian Processes in Machine Learning*, pages 63–71. Springer Berlin Heidelberg, Berlin, Heidelberg, 2004.

[138] Mathieu Bouet and Aldri L. dos Santos. Rfid tags: Positioning principles and localization techniques. In *2008 1st IFIP Wireless Days*, pages 1–5, 2008. doi: 10.1109/WD.2008.4812905.

[139] Amal Gunatilake. IEEE ICIEA 2021 Conference - Single Antenna RFID Localization with GP based Particle Filter, 11 2020. URL `https://www.youtube.com/watch?v=iDc8cqeq_RY`.

[140] Jian Zhang, Yibo Lyu, Justin Patton, Senthilkumar C. G. Periaswamy, and Thaddeus Roppel. Bfvp: A probabilistic uhf rfid tag localization algorithm using bayesian filter and a variable power rfid model. *IEEE Transactions on Industrial Electronics*, 65(10):8250–8259, 2018. doi: 10.1109/TIE.2018.2803720.

[141] Bo Tao, Haibing Wu, Zeyu Gong, Zhouping Yin, and Han Ding. An rfid-based mobile robot localization method combining phase difference and readability. *IEEE Transactions on Automation Science and Engineering*, 18(3):1406–1416, 2021. doi: 10.1109/TASE.2020.3006724.

[142] A. Motroni, P. Nepa, P. Tripicchio, and M. Unetti. A multi-antenna sar-based method for uhf rfid tag localization via ugv. In *2018 IEEE International Conference on RFID Technology Application (RFID-TA)*, pages 1–6, 2018. doi: 10.1109/RFID-TA.2018.8552780.

[143] F. Bernardini, A. Motroni, P. Nepa, A. Buffi, P. Tripicchio, and M. Unetti. Particle swarm optimization in multi-antenna sar-based localization for uhf-rfid tags. In *2019 IEEE International Conference on RFID Technology and Applications (RFID-TA)*, pages 291–296, 2019. doi: 10.1109/RFID-TA.2019.8891990.

[144] Shen Leixian, Qingyun Zhang, Jiayi Pang, He Xu, Peng Li, and Donghui Xue. Antspin: Efficient absolute localization method of rfid tags via spinning antenna. *Sensors*, 19:2194, 05 2019. doi: 10.3390/s19092194.

[145] Mariusz Weglarski, Piotr Jankowski-Mihułowicz, Mateusz Chamera, Justyna Dziedzic, and Paweł Kwaśnicki. Designing antennas for rfid sensors in monitoring parameters of photovoltaic panels. *Micromachines*, 11:420, 04 2020. doi: 10.3390/mi11040420.

[146] Piotr Jankowski-Mihułowicz and Mariusz Weglarski. Definition, characteristics and determining parameters of antennas in terms of synthesizing the interrogation zone in rfid systems. In Paulo Cesar Crepaldi and Tales Cleber Pimenta, editors, *Radio Frequency Identification*, chapter 5. IntechOpen, Rijeka, 2017. doi: 10.5772/intechopen.71378.

[147] Jelena Kaitovic, Robert Langwieser, and Markus Rupp. Rfid reader with multi antenna physical layer collision recovery receivers. In *2011 IEEE International Conference on RFID-Technologies and Applications*, pages 286–291, 2011. doi: 10.1109/RFID-TA.2011.6068651.

[148] Sicheng Zou, Michael Crisp, Sithamparanathan Sabesan, Abdullah Kadri, Richard V. Penty, and Ian H. White. An optimization model for antenna selection and deployment in single and multi-cell rfid systems. In *2015 IEEE International Conference on RFID Technology and Applications (RFID-TA)*, pages 87–92, 2015. doi: 10.1109/RFID-TA.2015.7379803.

[149] Gonzalo Crespo, Jorge Teniente, Iñigo Ederra, and Ramon Gonzalo. Experimental study of the antenna influence in rtls based-on rfid. In *2012 6th European Conference on Antennas and Propagation (EUCAP)*, pages 2500–2504, 2012. doi: 10.1109/EuCAP.2012.6206172.

[150] Bo Tao, Haibing Wu, Zeyu Gong, Zhouping Yin, and Han Ding. An RFID-Based Mobile Robot Localization Method Combining Phase Difference and Readability. *IEEE Transactions on Automation Science and Engineering*, pages 1–11, 2020. doi: 10.1109/TASE.2020.3006724.

[151] Po Yang, Wenyan Wu, Mansour Moniri, and Claude C. Chibelushi. Efficient object localization using sparsely distributed passive rfid tags. *IEEE Transactions on Industrial Electronics*, 60(12):5914–5924, 2013. doi: 10.1109/TIE.2012.2230596.

[152] Soonshin Han, HyungSoo Lim, and JangMyung Lee. An efficient localization scheme for a differential-driving mobile robot based on rfid system. *IEEE Transactions on Industrial Electronics*, 54(6):3362–3369, 2007. doi: 10.1109/TIE.2007.906134.

[153] Nabil Belbachir, Nadia Noori, and Benyamin Akdemir. Real-time vehicle localization using on-board visual slam for detection and tracking. In *2019 IEEE/CVF International Conference on Computer Vision Workshop (ICCVW)*, pages 4291–4295, 2019. doi: 10.1109/ICCVW.2019.00528.

[154] Li Yaojun, Pan Quan, Zhao Chunhui, and Yang Feng. Scene matching based ekf-slam visual navigation. In *Proceedings of the 31st Chinese Control Conference*, pages 5094–5099, 2012.

[155] Shao-Hung Chan, Ping-Tsang Wu, and Li-Chen Fu. Robust 2d indoor localization through laser slam and visual slam fusion. In *2018 IEEE International Conference on Systems, Man, and Cybernetics (SMC)*, pages 1263–1268, 2018. doi: 10.1109/SMC.2018.00221.

[156] Zhiqian Cheng and Geng Wang. Real-time rgb-d slam with points and lines. In *2018 2nd IEEE Advanced Information Management,Communicates,Electronic and Automation Control Conference (IMCEC)*, pages 119–122, 2018. doi: 10.1109/IMCEC.2018.8469424.

[157] Yubao Liu and Jun Miura. Rds-slam: Real-time dynamic slam using semantic segmentation methods. *IEEE Access*, 9:23772–23785, 2021. doi: 10.1109/ACCESS.2021.3050617.

[158] Hailan Kuang, Xiaodan Wang, Xinhua Liu, Xiaolin Ma, and Ruifang Li. An improved robot's localization and mapping method based on orb-slam. In *2017 10th International Symposium on Computational Intelligence and Design (ISCID)*, volume 2, pages 400–403, 2017. doi: 10.1109/ISCID.2017.179.

[159] *INS-Assisted Monocular Robot Localization*, volume Volume 8: Dynamic Systems and Control, Parts A and B of *ASME International Mechanical Engineering Congress and Exposition*, 11 2010. doi: 10.1115/IMECE2010-39531. URL `https://doi.org/10.1115/IMECE2010-39531`.

[160] Peter Hansen, Hatem Alismail, Peter Rander, and Brett Browning. Visual mapping for natural gas pipe inspection. *The International Journal of Robotics Research*, 34 (4-5):532–558, 2015. doi: 10.1177/0278364914550133.

[161] Wen Zhao, Mitsuhiro Kamezaki, Kento Yoshida, Minoru Konno, Akihiko Onuki, and Shigeki Sugano. Modeling and simulation of flc-based navigation algorithm for small gas pipeline inspection robot. In *2018 IEEE/ASME International Conference on Advanced Intelligent Mechatronics (AIM)*, pages 912–917, 2018. doi: 10.1109/AIM.2018.8452416.

[162] Rahul Summan, William Jackson, Gordon Dobie, Charles MacLeod, Carmelo Mineo, Graeme West, Douglas Offin, Gary Bolton, Stephen Marshall, and Alexandre Lille. A novel visual pipework inspection system. *AIP Conference Proceedings*, 1949(1): 220001, 2018. doi: 10.1063/1.5031647.

[163] Atsushi Kakogawa, Yuki Komurasaki, and Shugen Ma. Anisotropic shadow-based operation assistant for a pipeline-inspection robot using a single illuminator and camera. In *2017 IEEE/RSJ International Conference on Intelligent Robots and Systems (IROS)*, pages 1305–1310, 2017. doi: 10.1109/IROS.2017.8202306.

[164] Atsushi Kakogawa, Taiju Yamagami, Yang Tian, and Shugen Ma. Recognition of pathway directions based on nonlinear least squares method. In *2015 IEEE International Conference on Robotics and Biomimetics (ROBIO)*, pages 1596–1601, 2015. doi: 10.1109/ROBIO.2015.7418999.

[165] Dong-Hyuk Lee, Hyungpil Moon, Ja Koo, and Hyouk Choi. Map building method for urban gas pipelines based on landmark detection. *International Journal of Control, Automation and Systems*, 11, 02 2013. doi: 10.1007/s12555-012-0049-6.

[166] Jens T. Thielemann, Goril M. Breivik, and Asbjorn Berge. Pipeline landmark detection for autonomous robot navigation using time-of-flight imagery. In *2008 IEEE Computer Society Conference on Computer Vision and Pattern Recognition Workshops*, pages 1–7, 2008. doi: 10.1109/CVPRW.2008.4563167.

[167] Ke Ma, Michele Schirru, Ali Hassan Zahraee, Rob Dwyer-Joyce, Joby Boxall, Tony J. Dodd, Richard Collins, and Sean R. Anderson. Pipeslam: Simultaneous localisation and mapping in feature sparse water pipes using the rao-blackwellised particle filter. In *2017 IEEE International Conference on Advanced Intelligent Mechatronics (AIM)*, pages 1459–1464, 2017. doi: 10.1109/AIM.2017.8014224.

[168] Yoshiaki Bando, Hiroki Suhara, Motoyasu Tanaka, Tetsushi Kamegawa, Katsutoshi Itoyama, Kazuyoshi Yoshii, Fumitoshi Matsuno, and Hiroshi G. Okuno. Sound-based online localization for an in-pipe snake robot. In *2016 IEEE International Symposium on Safety, Security, and Rescue Robotics (SSRR)*, pages 207–213, 2016. doi: 10.1109/SSRR.2016.7784300.

[169] Douglas Daniel Sampaio Santana, Newton Maruyama, and Celso Massatoshi Furukawa. Estimation of trajectories of pipeline pigs using inertial measurements and non linear sensor fusion. In *2010 9th IEEE/IAS International Conference on Industry Applications - INDUSCON 2010*, pages 1–6, 2010. doi: 10.1109/INDUSCON.2010.5739911.

[170] Md Sheruzzaman Chowdhury and Mamoun F. Abdel-Hafez. Pipeline Inspection Gauge Position Estimation Using Inertial Measurement Unit, Odometer, and a Set of Reference Stations. *ASCE-ASME J Risk and Uncert in Engrg Sys Part B Mech Engrg*, 2(2), 01 2016. ISSN 2332-9017. doi: 10.1115/1.4030945. 021001.

[171] Wasim M. F. Al-Masri, Mamoun F. Abdel-Hafez, and Mohammad A. Jaradat. Inertial navigation system of pipeline inspection gauge. *IEEE Transactions on Control Systems Technology*, 28(2):609–616, 2020. doi: 10.1109/TCST.2018.2879628.

[172] Andreu Corominas Murtra and Josep M. Mirats Tur. Imu and cable encoder data fusion for in-pipe mobile robot localization. In *2013 IEEE Conference on Technologies for Practical Robot Applications (TePRA)*, pages 1–6, 2013. doi: 10.1109/TePRA.2013.6556377.

[173] Lianwu Guan, Xiaodan Cong, Yunlong Sun, Yanbin Gao, Umar Iqbal, and Aboelmagd Noureldin. Enhanced mems sins aided pipeline surveying system by pipeline junction detection in small diameter pipeline. *IFAC-PapersOnLine*, 50(1): 3560–3565, 2017. ISSN 2405-8963. doi: https://doi.org/10.1016/j.ifacol.2017.08.962. 20th IFAC World Congress.

[174] Hussein Sahli and Naser El-Sheimy. A novel method to enhance pipeline trajectory determination using pipeline junctions. *Sensors*, 16(4), 2016. ISSN 1424-8220. doi: 10.3390/s16040567.

[175] Lianwu Guan, Xu Xu, Yanbin Gao, Fanming Liu, Hanxiao Rong, Meng Wang, and Aboelmagd Noureldin. *Micro-Inertial-Aided High-Precision Positioning Method for Small-Diameter PIG Navigation*. IntechOpen, 11 2018. ISBN 978-1-83880-564-7. doi: 10.5772/intechopen.80343.

[176] You Wu, Elizabeth Mittmann, Crystal Winston, and Kamal Youcef-Toumi. A practical minimalism approach to in-pipe robot localization. In *2019 American Control Conference (ACC)*, pages 3180–3187, 2019. doi: 10.23919/ACC.2019.8814648.

[177] Hoon Lim, Jae Youn Choi, Young Sik Kwon, Eui-Jung Jung, and Byung-Ju Yi. Slam in indoor pipelines with 15mm diameter. In *2008 IEEE International Conference on Robotics and Automation*, pages 4005–4011, 2008. doi: 10.1109/ROBOT.2008.4543826.

[178] Byeolteo Park and Hyun Myung. Resilient underground localization using magnetic field anomalies for drilling environment. *IEEE Transactions on Industrial Electronics*, 65(2):1377–1387, 2018. doi: 10.1109/TIE.2017.2733420.

[179] Feng Lu and Evangelos E. Milios. Globally consistent range scan alignment for environment mapping. *Autonomous Robots*, 4:333–349, 1997.

[180] Sebastian Thrun and Michael Montemerlo. The graph slam algorithm with applications to large-scale mapping of urban structures. *The International Journal of Robotics Research*, 25(5-6):403–429, 2006. doi: 10.1177/0278364906065387.

[181] Frank Dellaert and Michael Kaess. Square root sam: Simultaneous localization and mapping via square root information smoothing. *I. J. Robotic Res.*, 25:1181–1203, 12 2006. doi: 10.1177/0278364906072768.

[182] Fang Bai, Teresa Vidal-Calleja, and Giorgio Grisetti. Sparse pose graph optimization in cycle space. *IEEE Transactions on Robotics*, pages 1–20, 2021. doi: 10.1109/TRO.2021.3050328.

[183] Giorgio Grisetti, Rainer Kümmerle, Cyrill Stachniss, and Wolfram Burgard. A tutorial on graph-based slam. *IEEE Transactions on Intelligent Transportation Systems Magazine*, 2:31–43, 12 2010. doi: 10.1109/MITS.2010.939925.

[184] Rana Azzam, Felix H. Kong, Tarek Taha, and Yahya Zweiri. Pose-graph neural network classifier for global optimality prediction in 2d slam. *IEEE Access*, 9:80466–80477, 2021. doi: 10.1109/ACCESS.2021.3084599.

[185] Edwin Olson, John Leonard, and Seth Teller. Fast iterative alignment of pose graphs with poor initial estimates. In *Proceedings 2006 IEEE International Conference on Robotics and Automation, 2006. ICRA 2006.*, pages 2262 – 2269. IEEE, 06 2006. doi: 10.1109/ROBOT.2006.1642040.

[186] Tae-jae Lee, Byung-moon Jang, and Dong-il Dan Cho. A non-iterative pose-graph optimization algorithm for fast 2d slam. In *2014 IEEE International Conference on Robotics and Biomimetics (ROBIO 2014)*, pages 1596–1601, 2014. doi: 10.1109/ROBIO.2014.7090562.

[187] Talha Takleh Omar Takleh, Nordin abu bakar, Shuzlina Rahman, Raseeda Hamzah, and Zalilah Abd Aziz. A brief survey on slam methods in autonomous vehicle. *International Journal of Engineering and Technology(UAE)*, 7:38–43, 11 2018. doi: 10.14419/ijet.v7i4.27.22477.

[188] S. Thrun, W. Burgard, D. Fox, and R.C. Arkin. *Probabilistic Robotics*. Intelligent Robotics and Autonomous Agents series. MIT Press, 2005. ISBN 9780262201629. URL `https://books.google.com.au/books?id=2Zn6AQAAQBAJ`.

[189] Weiyang Lin, Jianjun Hu, Hong Xu, Chao Ye, Xiao Ye, and Zhan Li. Graph-based slam in indoor environment using corner feature from laser sensor. In *2017 32nd Youth Academic Annual Conference of Chinese Association of Automation (YAC)*, pages 1211–1216, 2017. doi: 10.1109/YAC.2017.7967597.

[190] H. Durrant-Whyte and T. Bailey. Simultaneous localization and mapping: part i. *IEEE Robotics Automation Magazine*, 13(2):99–110, 2006. doi: 10.1109/MRA.2006.1638022.